

Multiphysical Characterization of Medium-Frequency Power Electronic Transformers

THÈSE N° 4622 (2010)

PRÉSENTÉE LE 9 AVRIL 2010

À LA FACULTÉ SCIENCES ET TECHNIQUES DE L'INGÉNIEUR
LABORATOIRE D'ÉLECTRONIQUE INDUSTRIELLE
PROGRAMME DOCTORAL EN ENERGIE

ÉCOLE POLYTECHNIQUE FÉDÉRALE DE LAUSANNE

POUR L'OBTENTION DU GRADE DE DOCTEUR ÈS SCIENCES

PAR

Irma VILLAR

acceptée sur proposition du jury:

Prof. F. Rachidi-Haeri, président du jury
Prof. A. Rufer, directeur de thèse
Prof. R. W. De Doncker, rapporteur
Dr I. Etxeberria-Otadui, rapporteur
Prof. J.-J. Simond, rapporteur



ÉCOLE POLYTECHNIQUE
FÉDÉRALE DE LAUSANNE

Suisse
2010

Preface

Six years ago, I started my master thesis project at Ikerlan-IK4 in the Power Electronics Area, where Marcelino Caballero, the head of the area at the time, and Unai Viscarret, my supervisor convince me to begin this long journey. Five years ago, expecting to become a PhD student at the EPFL, I visited the Industrial Electronics Laboratory directed by Prof. Alfred Rufer. From then on I have been an external, but mostly internal, PhD student.

First of all, special thanks to Prof. Alfred Rufer for accepting me as a PhD student at the Industrial Electronics Laboratory and for the confidence he placed in me throughout this project.

I would like to thanks the president of the jury Prof. Farhad Rachidi-Haeri, and its members Prof. Alfred Rufer, Prof. Jean-Jacques Simond, Prof. Rik W. de Doncker and Dr. Ion Etxeberria-Otadui for their valuable participation in the exam.

From the Industrial Electronics Laboratory I would like to thanks all the administrative and technical staff, particularly Fabienne Vionnet for her kindness. I also wish to thanks my colleagues and occasional visitors at the Laboratory for their support and for the god atmosphere they created in the lab. Especially I want to thanks those who have suffer from my presence like Frédéric, Antoine, Stephan and Yannick.

From the Power Electronics Area at Ikerlan-IK4 I would also like to thanks all my past and present colleagues for the excellent atmosphere they created in my short stays at the area. I sincerely want to thanks Unai Viscarret for always being just there, and Ion Etxeberria-Otadui, the current head of the area, for being the light of my bright present.

I would also like to thank all my *basque* friends in Lausanne, who in many different ways have shared with me four excellent years of my life.

Special thanks to my girls, Olatz and Maialen, and my very best friends Marije, Mairu, Naiara, Deiane, Miren and Vanessa (from wherever you are watching us). A huge thanks to my whole family, for following and supporting me throughout this fulfilling experience, specially to my brother Gorka and to Nerea, and to my joyful niece Ilargi. And last but not least, a hearty thanks to my parents, *aitta ta ama*, who gave me the strength to be right here.

*Guztioi, eta batez ere zuei,
bihotzez eskerrak.*

Irma

Summary

Europe is currently making a great effort in order to improve the sustainability and reduce the environmental impact of its energy and transportation systems. A key role on these initiatives is played by efficient generation systems, like cogeneration, and clean or renewable energies, like wind or solar energy, as well as, by efficient and improved transportation technologies.

In the evolution of these energy and transport systems, the development of Power Electronic Converters with greater functionality, higher reliability, higher efficiency, lower cost, and more sophisticated control will be essential. The main goal of future Power Electronic Converters will be to increase power density, reduce cost and improve reliability. This way, volume, weight and material reduction as well as reliability will gain the future market. A great contribution of these goals will be made by new high-power semiconductor devices, which permit the extension of the frequency range of power converters, and consequently the reduction of magnetic components. A good example of one of these systems are medium-frequency power conversion systems, also known as Power Electronic Transformers, which are able to convert electric power as convectional transformers but with increased features: volume and weight reduction, power transfer and quality control etc.

The present work introduces a complete characterization of a medium-frequency power transformer, suitable for efficient Power Electronic conversion systems. The motivation of the present work stems out from the need to evaluate the constraints of conventional transformer characterization and design methodologies. The proposed expressions are able to successfully address the problematic related to non-sinusoidal waveforms, typical of medium-frequency power transformers. Moreover, a design methodology for the optimal design of medium-frequency power trans-

SUMMARY

formers is introduced. The characterization, as well as the design methodology, are verified by means of finite element simulations and measurement results.

Key Words: Power Electronic Transformer, Medium-Frequency Transformer, Non-Sinusoidal Transformer Characterization, Transformer Design Methodology.

Résumé

L'Europe fait actuellement un grand effort afin d'améliorer la durabilité et réduire les incidences sur l'environnement des systèmes d'énergie et de transport. Un rôle principal sur ces initiatives est joué par les systèmes d'haute rendement, comme la cogénération, et les énergies propres ou renouvelables, comme les éoliens ou l'énergie solaire, comme, par des technologies d'haute rendement de transport.

Dans l'évolution de l'énergie et les systèmes de transport, le développement des convertisseurs d'électronique de puissance plus fonctionnelle, avec une fiabilité plus élevée, aussi bien qu'un rendement élevée, moins coûteux, et une commande plus sophistiquée seront essentiels.

Les défis principaux des futurs convertisseurs d'électronique de puissance seront d'augmenter la densité de puissance, réduire le coût et améliorer la fiabilité. De cette manière la réduction du volume, du poids et du matériel aussi bien que la fiabilité gagneront le futur marché. Une grande contribution à ces buts sera apportée par les nouveaux semiconducteurs de puissance, qui permettent l'extension de la gamme de fréquence des convertisseurs de puissance, et par conséquent la réduction de la taille et volume des composants magnétiques. Un bon exemple d'un de ces systèmes sont les systèmes de conversion à moyenne fréquence, également connus sous le nom de Transformateurs d'Électronique de Puissance, qui peuvent convertir les niveaux de tension, comme les transformateurs conventionnels mais avec des caractéristiques ajoutées: réduction du volume et du poids, contrôle du transfert de puissance et de la qualité etc.

Le travail actuel présente une caractérisation complète d'un transformateur de moyenne fréquence, appropriée pour des systèmes de conversion d'électronique de puissance d'haute rendement. La motivation du travail réside dans la né-

cessité d'évaluer les contraintes de la caractérisation des transformateurs et des méthodologies de conception conventionnelles. Les expressions proposées peuvent adresser avec succès la problématique complexe liée aux formes d'onde non-sinusoidales, typiques des transformateurs de moyenne fréquence. D'ailleurs, une méthodologie de conception pour la conception optimale des transformateurs de moyenne fréquence est présentée. La caractérisation, aussi bien que la méthodologie de conception, sont vérifiées au moyen de simulations d'élément finis et résultats expérimentaux.

Mots Clés: Transformateur d'Électronique de Puissance, Transformateur de Moyenne Fréquence, Caractérisation Non-Sinusoidal, Méthode de Conception des Transformateurs

Contents

Preface	i
Summary	iii
Résumé	v
Contents	x
Notations	xi
1. The Power Electronic Transformer: From Low to Medium-Frequency Conversion	1
1.1. The Global Picture	2
1.2. Power Electronic Transformers	4
1.2.1. Traction Transformers	8
1.2.2. Offshore Wind Farm Transformers	9
1.2.3. Future Flexible Distribution Transformers	10
1.3. Medium-Frequency Power Transformers	12
1.4. Motivation of the Present Work	17
1.5. Structure of this Document	18
2. Multiphysical Characterization of Medium-Frequency Power Transformers	19
2.1. Introduction	20

vii

2.2. Windings and Parasitics	22
2.2.1. Frequency Effects	22
2.2.2. Winding Losses	23
2.2.3. Leakage Inductance	48
2.3. Magnetic Core, Magnetic Losses	55
2.3.1. Magnetic Hysteresis	56
2.3.2. Hysteresis Models	57
2.3.3. Loss Separation Approach	63
2.3.4. Empirical Methods, Steinmetz Equation	67
2.3.5. Methodology Comparison	73
2.4. Thermal Behavior and Temperature Rise	74
2.4.1. Simplified Thermal Model: Equivalent Nodal Network	75
2.4.2. Heat Transfer Coefficients	78
2.4.3. Basic Static Network	82
2.5. Conclusions	87
3. Medium-Frequency Transformer Design Methodology	89
3.1. Design Flow Chart	90
3.2. Data: Transformer Characteristics and Constraints	93
3.2.1. High-Power Medium-Frequency Magnetic Cores	93
3.2.2. The Amorphous Magnetic Core	95
3.2.3. Heat Dissipation Capacity	96
3.2.4. Loss Distribution for Maximum Efficiency	97
3.2.5. Maximum Power Level	98
3.2.6. Maximum Current Density	102
3.2.7. Operating Frequency Range	104
3.2.8. Optimal Conductor Thickness	105
3.3. Process: Parameterized Equations	111
3.3.1. Number of turns	112
3.3.2. Winding Dimensions	113
3.3.3. Core Dimensions	115
3.3.4. Core Losses	117
3.3.5. Winding Losses	121

3.3.6. Leakage Inductance	123
3.4. Optimization: Minimization Functions	125
3.4.1. The Problem	125
3.4.2. Objective or Cost Function	126
3.5. Conclusions	128
4. Design and Experimental Verification of a Dedicated Medium-Frequency Power Transformer	131
4.1. Context	132
4.2. Operation Principle of the Dual Active Bridge (DAB)	136
4.3. Application Characteristics and Transformer Constraints	138
4.4. Medium-Power Amorphous Cores	140
4.5. Conductor Selection	141
4.6. Winding Losses for the DAB	145
4.7. Optimization Characteristics	147
4.8. MF Power Transformer Prototype	148
4.9. Experimental Results	152
4.9.1. Experimental Set-up	152
4.9.2. Winding Parasitics Measurements	152
4.9.3. Core Loss Measurements	154
4.9.4. Thermal Response	161
4.10. Conclusions	172
5. Conclusions and Future Work	173
5.1. Summary	174
5.2. Contributions	175
5.3. Future work	176
A. Mathematical Developments	179
A.1. Time Harmonic Diffusion Equation	180
A.1.1. Diffusion Equation in Cartesian Coordinates	180
A.1.2. Diffusion Equation in Cylindrical Coordinates	181
A.2. Conduction Loss Expression	182

CONTENTS

A.2.1. Conduction Loss Expression in Cartesian Coordinates	182
A.3. Bessel Functions	183
A.4. Approximations for Modified Bessel Functions	183
B. Physical Properties	187
B.1. Thermal Properties of Various Fluids	188
B.2. Operating Limits for Oil Cooling	188
C. Optimal Conductor Thickness Estimation Error	191
C.1. Optimal Conductor Thickness	192
List of Figures	203
List of Tables	205
Bibliography	216
Curriculum Vitae	217

Notations

Abbreviations

PE	Power Electronics
PET	Power Electronic Transformer
DEPT	Distribution Power Electronic Transformer
TT	Traction Transformer
SST	Solid-State Transformer
MFT	Medium-Frequency Topology or Transformer
IGBT	Insulated Gate Bipolar Transistor
IGCT	Integrated Gate Commutated Thyristors
SiC	Silicon Carbide
FC	Flying Capacitor
NPC	Neutral Point Clamped
CHB	Cascaded H-Bridge
LV	Low Voltage
MV	Medium Voltage
HV	High Voltage
MF	Medium Frequency
MSE	Modified Steinmetz Equation
GSE	Generalized Steinmetz Equation
IGSE	Improved Generalized Steinmetz Equation
NSE	Natural Steinmetz Extension
EEL	Equivalent Elliptical Loop
WcSE	Waveform coefficient Steinmetz Equation

FWC	Flux Waveform Coefficient
DAB	Dual Active Bridge
PWL	Piecewise Linear

Roman Symbols

K	Steinmetz equation constant	
a	Steinmetz equation's frequency parameter	
b	Steinmetz equation's magnetic induction parameter	
k_h	Hysteresis loss constant	
k_e	Eddy current loss constant	
k_a	Anomalous or excess loss constant	
k_1	Generalized Steinmetz Equation constant	
k_i	Improved Generalized Steinmetz Equation constant	
P_v	Volumetric power loss	[W/m ³]
P_s	Specific power loss	[W/kg]
P_h	Static hysteresis loss	[W/kg]
P_e	Classical eddy current loss	[W/kg]
P_a	Excess or anomalous eddy current loss	[W/kg]
P_w	Winding total loss	[W]
P_σ	Foil layer loss	[W]
B	Magnetic induction	[T]
B_m	Maximum magnetic induction	[T]
B_s	Saturation magnetic induction	[T]
B_r	Remanent magnetic induction	[T]
H	Magnetic field	[A/m]
H_s	Saturation magnetic field	[A/m]
H_c	Coercive magnetic field	[A/m]
H_{irr}	Irreversible magnetic field	[A/m]
H_{int}	Internal magnetic field	[A/m]
H_{ext}	External magnetic field	[A/m]
J	Current density	[A/m ²]

f	Frequency	[1/s]
f_{eq}	Equivalent frequency	[1/s]
T	Period	[s]
T	Temperature	[K]
d_g	Interwinding gap thickness	[m]
d_i	Interlayer gap thickness	[m]
d	Round conductor diameter	[m]
d_w	Conductor or layer thickness	[m]
h_w	Conductor or layer height	[m]
l_w	Conductor or layer length	[m]
h_c	Winding window height	[m]
N	Number of conductors in a winding	
l_s	Litz strand length	[m]
r_s	Litz strand radius	[m]
d_s	Litz strand diameter	[m]
n_s	Number of strands in a Litz bundle	
r_b	Litz bundle radius	[m]
d_b	Litz bundle diameter	[m]
p_f	Packing or filling factor	[m]
t_b	Distance between the centers of two adjacent Litz bundles	[m]
t_s	Distance between the centers of two adjacent Litz strands	[m]
I	Peak current	[A]
I_n	Root mean square current	[A]
I_s	Strand peak current	[A]
m	Consecutive number of layers	
p	Consecutively located layer number	
F_r	Resistance factor	
F_L	Inductance factor	
R_{ac}	Ac resistance of a conductor	[Ω]
R_{dc}	Dc resistance of a conductor	[Ω]
$R_{s_{dc}}$	Dc resistance of a single strand	[Ω]
L_σ	Leakage inductance	[H]
L_w	Winding leakage inductance	[H]

L_g	Interwinding leakage inductance	[H]
L_i	Interlayer leakage inductance	[H]
W_m	Magnetic energy	[J]

Greek Symbols

α	Propagation constant	
β	Coefficient of thermal expansion	[1/K]
λ	Thermal conductivity	[W/m K]
δ	Skin depth	[m]
ω	Pulsation frequency	[rad/s]
μ	Permeability	[H/m]
μ_0	Permeability of free space	[H/m]
μ_r	Relative permeability	
σ	Electrical conductivity	[S/m]
ρ	Electrical resistivity	[Ω m]
Δ	Penetration ratio	
γ	Round conductor penetration ratio	
η_w	Porosity factor	
η_1	External porosity factor	
η_2	Internal porosity factor	
ς_1	Skin effect factor for foil windings	
ς_2	Proximity effect factor for foil windings	
τ_1	Resistive skin effect factor in round conductors	
τ_2	Resistive proximity effect factor in round conductors	
φ_1	Inductive skin effect factor in round conductors	
φ_2	Inductive proximity effect factor in round conductors	
ϕ	Magnetic flux	[Wb]
ν	Harmonic number	

1

The Power Electronic Transformer: From Low to Medium-Frequency Conversion

Summary

With the advent of new high-power semiconductor devices, new power conversion structures are conceived to meet the needs of future medium-voltage conversion systems. Though, competitive conversion systems will be characterized by high efficiency, small volume, low weight, and cost effective requirements. In this chapter a state of the art of Power Electronic Transformers is carried out, from application areas to medium-frequency power transformer characteristics.

1.1. The Global Picture

It is a well known fact that increasing operation frequency reduces magnetic device volume, something already put into practice in low-power applications due to the availability of fast and efficient semiconductor devices. Nowadays, in high-power applications this fact is becoming a reality, on the one hand, due to the development of new magnetic materials with higher saturation inductions and lower loss densities, and on the other hand, due the availability of more efficient devices with faster switching possibilities, higher blocking capabilities and higher power densities. These new combined conversion elements with reduced weight and volume can be integrated in ac/dc/ac structures replacing current bulky low-frequency transformers. In medium-voltage applications these new combined conversion structures are expected to become a major technology, where practical voltage levels can fully utilize the existing semiconductor devices and magnetic materials within recent multilevel converters.

Apart from the basic functionalities provided by conventional low-frequency transformers, like voltage adaptation and isolation, the conversion with Power Electronics (PE) structures adds additional features to transformation systems, like power flow regulation and power quality improvement. Thus, depending on their application and features, they are known as Solid-State Transformers (SST) [Lai et al., 2005; Oates and Bassett, 2006], Power Electronic Transformers (PET) [Iman-Eini et al., 2008], Distribution Electronic Power Transformers (DEPT) [Wang et al., 2007], e-Transformers [Taufiq, 2007], dc-dc Electronic Transformers [Filchev et al., 2004], Power Electronic Traction Transformers (TT) [Hugo et al., 2007] or simply Medium-Frequency Topologies [Steiner and Reinold, 2007] or Medium-Frequency

Transformers (MFT). Throughout this work the term Power Electronic Transformer (PET) will be used. Although these new PETs offer interesting advantages over conventional solutions, currently their high-power application faces three main challenges [Blaabjerg et al., 2006; Oates and Bassett, 2006; Strbac et al., 2006; Taufiq, 2007]: 1) higher efficiency requirements, 2) a wider technical and commercial deployment of key components and 3) higher reliability levels.

On the one hand, regarding efficiency, research is focused on two main aspects: converter and transformer optimization. The conversion throughout various silicon stages makes efficiency requirements unattainable compared to conventional low-frequency transformers. Therefore, new conversion topologies [Filchev et al., 2004] and switching techniques (mostly resonant [Steiner and Reinold, 2007] or soft-switching [Schibli, 2000]) are under study. Concerning transformers, their optimization is gathering more attention lately [Aggeler et al., 2008; Heinemann, 2002; Pavlovsky et al., 2005; Steiner and Reinold, 2007]. The core element of these new PE conversion systems will be the medium-frequency power transformer, and its efficiency will depend on the optimized design of the transformer core and winding that will match each of the applications. Contrary to the use of standard commercially available semiconductor devices for optimized conversion topologies, medium-frequency transformer selection will depend on dedicated optimized designs with particular material and building arrangements [Heinemann, 2002].

Concerning the development of key components, besides the medium-frequency transformer, the power electronic converter is also a key element. As a matter of fact, the field of power semiconductors has experienced a considerable advance in the last decades with the increasing power rating of insulated gate bipolar transistors (IGBTs), currently 6.5 kV-750 A and 10 kV devices under test, and high-power, 6.5 kV-4 kA, integrated gate-commutated thyristors (IGCTs) [Bose, 2009]. With the advent of these powerful devices, medium-voltage applications have improved their efficiency, with reduced loss densities in higher operating frequencies and in conduction states. In spite of these advances, new semiconductor devices, like the 10 kV IGCTs, or large band-gap materials, like Silicon Carbide (SiC) or Diamond with higher breakdown electric field, and higher electrical and thermal conductivities, are expected to build high-power density converters in medium-voltage applications. Although, actually, with their difficult and challenging processing

[Bose, 2009], their application is expected in a longer term scenario.

Finally, the questionable reliability of complex multilevel configurations and topologies that are necessary to reach high-power levels [Hiller et al., 2008] with current semiconductor ratings, reduce the reliability of the final system comparing to the well known traditional low-frequency technology, even if some researchers state that reliability levels are very similar for both technologies [Marchesoni et al., 2002].

Despite the advantages and additional functionalities introduced by these new conversion systems, the main motivation that will actually justify their short term application lies in volume, material and weight reduction in highly restricted applications, such as ships [Chabert and Rufer, 2001], traction [Heinemann, 2002] and wind power [Prasai et al., 2008]. As a matter of fact, there is an obvious interest in developing this type of systems, clearly shown by the effort made by several industrial companies, mainly related to traction applications [Engel et al., 2003; Heinemann, 2002; Hugo et al., 2007; Steiner and Reinold, 2007; Taufiq, 2007]. These works prove the technical feasibility of medium-frequency conversion systems, showing their advantages over conventional systems. There are also similar initiatives in the wind power field, related to offshore applications where spatial and weight restrictions are very significant [Prasai et al., 2008]. In contrast, their application in electricity distribution networks seems more difficult in a short term scenario, although there could be some specific exceptions like urban facility upgrading with high-space restrictions [Strbac et al., 2006]. In a longer term scenario, and with the expected evolution of semiconductor devices, Power Electronic Transformers could revolutionize transmission and distribution networks [Oates and Bassett, 2006], offering efficient connections for distributed sources and optimizing power flow in future highly dispersed and interconnected network [Rufer, 2007a].

1.2. Power Electronic Transformers

A Power Electronic Transformer consists, essentially, of two elements a) the medium-frequency transformer (or ac-link), which is an especially designed electromagnetic component and b) two conversion stages (power electronic converters),

one at each side of the transformer, which are used to adapt grid frequency (low) to a medium frequency required for the conversion (see Fig. 1.1).

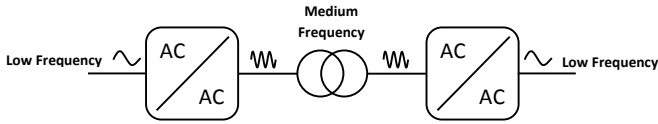


Figure 1.1: Operation principle of Power Electronic Transformers.

This frequency transformation in the conversion stages can be implemented with two different conversion structures:

- Direct conversion (ac/ac).
- Indirect conversion, with a dc-link (ac/dc/ac).

In the former, the conversion from low frequency to medium frequency is made directly (see Fig. 1.2), usually with a cycloconverter [Wu et al., 2008] or a matrix converter [Oates and Bassett, 2006]. In the latter, the conversion is made with an intermediary dc-link (see Fig. 1.2).

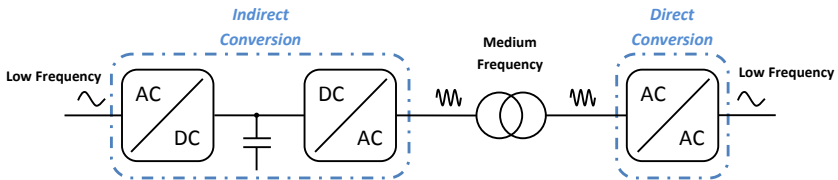


Figure 1.2: Possible Power Electronic Transformer structure.

Within the indirect-conversion family, three multilevel voltage-source inverter topologies are mainly used to handle medium-voltage levels (see Fig. 1.3): 1) the neutral-point clamped (NPC) [Lai et al., 2005], 2) the flying capacitor (FC), and 3) the cascaded H-bridge (CHB). Among them the most common one for medium-voltage transformer applications is the CHB converter, where, with the modular approach, different voltage levels can be reached and redundancy for higher availability can be applied [Steiner and Reinold, 2007]. Other innovative

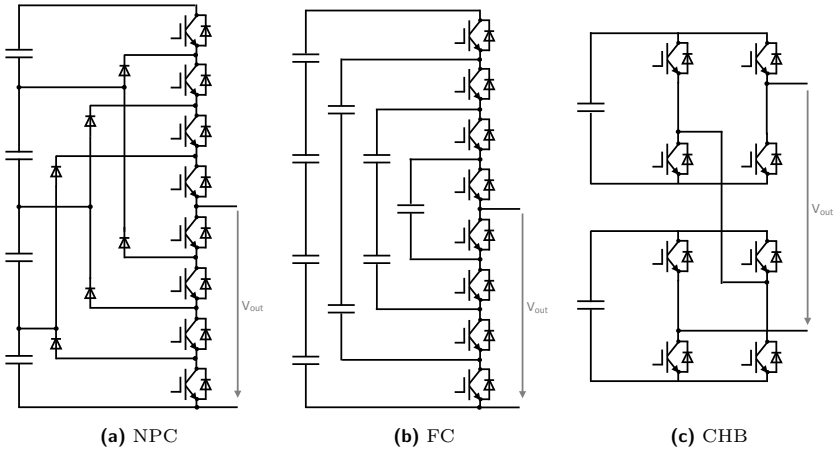


Figure 1.3: 5L inverters.

topologies based on cascaded H-bridge converters have been introduced lately, like in [Mariethoz and Rufer, 2006].

The core element of every indirect-conversion structure is the isolated dc-dc converter (see Fig. 1.4), which stands out as one of the most promising components of future drives [Inoue and Akagi, 2007], electricity networks [Bifaretti et al., 2008], dc grids [Konishi et al., 2005], micro-grids [Biczal, 2007], and wind farms [Meyer et al., 2007], within its single-phase or its three-phase topology.

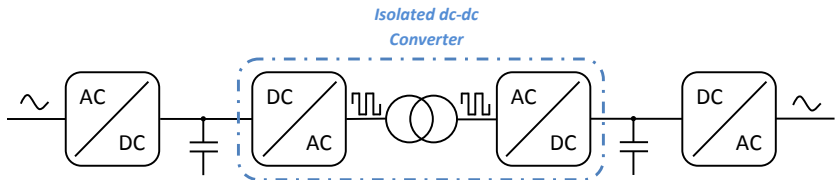


Figure 1.4: Isolated dc-dc converter within a PET with indirect-conversion topology.

In the case of the multilevel cascaded H-bridge structure, the dc-dc converter with its medium-frequency transformer for galvanic isolation usually consists of

an H-bridge inverter at the input side, which transforms dc voltage into an ac signal of a certain frequency. The transformer is excited with a rectangular voltage waveform of medium frequency which makes volume and weight reduction possible. The output of the dc-dc converter rectifies the medium-frequency waveform into, once more, dc voltage. Depending on the application, this second rectifier can be a passive one, with only diodes for a unidirectional power flow, or an active one for a bidirectional power flow.

Two main topologies can be found in the literature for the ac-link of isolated dc-dc converters (see Fig. 1.5), both in single-phase and three-phase topologies: resonant converters (soft-switching converters) and non-resonant ones (hard/soft-switching converters depending on control strategy) [Aggeler et al., 2008; Akagi and Inoue, 2006; Schibli, 2000]. In both converters the ac-link is usually built with the leakage inductance of the transformer. The most common topology for resonant converters is the series-resonant topology [Heinemann, 2002; Konishi et al., 2005; Meyer et al., 2007; Reinold and Steiner, 1999], although new ones like the LCL resonant topology have been introduced lately [Filchev et al., 2004].

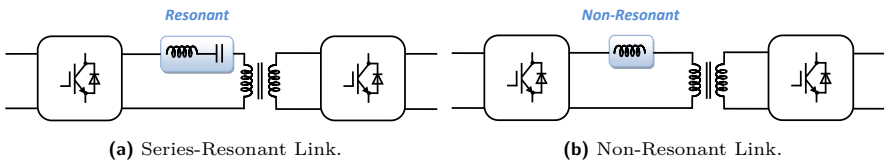


Figure 1.5: Two main topologies for the ac-link of isolated dc-dc converters.

On the one hand, the efficiency of resonant converters is usually higher compared to the hard/soft-switching ones. The capacitance of resonant converters is tuned with the leakage inductance of the transformer, therefore the voltages in the primary and secondary of the transformer are in phase and the only difference comes from the ohmic loss in the transformer windings. The harmonics within the transformer windings, and therefore the losses, are reduced and, due to the synchronization of voltage and current waveforms, soft switching is reached. On the other hand, however, there is a narrow output voltage control which makes them undesirable for some power applications. Besides lack of control margin, there

is usually an extra cost in the construction of the resonant converter due to an external resonant capacitor or, in the case of the LCL topology, a second resonant inductance.

Below, several medium-frequency solutions that can be found in the literature are described only considering the overall topology of the bidirectional isolated dc-dc converter, which will be the core element of indirect-conversion based Power Electronic Transformers.

1.2.1. Traction Transformers

On board transformers are heavy and take up too much of the narrow available space of traction vehicles [Steiner and Reinold, 2007]. Current market requirements demand low-floor solutions (to improve accessibility) or higher useful load capacities [Taufiq, 2007], thus reduced and lighter inverter solutions. Therefore, weight and size constraints in traction transformers are becoming stronger, with the ultimate target of 1 kg/kVA [Hugo et al., 2007].

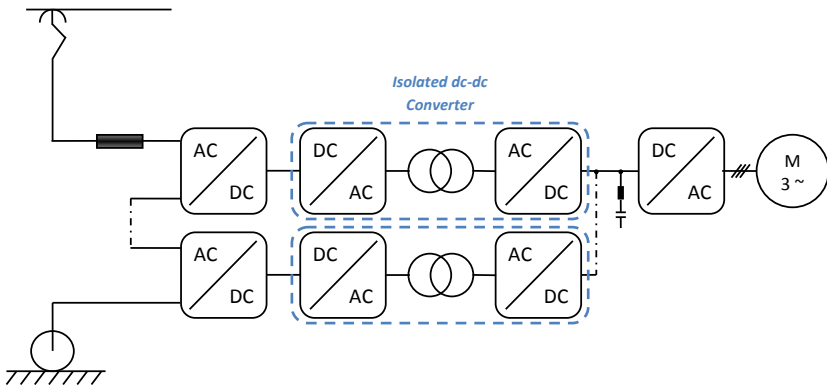


Figure 1.6: Traction converter with MF transformers.

Due to these demanding requirements several Power Electronic Transformer prototypes have already been built [Engel et al., 2003; Heinemann, 2002; Hugo et al., 2007; Steiner and Reinold, 2007; Taufiq, 2007]. This new conversion structures can reduce weight by approximately %50 and volume by %30 [Engel et al.,

2003]. One of the most common structures is introduced in Fig. 1.6, i.e. a cascaded H-bridge topology, which is composed of several stages each of them containing a medium-frequency power transformer. On the high-voltage side, the voltage-source inverters are connected in series while on the dc bus side they are connected in parallel with a common dc bus.

The weight benefits of medium-frequency conversion solutions have been evaluated in comparison with conventional transformer solutions. According to [Steiner and Reinold, 2007], with current semiconductor devices, advantages on these new technologies would only be effective in low-frequency 16 2/3 Hz transformers. In 50 Hz traction transformers, there would not be any significant weight gain due to the higher frequency of the conventional transformer. Moreover, the 25 kV catenary would be a penalty in the number of modular cells.

1.2.2. Offshore Wind Farm Transformers

Offshore wind farms can be located far from the coast where the wind is more constant, thus opening up new opportunities for wind generation. However, so as to reduce the installation cost, the weight and volume of the conversion system has to be reduced compared to actual onshore solutions. Thus, medium-frequency conversion technologies would be appropriate solutions [Meier et al., 2004]. According to [Prasai et al., 2008] the weight and size of a 3 MW 1.2 kHz transformer is less than %8 of an equivalent 50 Hz unit. Moreover, the bidirectional isolated dc-dc converter (see Fig. 1.7) could perfectly fit in a preferable dc configuration of the wind park, both for the interconnection of generators on the wind park [Rufer, 2007a], as well as for the dc connection between the wind park and the electricity grid onshore [Morren et al., 2001]. One of the possible configurations is introduced in Fig. 1.7, where two step up PETs are considered.

The first converter steps-up the voltage to a medium-voltage (MV) dc collection point, and the second one steps-up the common point medium-voltage to a high-voltage (HV) transmission level. However, in terms of power and voltage levels, this second Power Electronic Transformer would suffer serious penalties. A wider analysis with several possible structures, including the one in Fig. 1.7, can be found in [Meyer et al., 2007].

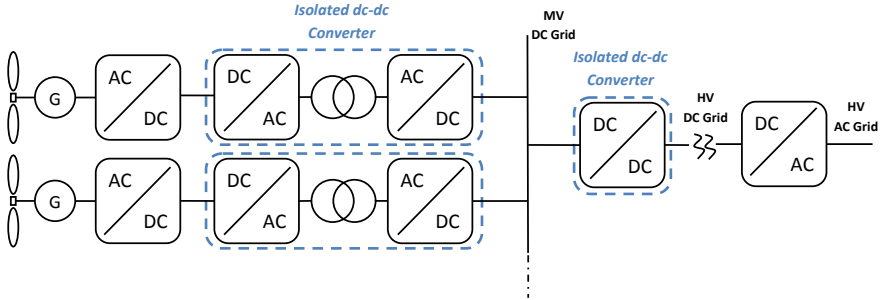


Figure 1.7: Offshore wind farm topology with MF transformers.

1.2.3. Future Flexible Distribution Transformers

In future decentralized grid scenario, balancing of production and consumption will be one of the main concerns. Considering the integration of renewable energy sources, like photovoltaic and wind power, which are intermittent power sources, advanced generation prediction techniques and additional storage technologies will be required [Rufer, 2007b]. Thus to compensate fluctuations from renewable energy sources they can be combined with storage units, which like renewable energy sources need also power electronic adaptation for optimized operation. Due to different voltage ranges PETs can equate voltage levels on both sides, introduce isolation if it is necessary and reduce, therefore, isolation requirements in the low-

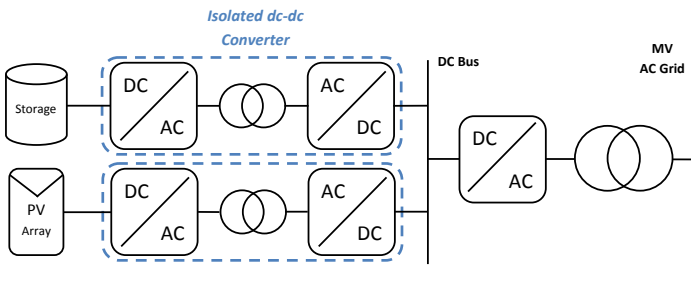


Figure 1.8: Combination of intermittent sources with storage facilities.

voltage side [Fischer et al., 2002]. A simple solution would be the interconnection of both elements on a common dc bus like in Fig. 1.8.

Power Electronic Transformers are also proposed as transmission and distribution transformer substitutes [Bifaretti et al., 2008; Filchev et al., 2004; Heinemann and Mauthe, 2001; Iman-Eini et al., 2008; Lai et al., 2005; Oates and Bassett, 2006], where they could enhance the functionalities of conventional power transformers and achieve flexible ac transmission systems in a future decentralized generation. The introduction of PETs in distribution grids (see Fig. 1.9) could increase power quality and reliability, reducing harmonics, compensating reactive power, avoiding transient transmission or equilibrating voltage differences [Bifaretti et al., 2008].

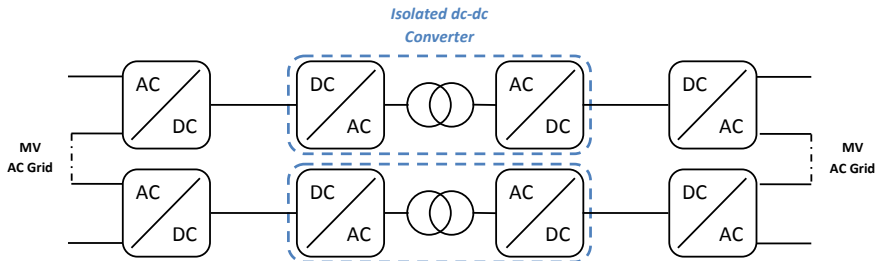


Figure 1.9: Flexible medium-voltage grid with medium-frequency transformers.

The bidirectional isolated dc-dc converter can be used as energy buffer to stabilize power flow in both sides [UNIFLEX] of the medium-voltage ac grid. Moreover, interruptions due to disturbances can be overcome including storage systems that can be easily connected to the dc bus, avoiding frequency adaptation or dc to ac conversion of the storage systems. In addition, it is also possible to provide universal voltage output, such as dc voltage or variable frequency ac voltage to other grids or to the load (see Fig. 1.10).

Apart from the connection of several generators and loads in a common ac grid, the bidirectional dc-dc converter can be used to connect those elements to a common low-voltage (LV) or medium-voltage dc grid [Konishi et al., 2005; Nilsson and Sannino, 2004; Oates and Bassett, 2006] where many conversion steps could be avoided reducing losses and increasing reliability. However, at the moment,

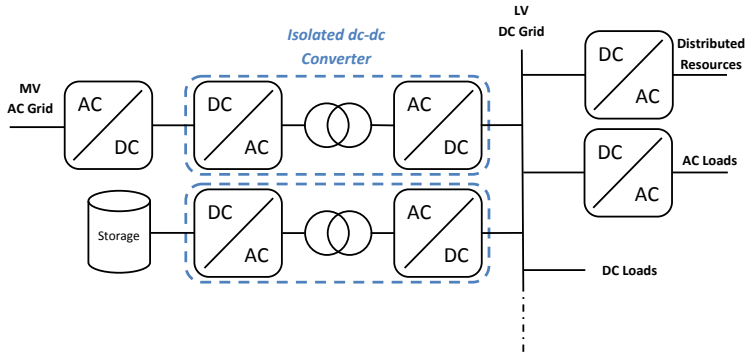


Figure 1.10: Transmission and distribution MF transformers for ac or dc grids.

according to the study carried out on [Oates and Bassett, 2006] the substitution of a conventional transformer with a medium-frequency converter with SiC semiconductors in medium-voltage grids, is still not financially possible because the cost of these new electronic transformers is at least 20 times higher than current solutions. Thus, the incursion of power electronics in distribution grids will only be possible in lower level networks, where available semiconductors could be used without suffering serious penalties.

1.3. Medium-Frequency Power Transformers

Medium-Frequency Power Transformers are the key component of future medium-voltage conversion systems, especially in those with volume and weight restrictions. The increase on operation frequency contributes to a volume and weight reduction, and therefore transformer material is economized. Besides these improvements, conventional transformer problems, like the periodic replacement of oil or dielectric liquid, can be avoided. However, these new medium-frequency power transformers have to deal with various challenges:

- Loss reduction for a new operation point within the frequency range.
- Efficient thermal management, higher power levels are contained in equal volumes.

- High-dielectric stress generated by rapidly changing rectangular voltage waveforms.
- High-isolation levels, usually these transformers are part of a multilevel structure.
- Generation of acoustic noise, which reaches the most sensitive range of the human ear.

Although there are numerous publications in the literature regarding future Power Electronic Transformers, the development, design and characterization of the transformer itself is carried out by a reduced number of research groups, and usually they point out and characterize only part of the process. From the prototypes mentioned in previous sections several general characteristics of currently developed medium-frequency power transformers can be deduced.

In Table 1.1 a summary of these characteristics is illustrated, some of them are physical prototypes, however there are others (*italics*) which present only design characteristics without final prototypes. Nearly all the transformers summarized in Table 1.1 are part of a multilevel cascaded H-bridge converter. The analysis carried out with these transformers is centered, apart from the transformer itself in some cases, on the dc-dc converter whether in its resonant or non-resonant topology. Most of the dc-dc converters are bidirectional, although exceptions are mentioned in the table. Considering the operation principle and the frequency, some general characteristics are described next. Regarding the selection of the magnetic materials, there are three distinctive frequency ranges:

< **1kHz Silicon-Steel (FeSi)** Low-frequency power transformers are made of laminated iron cores due to their high-saturation magnetic induction ($\sim 2\text{T}$) and affordable cost for large-power devices. Although there are some attempts to replace this material with low-loss amorphous cores [METGLAS], i.e. to reduce no-load losses, their price makes them, until present, the best solution for high-power low-frequency applications. Although in the low-range of medium-frequency applications a traction transformer prototype with FeSi has been built [Hugo et al., 2007], a higher working frequency could improve the volume and weight constraints of these solutions.

Frequency	Magnetic Material	Low-Leakage Inductance Resonant Converter	High-Leakage Inductance Non-Resonant Converter
<1 kHz	Silicon-Steel (FeSi)		Traction, 75 kVA 400 Hz, Bare 340 μ H, Oil [Hugo et al., 2007]
1 kHz to 25 kHz	Nanocrystalline	Traction, 350 kVA 10 kHz, Coaxial < 50 kg, 3 μ H, Water [Heinemann, 2002]	General, 10 kVA 20 kHz, Litz wire 1.6 μ H + L_{ext} 21 μ H [Akagi and Inoue, 2006]
		Traction, 500 kW 8 kHz, Coaxial 2.3 μ H, Water, 18 kg [Steiner and Reinold, 2007]	Traction, 1 MVA 4 kHz, Litz wire 215 μ H, 148 kg, Cyclo [Kjellqvist et al., 2004]
	Amorphous	General, 50 kW 25 kHz, Interleaved Foils 3 μ H + L_{ext} 37 μ H [Pavlovsky et al., 2005]	Wind, 280 kVA 1.2 kHz, Coaxial 251 nH, Passive Rectifier [Prasai et al., 2008]
			Wind, 1 MW 10 kHz, HV Litz wire 50 μ H, Passive Rectifier [Morren et al., 2001]
>25 kHz	Ferrite		Wind, 3.6 kW 50 kHz, Litz wire 14 μ H, Passive Rectifier [Morren et al., 2001]
			General, 50 kW 50 kHz, Coaxial 1.6 μ H [Kheraluwala et al., 1992]
			Drives, 25 kW 50 kHz, Litz wire 2.2 mH, Forced Air [Aggeler et al., 2008]

Table 1.1: MF power transformer designs and physical prototypes found in the literature.

1kHz - 25kHz Amorphous and Nanocrystalline Alloys Although silicon-steel remains as the most affordable of magnetic materials, within this frequency range losses are too high for FeSi alloys and amorphous [UNIFLEX],[Meyer et al., 2007] or nanocrystalline alloys [Akagi and Inoue, 2006; Heinemann, 2002; Steiner and Reinold, 2007] are selected. The relatively high-saturation magnetic induction, 1.56 T and ~ 1.2 T respectively, with reduced losses makes them suitable for this frequency range. Besides reduced loss densities, these materials present a constant magnetic behavior with temperature, even for higher temperatures than the admissible one for the other components of the transformer.

> 25kHz Ferrites Ferrites present low-loss densities even in high-frequency applications, which makes them suitable for this frequency range [Aggeler et al., 2008; Morren et al., 2001]. Moreover, their low-saturation magnetic induction (~ 0.5 T) would not be a penalty within these frequencies. In lower frequency applications the required effective cross-sectional area of the core would be a penalty in volume restricted applications. Transformers within this frequency range are part of medium-frequency converters proposed for future semiconductor devices, because current semiconductors for medium-voltage applications will present inadmissible losses within this frequency range. However, even if the converter reaches those frequency ranges efficiently, a wider study will be necessary due to temperature dependent behavior of ferrites.

In Fig. 1.11 the dc magnetic loop and magnetic loss densities for the mentioned materials are represented. The Chan-Vladirimescu Model that will be introduced in subsection 2.3.2 has been used to represent the dc BH loops of Fig. 1.11a. Similarly, the Steinmetz Equation introduced in section 2.3 has been used to represent the comparison among magnetic loss densities of Fig. 1.11b.

As mentioned before, in some low-frequency applications the 3% silicon-steel alloy is replaced with iron-based amorphous alloys. Both materials present a similar BH curve (see Fig. 1.11a), with high permeability and saturation induction values. However, the amorphous material has a narrower dc loop which corresponds to lower loss densities. Moreover, due to the similarity in the BH loop, the frequency behavior of both materials will be almost identical.

Regarding the medium-frequency range, the nanocrystalline material [VIT-

ROPERM] presents lower loss densities than the amorphous material [METGLAS]. Finally, mention that ferrites present low-loss densities. However, in order to highlight their saturation limit (i.e. volume restrictions) the loss density curves in Fig. 1.11b have been plotted referred to their maximum magnetic induction value.

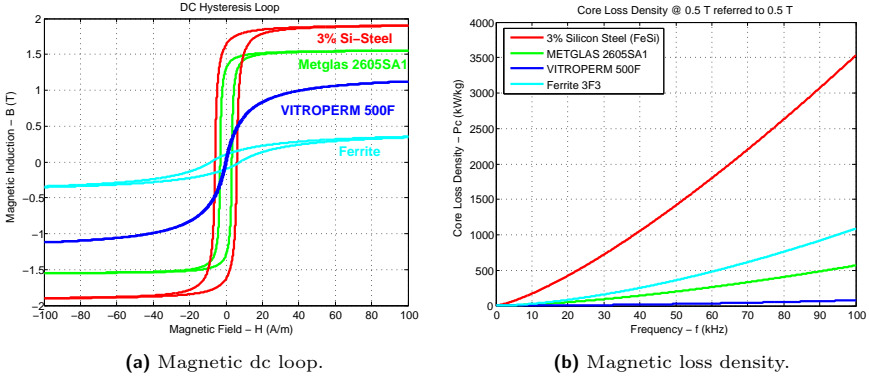


Figure 1.11: Magnetic material comparison.

Regarding the winding, on the other hand, the conductor selection depends normally on the dc-dc converter topology, and therefore on its operation principle.

Low-Leakage Inductance Resonant converters need low and perfectly tuned leakage inductances for proper operation. Interleaved foil conductors [Pavlovsky et al., 2005] or coaxial conductors [Heinemann, 2002; Steiner and Reinold, 2007] present low inductances. In the former, this is due to the fact that magnetic field distribution within the core window, i.e. between foil conductors, is reduced to its maximum, and therefore the stored magnetic energy. In the latter, nearly all the magnetic field is kept within the two conductors. The exterior part of a coaxial cable, i.e. the primary, surrounds the interior part, i.e. the secondary, and the field generated by the primary conductor arrives without leakage paths to the secondary.

High-Leakage Inductance Non-resonant converters or hard/soft-switching ones need a certain value of leakage inductance for proper operation. Leakage

inductance depends mainly on the distance between primary and secondary windings, on the thickness and height of the conductors and on the number of turns. Thus, to keep volume ratios within admissible values for high-leakage inductances the number of turns has to be increased. Coaxial windings or foil conductors have usually one turn in each winding, although some variations can be found in the literature [Kheraluwala et al., 1992; Prasai et al., 2008], therefore, solid conductors or Litz wires with several turns are used to reach the desired value of the leakage inductance. Considering current vs. frequency ranges of medium-voltage medium-frequency applications, solid conductors are usually an unfeasible solution and Litz wires [Aggeler et al., 2008; Akagi and Inoue, 2006] are selected to reduce eddy current effects.

1.4. Motivation of the Present Work

Current high-power semiconductor devices, along with new magnetic materials, enable a potential substitution of bulky low-frequency transformers with new conversion structures. These conversion structures combine fast and efficient switching devices with medium-frequency power transformers. The overall volume of the conversion structure is reduced due to the higher operation frequency of the transformer. In order to reach the desired benefits from these PETs, the characterization of the medium-frequency power transformer is essential.

Although transformer design is not a new subject, voltage and current waveforms, along with power and frequency ranges, of these medium-frequency power transformers demand a reevaluation of convectional transformer characterization and design methodologies. High-power densities, with medium-operational frequencies require new conductor types to face detrimental frequency effects until now not present in high-power applications. Thus, adequate field expressions are necessary to correctly characterize transformer behavior. Moreover, the non-sinusoidal excitation voltages generate magnetic losses that need correct characterization. The reevaluation of conventional characterization expressions and the proposition of appropriate ones for medium-frequency applications, perfectly matches with a new design methodology proposition, in order to verify their validity.

Therefore, this work stems from the need to reevaluate conventional proceedings, in order to create optimized transformer designs in medium-voltage medium-frequency application, and thus, to have a start point for an optimal medium-voltage conversion system.

1.5. Structure of this Document

Within this introductory chapter, the state of the art of Power Electronic Transformers has been introduced with special attention on medium-frequency power transformers. The current and potential applications are listed along with the specific characteristics of the required medium-frequency transformer, which will be the core element of future conversion systems. Once the background of the work has been described, the motivation of the present thesis has been introduced.

In Chapter 2 a wide characterization analysis of medium-frequency power transformers is introduced. The detrimental frequency effects are thoroughly analyzed and appropriate expressions for loss and parasitics introduced, covering various wires and winding arrangements suitable for medium-frequency power transformers. Moreover, a detailed thermal model is introduced where transformer specific characteristics and constraints are taken into account.

In Chapter 3 an optimized design methodology is proposed based on the equations developed in Chapter 2, where the exhaustive analysis carried out enables a straightforward selection of the appropriate equations. The proposed design methodology is suitable for medium-voltage medium-frequency applications. Basic design assumptions are presented and justified, and design steps are clearly presented, ending up by formulating the optimization problem of the transformer.

In Chapter 4, in order to verify the proposed methodology, a case study is introduced, a Dual Active Bridge (DAB) with a medium-frequency power transformer. The design process and the prototyping is described. Experimental measurements are carried out and multiphysical characterization methodologies are verified to conclude the chapter.

Finally, in Chapter 5 the main conclusions and contributions of this thesis will be presented, the achieved objectives will be discussed and future improvements and works will be pointed out.

2

Multiphysical Characterization of Medium-Frequency Power Transformers

Summary

A transformer is mainly composed of winding and core parts. The characterization of both parts is widely analyzed in the literature. However, usually there is a lack of global comparison and validity studies, mostly in medium/high-frequency applications, finding hard to compile information from widely scattered data. This chapter aims to gather the most remarkable methodologies, in order to have a general and clear overview of the possibilities in medium-frequency transformer characterization.

2.1. Introduction

A transformer is a static electrical device that transfers energy from one circuit to another by mutual magnetic coupling.

The transformer is ideal if the magnetic coupling is perfect and the energy transfer lossless, fulfilling the following suppositions:

- The resistance of the winding is zero, there are no losses in the windings.
- The coupling factor is 1, there is no leakage inductance in the transformer.
- The permeability and the resistivity of the core are infinite, there are no losses and there is no energy stored in the core.

However, in practice, the winding resistance is inherent to the constitution of the transformer and it increases with frequency and temperature. Furthermore, even in a perfectly realized winding some of the flux leaks from the common path and does not link the other winding reducing the coupling efficiency. Finally, a minimum amount of current and therefore energy, is necessary to magnetize the transformer due to its finite permeability, this energy will be partially stored and partially dissipated in the core (see Fig. 2.1).

These energy losses reduce transformer efficiency and require an appropriate cooling system design. Therefore, transformer characterization is essential to create optimal energy transfer devices, both in electromagnetic and thermal fields.

Transformer characterization is not a new subject [Hurley et al., 1998]. However, in medium-frequency dc-dc converters the isolation transformer is excited

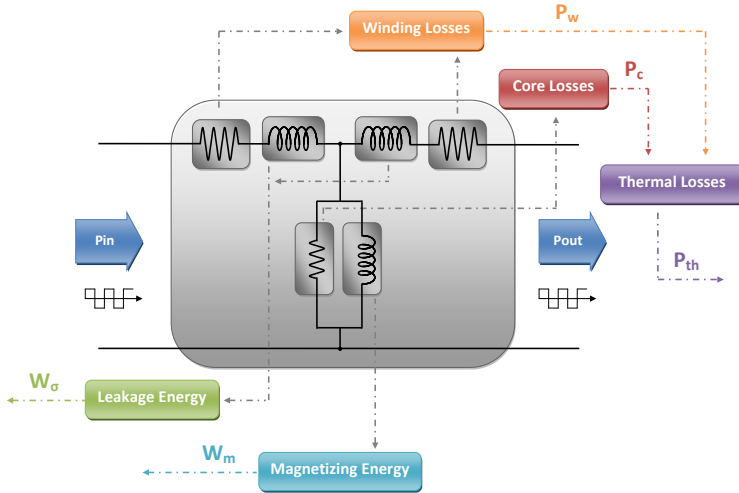


Figure 2.1: Equivalent circuit of a transformer with corresponding loss and energy storing elements.

with non-sinusoidal current and voltage waveforms, requiring more complex expressions. The frequency-dependent behavior of magnetic materials and the redistribution of magnetic fields with frequency, as well as, the utilization of different conductor types to face detrimental frequency effects, has to be correctly characterized to create optimized medium-frequency transformers. Besides power loss characterization, an optimized transformer design requires specific thermal characteristics in order to develop an efficient cooling system.

The first part of this chapter introduces various types of conductors along with their characterization aimed at determining winding-loss expressions and leakage inductance formulas. In the second part, the frequency behavior of magnetic materials and characterization methods are summarized and compared. Finally, in the last part, a complete thermal model of a transformer is detailed.

2.2. Windings and Parasitics

2.2.1. Frequency Effects

The behavior of a transformer can significantly change as frequency increases, due to the redistribution of magnetic field and current density within the conductors. In transformer windings, the magnetic field depends on the current through the conductor itself (skin effect) and the current through neighbor conductors (proximity effect). The depth of these effects within the conductor will depend on the frequency of the waveform.

Skin Effect When a conductor carries an ac current, the magnetic field will not only depend on the amplitude of the current and the radial distance from the center of the conductor, but also on the frequency of the waveform (see Fig. 2.2). The alternating magnetic field generated by the excitation current will induce, according to Lenz’s law, an opposing current in the conductor. Therefore, the current density will be reduced inside the conductor and increased in the surface. The total current in the conductor will not suffer any change, however the current density will not be uniform anymore. The non-uniform distribution of the current

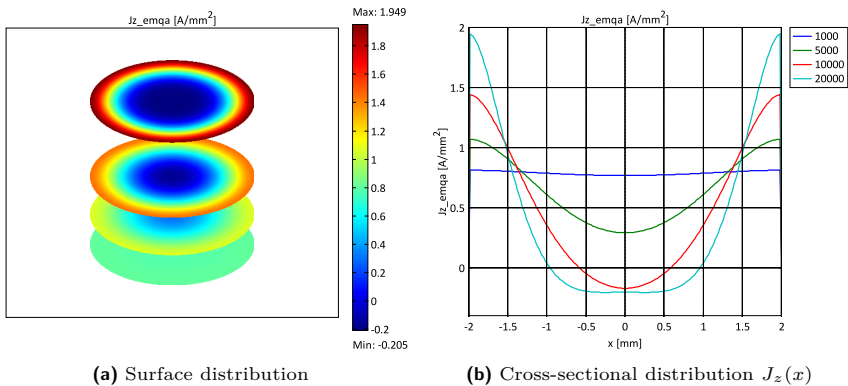


Figure 2.2: Current density in an isolated 4 mm round copper conductor with total net current of 10 A for various frequencies.

density will be much more pronounced with higher frequencies (see Fig. 2.2), due to the linear relationship between frequency and induced current density.

This penetration property of conducting materials is known as skin depth δ , and it is defined as the radial distance from the surface of the conductor where the value of the current density is 37% smaller than its value in the surface (see Table 2.1).

$$\delta = \sqrt{\frac{2}{\omega \mu \sigma}} \quad \text{or} \quad \delta = \sqrt{\frac{\rho}{\pi \mu f}} \tag{2.1}$$

where ω represents the pulsation frequency of the waveform, μ is the permeability of the material and σ the conductivity, or f represents the frequency of the waveform and ρ is the resistivity of the material.

Material	Conductivity (25 °C)	Frequency [kHz]					
		1	2	5	10	20	50
Copper	5.688e7	2.11	1.49	0.94	0.66	0.47	0.29
Aluminium	3.478e7	2.69	1.90	1.20	0.85	0.60	0.38

Table 2.1: Skin depth in mm for common winding materials.

Proximity Effect The ac current that circulates in a wire, generates a magnetic field that enters adjacent conductors and induces voltages on them, resulting in additional current in the conductor. The depth of the penetration will depend on the proximity of the external wire and the frequency of the waveform. The current density in the conductor will be reduced near the external wire and reinforced in the opposite side. The total net current of the conductor does not change, however the current distribution is altered. Thus, any additional conductor within the same external field will suffer from this current even if there is no net current through it.

2.2.2. Winding Losses

Transformer windings suffer from skin and proximity effects. The current distribution within a conductor depends on its current, the surrounding currents, the

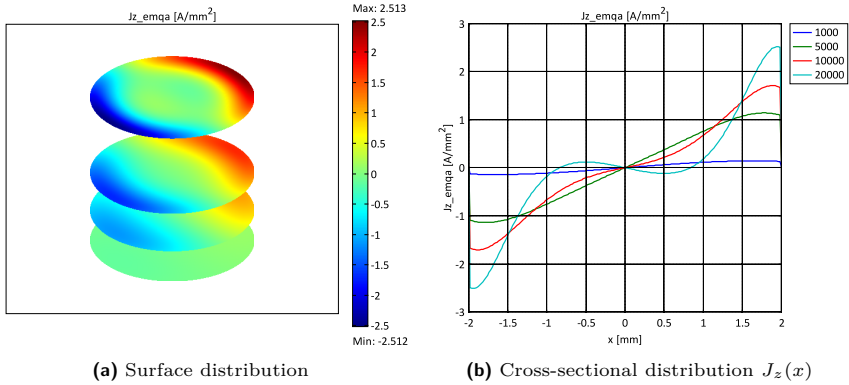


Figure 2.3: Current density in an open circuited 4 mm copper conductor placed within a external field $H_{y_{ext}}$, external magnetic field with only y-component.

type of conductor, the geometry of the winding, and finally the frequency of the waveform. Thus, the determination of conduction losses is not always an easy task. If the winding configuration is simple enough, like foil or coaxial conductors, the resolution of one dimensional field equations (Maxwell equations) is usually sufficient to estimate conduction losses. However, in complex winding arrangements magnetic field distribution, and therefore current density distribution, are highly two dimensional, and analytical solutions become too complex to be solved, requiring usually finite element resolutions.

2.2.2.1. Analytical Approach for Foil Conductors, Dowell's Equation

Although Dowell was not the first one who solved these one dimensional Maxwell equations in winding arrangements [Bennet and Larson, 1940], he was actually the first one solving them specifically for transformer windings, and reaching a closed form expression that is nowadays known as Dowell's expression [Dowell, 1966]. The resolution of these equations and therefore the validity of Dowell's expression is based on the following considerations (see Fig. 2.4):

- One dimensional analysis is directly applicable to foil conductors closed to each other.

- Foil conductors will occupy the whole core window height (y-direction¹) assuring one dimensional field along the core window, $H_y(x)$.
- The magnetic core will have an infinite permeability, thus considering only the field in the transformer window, $H_{core} \approx 0$.

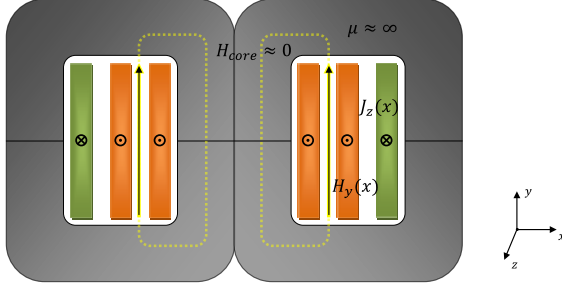


Figure 2.4: Cut view of an EE core transformer with foil windings, infinite permeability magnetic material and one dimensional magnetic field in the core window.

The development of the closed form expression for conduction losses begins with the resolution of the diffusion equation (see Appendix A.1). As conductive materials for winding conductors are linear, the resolution of Maxwell equations is carried out in its time harmonic form using phasors. The magnetic field phasor has only one cartesian component, in our case the y-component (2.2).

$$\mathbf{H}(x) = \mathbf{a}_y H_y(x) \quad (2.2)$$

The magnetic field within foil conductors depends only on the position along the x axis. Therefore, the diffusion equation becomes a second order ordinary differential equation (2.3).

$$\frac{d^2 H_y(x)}{dx^2} = j \sigma \omega \mu H_y(x) = \alpha^2 H_y(x), \quad (2.3)$$

¹The chosen cartesian axis direction is based on the 2D Perpendicular Induction Currents applications mode from COMSOL (a finite element software) to avoid confusion between analytical and finite element comparisons.

where α is the propagation constant

$$\alpha = \frac{(1 + j)}{\delta}. \tag{2.4}$$

The general solution for the hyperbolic equation (2.3) is

$$H_y(x) = H_1 e^{\alpha x} + H_2 e^{-\alpha x}. \tag{2.5}$$

In order to solve this expression, a single foil conductor within a core window is considered. This conductor carries a peak current I , has a thickness d_w , and a height h_w (much larger than its thickness), a length l_w surrounding the core with a negligible curvature and general boundary conditions as the ones presented in Fig. 2.5.

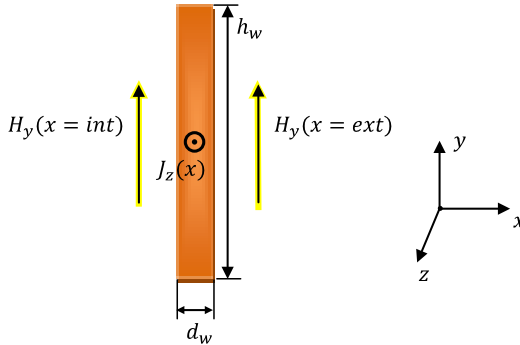


Figure 2.5: Foil conductor carrying a peak current I within a transformer core window, with general boundary conditions.

With this assumptions, a general frequency-dependent expression is reached for the magnetic field distribution within foil conductors (2.6).

$$H_y(x) = H_{ext} \frac{\sinh(\alpha x)}{\sinh(\alpha d_w)} - H_{int} \frac{\sinh(\alpha (x - d_w))}{\sinh(\alpha d_w)} \tag{2.6}$$

Once the one dimensional magnetic field is defined, the current density can be determined (2.7).

$$\nabla \times \mathbf{H} = \mathbf{J} \Rightarrow \mathbf{a}_z \frac{\partial H_y(x)}{\partial x} = \mathbf{J} \Rightarrow \frac{dH_y(x)}{dx} = J_z(x) \quad (2.7)$$

Therefore, deriving the magnetic field expression (2.6) the frequency-dependent current density in a foil conductor is obtained (2.8).

$$J_z(x) = \alpha H_{ext} \frac{\cosh(\alpha x)}{\sinh(\alpha d_w)} - \alpha H_{int} \frac{\cosh(\alpha(x - d_w))}{\sinh(\alpha d_w)} \quad (2.8)$$

As illustrated in Fig. 2.6b, the current density increases as the number of foils is also raised. The first conductor does not suffer from an external field on its left-hand side (see Fig. 2.6a), and consequently the distribution of the current density depends only on its own current (skin effect). In contrast, the second conductor has an external field on its left-hand side and counteracts with an opposed sign current near the first layer. As the total net current does not change, there is a high concentration in the opposite side of the second foil in order to balance the total current (proximity effect).

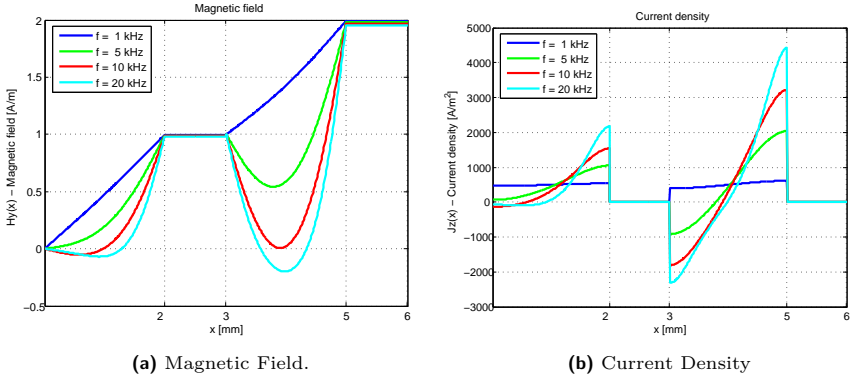


Figure 2.6: Magnetic field and current density in a two layer winding for various frequencies, with $d_w = 2$ mm and 1 mm of inter-layer space. Boundary conditions (H_{int} , H_{ext}): (0, 1) and (1, 2) for the first and second layer, respectively.

From the expression of the current density, the frequency-dependent conduction losses in foil windings are determined (2.9).

$$P_{\sigma} = \frac{1}{\sigma} \int_V \mathbf{J} \cdot \mathbf{J}^* \, dv \quad (2.9)$$

A simplified expression for ohmic losses P_{σ} is rewritten and solved (2.10).

$$P_{\sigma} = \frac{1}{2\sigma} \int_V |J_z^2(x)| \, dv = \frac{1}{2\sigma} \int_{x=0}^{x=d_w} |J_z^2(x)| h_w l_w \, dx \quad (2.10)$$

Finally, and after some mathematical developments (see Appendix A.1), conduction losses in a conduction layer, placed in a transformer window, are represented with a closed form expression (2.11).

$$P_{\sigma} = \frac{l_w h_w}{2\delta\sigma} \left[(H_{ext} - H_{int})^2 \frac{\sinh(2\Delta) + \sin(2\Delta)}{\cosh(2\Delta) - \cos(2\Delta)} + 2 H_{int} H_{ext} \frac{\sinh(\Delta) - \sin(\Delta)}{\cosh(\Delta) + \cos(\Delta)} \right] \quad (2.11)$$

where $\Delta = d_w/\delta$ represents the penetration ratio.

In this expression (2.11) two parts can be clearly distinguished, the one generated by the conductor itself representing the skin effect (left-hand side of the expression within the brackets), and the one generated from the interaction of the fields representing the proximity effect (right-hand side). From this expression two factors are determined, the skin and proximity effect factors, ς_1 and ς_2 respectively.

$$\varsigma_1 = \frac{\sinh(2\Delta) + \sin(2\Delta)}{\cosh(2\Delta) - \cos(2\Delta)} \quad \text{and} \quad \varsigma_2 = \frac{\sinh(\Delta) - \sin(\Delta)}{\cosh(\Delta) + \cos(\Delta)} \quad (2.12)$$

Now, if a winding is composed of several consecutive layers, the boundary conditions in each side of the p^{th} foil conductor will be defined with the following two expressions,

$$H_{int} = (p-1) \frac{I}{h_w} \quad H_{ext} = p \frac{I}{h_w} \quad (2.13)$$

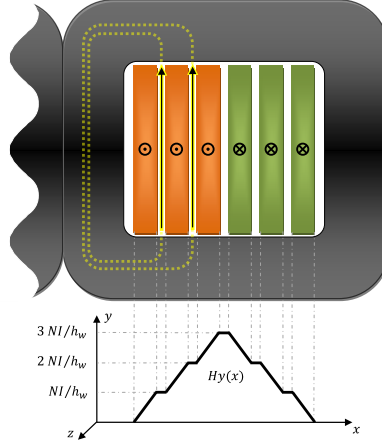


Figure 2.7: Transformer winding with several primary and secondary layers and equivalent dc magnetic field distribution within foil conductors according to Ampere's circuital law.

where H_{int} represents the field generated by the previous $p - 1$ layers and H_{ext} represents all the field generated by the p layers (see Fig. 2.7).

Substituting (2.13) in (2.11), simplifying according to (2.12) and summing up the losses of all the m layers of the winding $P_w = \sum_{p=1}^m P_{\sigma}$, the total ohmic losses of a winding will be

$$P_w = I^2 \frac{l_w}{2\delta\sigma h_w} m \left[\varsigma_1 + \frac{2}{3} (m^2 - 1) \varsigma_2 \right] \quad (2.14)$$

As mentioned before, each foil conductor is carrying a peak current I . Furthermore, power losses in resistive elements are determined from their resistance R_{ac} and the rms current through them I_n .

$$P_w = R_{ac} I_n^2 = R_{ac} \frac{1}{2} I^2 \quad (2.15)$$

Equating the conduction loss expression (2.14) with (2.15), the total ac resistance of the winding is determined (2.16).

$$R_{ac} = \frac{l_w}{\delta \sigma h_w} m \left[\varsigma_1 + \frac{2}{3} (m^2 - 1) \varsigma_2 \right] \quad (2.16)$$

The dc resistance of a winding composed of foil conductors is

$$R_{dc} = \frac{l_w}{d_w \sigma h_w} m , \quad (2.17)$$

from these expressions Dowell's resistance factor F_r , which represents the relationship between total ac resistance and total dc resistance, $R_{ac} = F_r R_{dc}$, can be deduced (2.18).

$$F_r = \Delta \left[\varsigma_1 + \frac{2}{3} (m^2 - 1) \varsigma_2 \right] \quad (2.18)$$

In Fig. 2.8 the resistance factor is illustrated for different penetration ratios Δ and for different number of layers. For high penetration ratios the total resistance of the winding rapidly increases. Below $\Delta = 1$ losses can be also considerable if windings with large number of layers are considered. For example, a four layer winding composed of $d_w = 2$ mm copper foil conductors carrying a sinusoidal

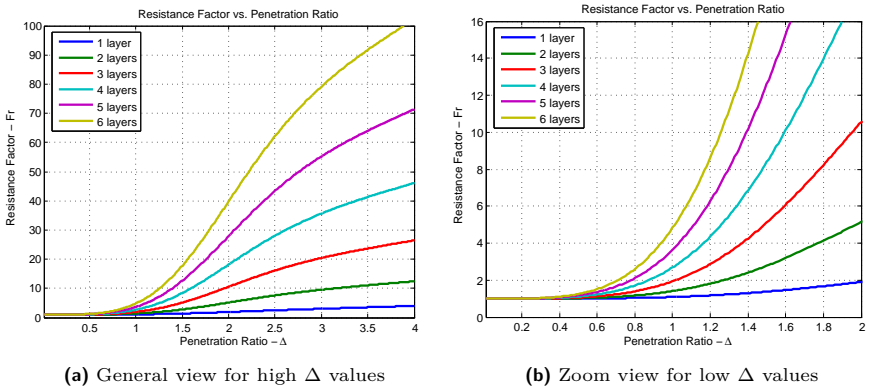


Figure 2.8: Dowell resistance factor expression F_r , versus penetration ratio.

current at 1 kHz (see Table 2.1) will present ~ 2.7 times higher losses than its dc counterpart.

The resistance factor expression was introduced by Dowell and equation (2.18) is one of its variants [Dowell, 1966]. From this closed form expression, losses in foils windings can be directly determined. Nevertheless, it is important to notice that the assumptions made at the beginning of the section must be accomplished in order to achieve a certain level of accuracy. If a different winding arrangement is considered, like interleaving primary and secondary foil conductors, separate consecutive layers can be considered and sum up, or otherwise, expression (2.11) should be reevaluated, in order to get a new compact expression.

2.2.2.2. Dowell's Porosity Factor

Although for some applications foil conductors are practical solutions, winding layers are usually composed of round or rectangular conductors, and sometimes they do not extend the full core window. For those cases Dowell introduced in the same analysis a parameter that accounted for these variations: the porosity factor η_w . This factor relates round, rectangular or short foil conductors with their equivalent whole window foil conductor (see Fig. 2.9).

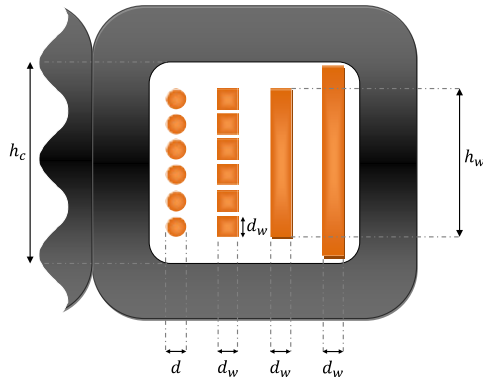


Figure 2.9: Representation of the equivalent foil conductor, from round conductors to equivalent square conductors to equivalent foil conductors and finally to whole window foil conductors.

In the case of round conductors, an equivalent square conductor (see Fig. 2.9), with the same conducting area (2.19) is defined.

$$d_w = \sqrt{\frac{\pi}{4}} d \quad (2.19)$$

For equivalent square conductors or rectangular ones, an equivalent foil conductor is determined, which has the same height as the whole conducting layer (see Fig. 2.9). However, in this second equivalence, the effective conductive surface is increased, thus an equivalent conducting material is defined (2.20) which generates an equal magnetic field along the enclosed winding path.

$$\sigma' = \eta_w \sigma \quad (2.20)$$

where η_w is known as the porosity factor and it is determined in this case according to (2.21).

$$\eta_{w1} = \frac{N d_w}{h_w} \quad (2.21)$$

where N represents the number of turns in one layer.

Finally, for equivalent or originally short foil conductors, the conductive layer is extended to fill the whole window height and a second porosity factor (2.22) is determined.

$$\eta_{w2} = \frac{h_w}{h_c} \quad (2.22)$$

Therefore, equation (2.18) becomes

$$F_r = \Delta' \left[\zeta'_1 + \frac{2}{3} (m^2 - 1) \zeta'_2 \right] \quad (2.23)$$

with $\Delta' = \sqrt{\eta_w} \Delta$ and

$$\zeta'_1 = \frac{\sinh(2\Delta') + \sin(2\Delta')}{\cosh(2\Delta') - \cos(2\Delta')} \quad \text{and} \quad \zeta'_2 = \frac{\sinh(\Delta') - \sin(\Delta')}{\cosh(\Delta') + \cos(\Delta')} \quad (2.24)$$

The physical validity of the porosity factor has been questioned in several publications [Ferreira, 1994], [Robert et al., 2000], [Nan and Sullivan, 2003], [Reatti

and Kazimierczuk, 2002], however its precision as a correction factor has been reinforced.

In [Ferreira, 1990], for instance, a remark was made concerning the physical validity of the factor, and it was proposed, if it was to be used, the application of the porosity factor as a compensation term also for the magnetic field (2.25), in order to eliminate the geometrical dependency of the skin depth introduced by Dowell.

$$F_r = \Delta' \left[\varsigma_1' + \eta_w^2 \frac{2}{3} (m^2 - 1) \varsigma_2' \right] \quad (2.25)$$

A part from the previous remark, [Ferreira, 1990] proposed another closed form expression for round conductors derived from the exact solution of an isolated round conductor [Lammeraner and Štafl, 1966] and based on the orthogonality between skin and proximity effects [Ferreira, 1990]. In the proposed expression (2.26) the skin effect is characterized with the exact solution of the magnetic field in an isolated round conductor and the proximity effect, with the exact solution of an external magnetic field in a round conductor.

$$F_r = \frac{\gamma}{2} \left[\tau_1 - 2\pi \frac{4(m^2 - 1)}{3} \tau_2 \right] \quad (2.26)$$

with

$$\begin{aligned} \tau_1 &= \frac{\text{ber}(\gamma) \text{bei}'(\gamma) - \text{bei}(\gamma) \text{ber}'(\gamma)}{\text{ber}'(\gamma)^2 + \text{bei}'(\gamma)^2} \\ \tau_2 &= \frac{\text{ber}_2(\gamma) \text{ber}'(\gamma) + \text{bei}_2(\gamma) \text{bei}'(\gamma)}{\text{ber}'(\gamma)^2 + \text{bei}'(\gamma)^2} \end{aligned} \quad (2.27)$$

and

$$\gamma = \frac{d}{\delta \sqrt{2}} = \frac{\sqrt{2} r}{\delta} \quad (2.28)$$

where bei and ber are Kelvin functions, i.e. real and imaginary parts, respectively, of Bessel functions of the first kind (see Appendix A.3).

In order to improve the accuracy of the expression proposed by Ferreira (2.26), [Reatti and Kazimierczuk, 2002] introduced the porosity factor in the equation as a correction term for the magnetic field, like Ferreira himself did for Dowell's

expression (2.25).

$$F_r = \frac{\gamma}{2} \left[\tau_1 - 2\pi\eta_w^2 \left(\frac{4(m^2 - 1)}{3} + 1 \right) \tau_2 \right] \quad (2.29)$$

The good predictions provided by Dowell’s expression and the porosity factor were pointed out already in [Ferreira, 1994] for tightly packed windings $\eta_w > 0.7$. More recently various papers with comparisons and validity ranges have been published [Dimitrakakis and Tatakis, 2008; Dimitrakakis et al., 2007; Nan and Sullivan, 2003; Robert et al., 2001]. The accuracy of Dowell’s expression was pointed out once more for tightly packed windings, as well as the overestimation of Ferreira based models (see Table 2.2). The exact solution of Ferreira’s method is only accurate for isolated round conductors, when the round conductors are getting close to each other, the effect between turns in each layer is not considered and the representation introduced by Dowell (with its equivalent square and foil conductors) is more precise, and much more simple.

Table 2.2 summarizes the study carried out in [Dimitrakakis et al., 2007] and [Dimitrakakis and Tatakis, 2008]. The reduced error in Dowell’s expression usually occurs when the skin depth is in the order of the diameter of the conductor ($\Delta \simeq 1$) [Nan and Sullivan, 2003], [Dimitrakakis et al., 2007]. However, for large penetration ratios the error, as illustrated in Table 2.2, is higher (highest error in each range).

Porosity Factor	Round Conductors		Rectangular Conductors
	Dowell	Ferreira Modified	Dowell
$\eta_w > 0.7$	< 5%	15% – 140%	Accurate
$0.7 > \eta_w > 0.6$	5% – 15%	8% – 70%	< 15%
$0.6 > \eta_w > 0.5$	5% – 30%	5% – 50%	20% – 40%

Table 2.2: Comparison of the relative percentage error of two closed form expressions and for different porosity factors.

Based on these statements, most recent publications related to winding losses,

focus on the improvement of Dowell's expression with finite element tools [Dimitrakakis et al., 2007; Nan and Sullivan, 2003; Robert et al., 2001]. They propose modified expressions with several correction factors or weighting parameters based on tens of finite element simulations, depending on turn-to-turn distance, layer-to-layer distance or edge-to-core distance and skin depth. On the one hand, propositions in [Nan and Sullivan, 2003] and [Robert et al., 2001] are based on complicated look-up tables. On the other hand, in [Dimitrakakis et al., 2007] a polynomial expression is introduced, however the conditions in which finite element simulations were carried out make the expression too limited, lacking a real applicability.

As a conclusion, it should be noted, if high-power densities are to be reached, windings will be tightly packed and Dowell's expression with the corresponding porosity factor will be precise enough. Nevertheless, for non conventional winding arrangements, finite element simulations should be used, because even if there are several winding arrangements summarized and characterized in [Nan and Sullivan, 2003] and [Robert et al., 2001], they do not cover every possible winding arrangement.

2.2.2.3. Round Litz Wire

In medium-frequency applications skin and proximity effects can be considerable. Thus, to handle the power density of medium-frequency transformers a certain effective conductor area is necessary. However this area can be too wide for the frequency of the waveform due to eddy current effects. The use of stranded insulated and twisted wires reduces these effects. If the wire is correctly twisted, each strand takes each of the places in the bundle (see Fig.2.10) and therefore the effect between strands is reduced. Moreover, the reduced surface area of each strand reduces the penetration ratio for the same skin depth. Conductors made up of multiple individually insulated strands twisted together are known as Litz wires.

In Litz wire windings skin and proximity effects can be divided in strand and bundle-level effects [Sullivan, 1999] (see Fig.2.11). Bundle-level effects, related to currents circulating in paths involving multiple strands, are controlled by the cor-

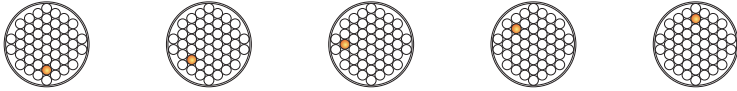


Figure 2.10: Representation of the position variation of a strand in a Litz bundle.

direct construction of the Litz wire. Bundle-level proximity loss is controlled by simple twisting, however bundle-level skin effect requires more complex constructions [Sullivan, 1999]. At strand level, related to individual strands, proximity effect dominates over skin effect in windings with high number of layers, and usually strand-level skin effects are negligible. Strand-level proximity losses can be further divided in internal and external losses. Internal proximity losses are related to the losses generated by the rest of the strands in the bundle, and external proximity losses express the losses generated from current in the rest of the bundles.

Usually equal currents in all strands are assumed in order to calculate losses in Litz wire windings. This assumption is equivalent to assuming that the bundle-level construction has been chosen properly to control bundle-level proximity and skin effects. Therefore, to calculate the total strand-level proximity-effect loss in a

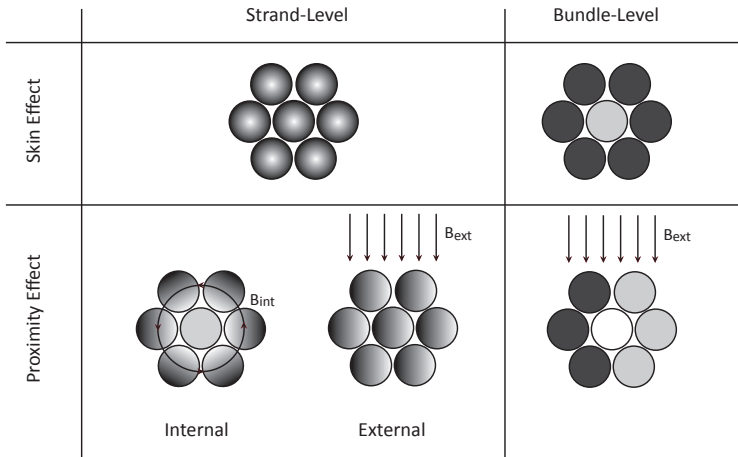


Figure 2.11: Type of eddy currents in Litz conductors. Illustration introduced in [Sullivan, 1999].

Litz winding, the whole winding is supposed to be composed of $n_s N$ turns, each one carrying an equal current I/n_s , where n_s is the number of strands, N the number of bundle-turns and finally I the current in a bundle.

In Fig. 2.12a an isolated Litz wire is represented, in which each strand is carrying the same total current, the internal proximity effect is clearly the main eddy current effect and the strand-level skin effect is almost negligible. In Fig. 2.12b, in contrast, a single Litz wire is represented without a net current but within an external magnetic field, in order to illustrate the external proximity effect. In Fig. 2.12c the same Litz bundle is carrying a net current within an external magnetic field, and both effects are illustrated.

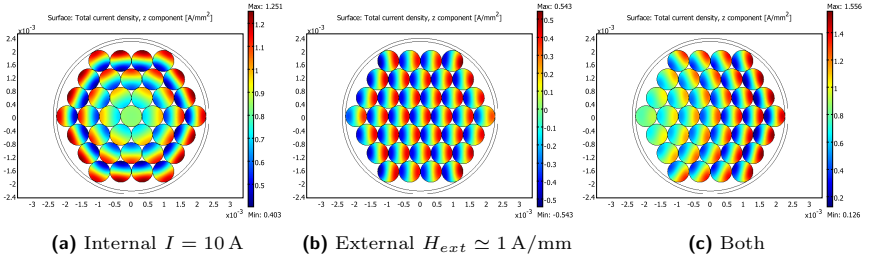


Figure 2.12: Total current density in a single round Litz wire $d_b = 4.5$ mm, with 37 strands of $d_s = 0.64$ mm and $f = 20$ kHz.

Due to the orthogonality principle between proximity and skin effects, losses in Litz bundles can be calculated separately, an approach followed in several publications.

Conduction losses in isolated Litz bundles, i.e. skin effect losses and internal proximity effect losses, were already determined in [Lammeraner and Štafl, 1966]. In [Ferreira, 1992] the same approach is followed but instead of reducing the expression to low penetration ratios, the complete equation already developed in [Lammeraner and Štafl, 1966] for single solid round conductors is used. And finally in [Lotfi and Lee, 1993] the exact Bessel equations are used, according to [Lotfi and Lee, 1993] in order to improve accuracy in high-frequency applications.

Skin Effect Losses are determined from the one-dimensional solution developed for round conductors [Lammeraner and Štafl, 1966], reaching in the case of an isolated strand (2.30).

$$P_{s_{skin}} = R_{s_{dc}} \frac{\gamma}{4} I_s^2 \tau_1(\gamma) \quad (2.30)$$

where I_s represents the current in a single strand and the dc resistance of the strand $R_{s_{dc}}$ is determined from (2.31).

$$R_{s_{dc}} = \frac{l_s}{\pi \sigma r_s^2} \quad (2.31)$$

where l_s is the total length and r_s the radius of a single strand.

Therefore, the strand-level skin effect losses in a Litz bundle will be

$$P_{skin} = R_{dc} \frac{\gamma}{4} I^2 \tau_1(\gamma) = \frac{R_{s_{dc}}}{n_s} \frac{\gamma}{4} I^2 \tau_1(\gamma) \quad (2.32)$$

because all the strands within a Litz bundle are in parallel.

The difference between previously mentioned publications lies in the term $\tau_1(\gamma)$. On the one hand, the expression introduced in [Ferreira, 1992] uses the equation already introduced in (2.27), where

$$\tau_1(\gamma) = \frac{\text{ber}(\gamma) \text{bei}'(\gamma) - \text{bei}(\gamma) \text{ber}'(\gamma)}{\text{ber}'(\gamma)^2 + \text{bei}'(\gamma)^2} \quad (2.33)$$

On the other hand, and considering the aims of the utilization of Litz wires, [Lammeraner and Štafl, 1966] reduces the expression to low penetration ratios reaching (2.34).

$$\tau_1(\gamma) = \frac{2}{\gamma} + \frac{\gamma^3}{96} \quad (2.34)$$

And finally in [Lotfi and Lee, 1993] the exact solution for solid round conductors is used with modified Bessel functions of the first kind of zero and first order, I_0 and I_1 respectively.

$$\tau_1(\gamma) = \frac{1}{\sqrt{2}} \Re \left[(1+j) \frac{I_0(\alpha r_s)}{I_1(\alpha r_s)} \right] \quad (2.35)$$

A comparison example is illustrated in Fig. 2.13, where the three expressions are evaluated along with a finite element simulation of a single isolated strand $d_s = 0.2$ mm. For low penetration ratios ($\Delta < 2$) all of the expressions are accurate. However, for large penetration ratios ($\Delta > 2$), the error obtained with the reduced expression (2.34) increases with the increase of the penetration ratio.

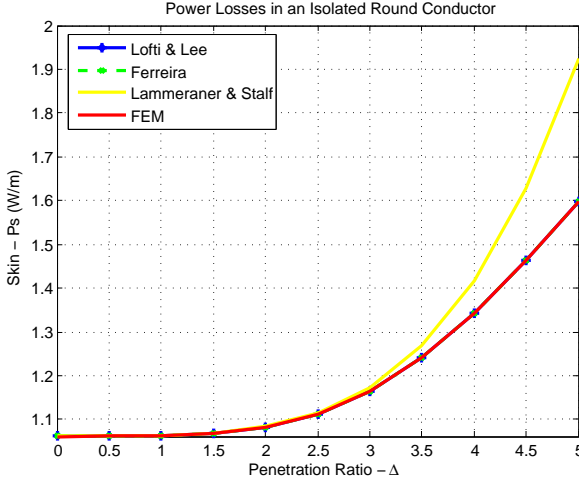


Figure 2.13: Comparison of different expressions for the determination of skin effect losses in an isolated round conductor with $d_s = 0.2$ mm.

Internal Proximity Effect Losses are also evaluated in previously mentioned publications, and once more they follow the same approach.

Internal proximity effects are determined considering the field generated by the strands of the bundle at each radial position $H_0(r)$, and applying this field as an external transverse magnetic field to each of the strands (according to their geometrical position as shown in Fig. 2.14).

The general power loss expression for single round conductors subjected to an

external transverse magnetic field is [Lammeraner and Štafl, 1966],

$$p_{s_{internal}}(r) = -\frac{2\pi\gamma}{\sigma} H_0^2(r) \tau_2(\gamma) \quad (2.36)$$

The field generated by the strands in the bundle at each radial position can be obtained by modifying the expression for solid round wires

$$H_0(r) = \frac{I}{2\pi r n_s} \left(\frac{r}{r_s}\right)^2 p_f \quad (2.37)$$

where $p_f = n_s (r_s/r_b)^2$ is the packing factor.

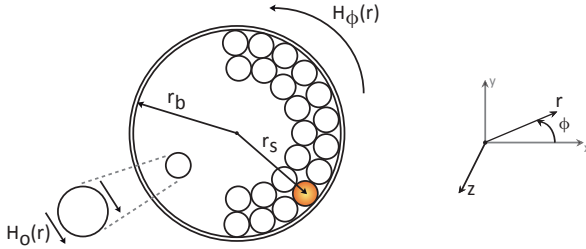


Figure 2.14: Litz bundle, the radial position of each strand is considered to apply the radial dependent internal magnetic field.

Rather than discrete summation of losses in each strand, the integration of internal losses per unit area results in

$$P_{s_{internal}} = -\frac{2\pi\gamma}{\sigma} \frac{n_s I^2 l_s}{8\pi^2 r_b^2} \tau_2(\gamma) \quad (2.38)$$

Once more, the difference between previously mentioned developments lies in the term $\tau_2(\gamma)$. On the one hand, the expression introduced in [Ferreira, 1992] uses the equation already introduced in (2.27), where

$$\tau_2(\gamma) = \frac{\text{ber}_2(\gamma) \text{ber}'(\gamma) + \text{bei}_2(\gamma) \text{bei}'(\gamma)}{\text{ber}'(\gamma)^2 + \text{bei}'(\gamma)^2} \quad (2.39)$$

On the other hand, [Lammeraner and Štafl, 1966] reduces the expression for low penetration ratios reaching

$$\tau_2(\gamma) = -\frac{\gamma^3}{16} \quad (2.40)$$

and finally in [Lotfi and Lee, 1993] the modified Bessel functions of the first kind of zero and first order are used.

$$\tau_2(\gamma) = \frac{1}{\sqrt{2}} \frac{\Re[(1-j)I_0(\alpha r_s)I_1^*(\alpha r_s)]}{|I_0(\alpha r_s)|^2} \quad (2.41)$$

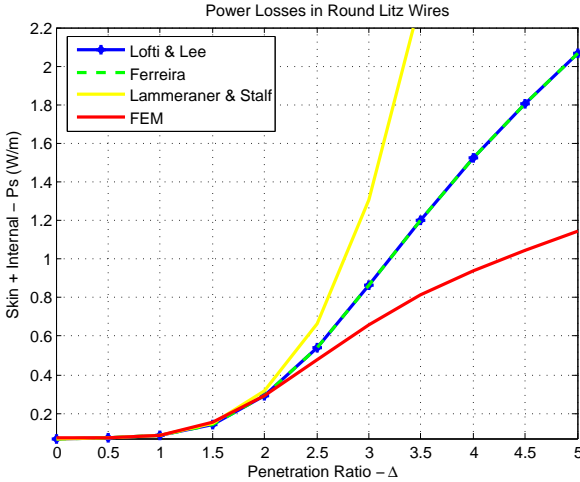


Figure 2.15: Comparison of different expressions for the determination of internal proximity losses in a single isolated Litz bundle with $d_b = 4.5$ mm and 37 strands of $d_s = 0.64$ mm.

A comparison example is illustrated in Fig. 2.15, along with a finite element simulation of a single isolated Litz bundle with $d_b = 4.5$ mm and 37 strands of $d_s = 0.64$ mm. For low penetration ratios ($\Delta < 2$) all the expressions are precise enough. However, for large penetration ratios even the most detailed of the expressions (2.41) overestimates the losses. It should be noticed that both the strand level skin effect and the internal proximity effect are evaluated.

In the case of internal proximity effect losses, the simplest of the expressions is accurate enough, large penetration ratio errors are due to the non circular nature of the field (see Fig. 2.16a to Fig. 2.16c). Therefore, the accuracy in the determi-

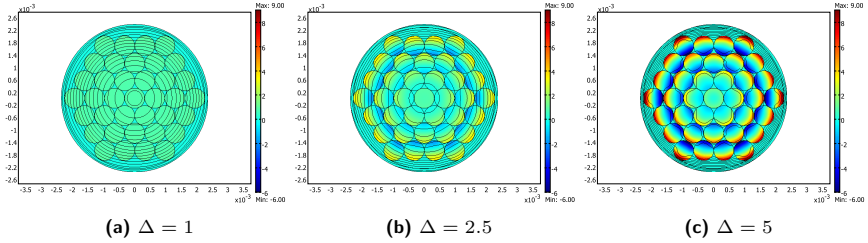


Figure 2.16: Total current density and magnetic field lines in a single isolated Litz bundle $d_b = 4.5$ mm, with 37 strands of $d_s = 0.64$ mm for different penetration ratios.

nation of the losses in an isolated strand does not improve the global prediction, due to the fact that the external magnetic field in each of the strands is no longer one dimensional.

External Proximity Effect Losses are determined, from the exact solution of an isolated round conductor within an external field [Ferreira, 1992]. Although among previously mentioned publications, external proximity effect losses in Litz bundles are only evaluated in [Ferreira, 1992], an extrapolation of the other methods can also be done using each of the expressions for $\tau_2(\gamma)$. Therefore, the external proximity effect losses in a Litz bundle within an external magnetic field are

$$P_{external} = -\frac{2\pi\gamma}{\sigma} n_s H_e^2 \tau_2(\gamma) \quad (2.42)$$

A comparison example is illustrated in Fig. 2.17, where the three expressions are evaluated along with a finite element simulation of a single open circuited Litz bundle $d_b = 4.5$ mm, with 37 strands of $d_s = 0.64$ mm, within an external magnetic field $H_e = 1$ A/mm.

For low penetration ratios ($\Delta < 2$) all the expressions are precise enough. However, for large penetration ratios, like in the case of skin effect losses, the reduced expression overestimates the losses.

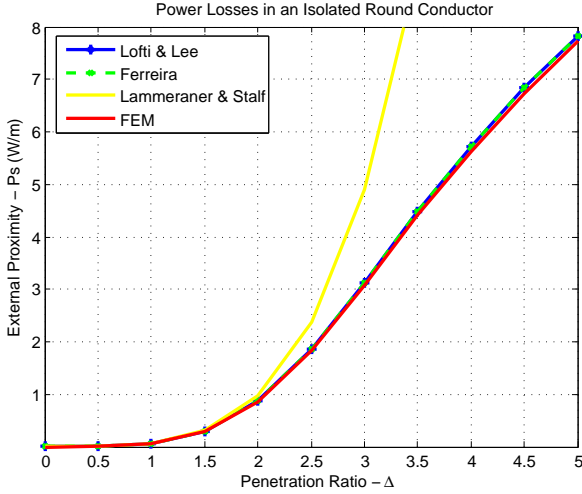


Figure 2.17: Comparison of different expressions for the determination of external proximity losses in an open circuited Litz bundle $d_b = 4.5$ mm, with 37 strands of $d_s = 0.64$ mm, within an external magnetic field $H_e = 1$ A/mm for different penetration ratios.

In Fig. 2.18 the difference between several penetration ratios is illustrated for an open circuited Litz bundle within an external magnetic field $H_e = 1$ A/mm.

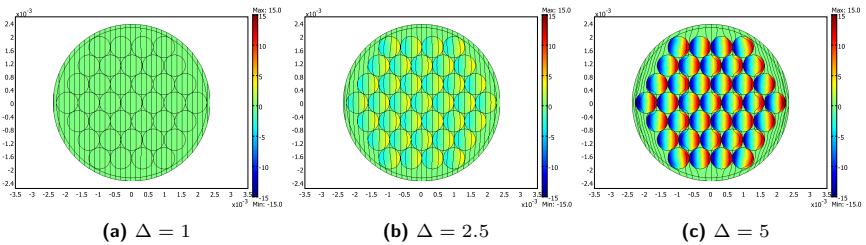


Figure 2.18: Total current density and magnetic field lines in an open circuited Litz bundle $d_b = 4.5$ mm, with 37 strands of $d_s = 0.64$ mm, within an external magnetic field $H_e = 1$ A/mm for different penetration ratios.

Although the analysis carried out for external magnetic fields is accurate, the

difficulty for its use lies in the fact that first the field within the transformer window has to be evaluated, and then applied in this last expression as an external magnetic field. This case is analyzed in various previous publications, for instance [Bartoli et al., 1996] and [Tourkhani and Viarouge, 2001]. The profile of the magnetic field within the transformer window is the same as the one introduced in Fig. 2.7, which increases linearly in each layer and remains constant within the inter-layer space.

In the former, [Bartoli et al., 1996], the development carried out in [Ferreira, 1992] is taken as a reference, (2.33) and (2.39), and two porosity factors are applied (2.43), like in the correction proposed for round conductors (2.29).

$$P_w = \frac{I^2}{2} R_{dc} \frac{\gamma}{2} \left[\frac{1}{n_s} \tau_1(\gamma) - 2\pi \left(\frac{4(m^2 - 1)}{3} + 1 \right) n_s \left(\eta_1^2 + \eta_2^2 \frac{p_f}{2\pi n_s} \right) \tau_2(\gamma) \right] \quad (2.43)$$

with η_1 being the external porosity factor and η_2 the internal porosity factor (2.44).

$$\eta_1 = \frac{d_s}{t_b} \sqrt{\frac{\pi}{4}} \quad \text{and} \quad \eta_2 = \frac{d_s}{t_s} \sqrt{\frac{\pi}{4}} \quad (2.44)$$

where t_b is the distance between the centers of two adjacent Litz bundles and t_s is the distance between the centers of two adjacent strands.

R_{dc} refers to the dc resistance of the whole winding (2.45), and m represents the number of layers in the winding.

$$R_{dc} = \frac{N l_s}{n_s \pi \sigma r_s^2} \quad (2.45)$$

In the latter, [Tourkhani and Viarouge, 2001], like in the previous case, Kelvin functions are used to determine the skin and proximity effect factors, $\tau_1(\gamma)$ and $\tau_2(\gamma)$ respectively. However, in this case, depending of the geometrical position of the Litz bundle, the external field is determined in each of the strands and all the losses in all the bundles are added reaching the final expression for the losses in the whole winding (2.46).

$$P_w = \frac{I^2}{2} R_{dc} \frac{\gamma}{2} \left(\tau_1(\gamma) - \frac{\pi^2 n_s p_f}{24} \left(16 m^2 - 1 + \frac{24}{\pi^2} \right) \tau_2(\gamma) \right) \quad (2.46)$$

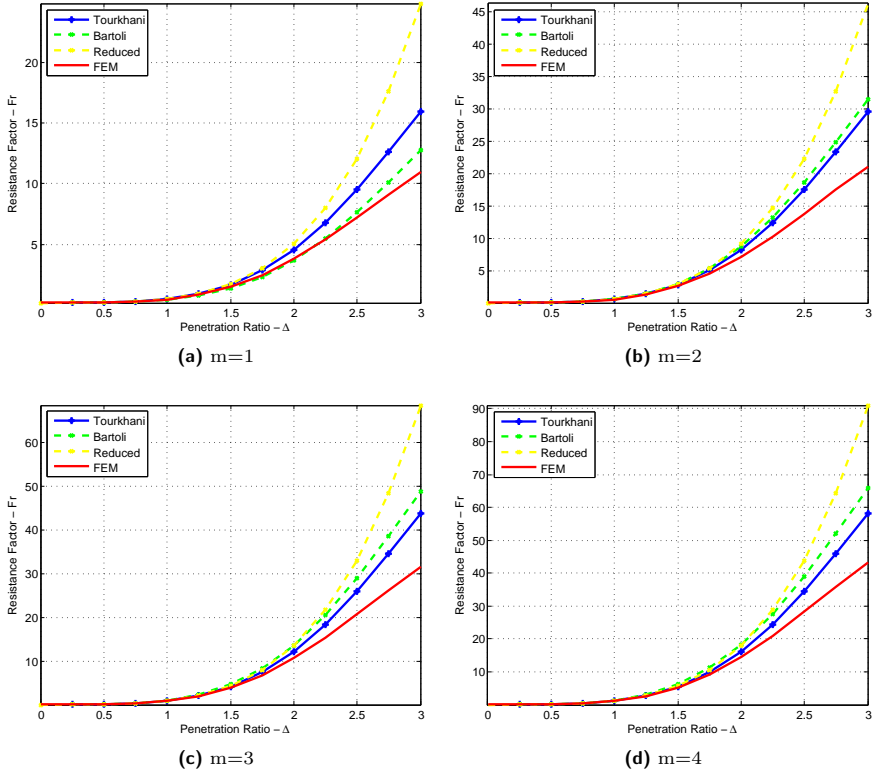


Figure 2.19: Comparison of different expressions for the determination of total Litz wire winding losses for different number of layers. Five Litz bundles per layer $d_b = 0.54$ mm, with 37 strands of $d_s = 0.2$ mm.

In a preliminary comparison test, a huge underestimation of (2.43) was detected, which probably comes from a typing error in [Bartoli et al., 1996], (a n_s factor is missing). A further comparison has been carried (after correcting the detected error) between the methods for different number of layers (see Fig. 2.19).

The geometry of some of the compared examples is illustrated in Fig. 2.20, where the same four layer transformer has been used to determine one layer and

two layer losses for various penetration ratios. In the left-hand column example (see Fig.2.20a, Fig.2.20c and Fig.2.20e), the winding is interleaved, which corresponds to a one layer winding-loss estimation while in the right-hand column (see Fig.2.20b, Fig.2.20d and Fig.2.20f), consecutive layers compose the primary or the secondary of the transformer, alternatively.

Apart from equations (2.43) and (2.46), a reduced expression for low penetration ratios using [Lammeraner and Štafl, 1966] approximations, is introduced (2.47).

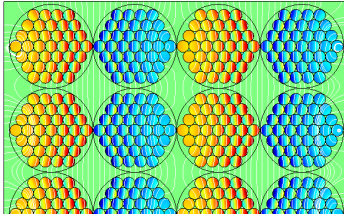
$$P_w = \frac{I^2}{2} R_{dc} \left(1 + \frac{\gamma^4}{192} \left(\frac{1}{6} + \frac{\pi^2 n_s p_f}{4} \left(16 m^2 - 1 + \frac{24}{\pi^2} \right) \right) \right) \quad (2.47)$$

The deviation shown in Fig. 2.19 for large values of Δ derives from the hypothesis that the magnetic field describes a trapezoidal form throughout the whole window width. However, as illustrated in Fig. 2.20 for large values of Δ the magnetic field does not longer describe a trapezoidal form, the incursion of the external field is too pronounced and the one dimensional development of the field equations is no longer appropriate. Moreover, the application of the detailed expressions does not assure a better estimation of losses, and consequently, it can be concluded that the reduced expression is accurate enough and much simpler.

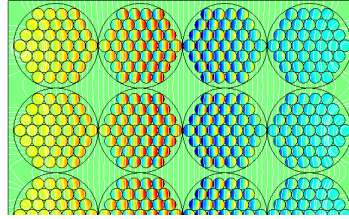
2.2.2.4. Rectangular Litz Wire

In the case of square Litz wires, the analysis made for round wires would be correct and almost accurate because due to the squareness, a circular magnetic field pattern will be described in each of the bundles. However, Litz conductors instead of square they are usually rectangular, due to construction constraints. In that case the magnetic field distribution in a single isolated Litz wire is no longer circular but mostly ellipsoidal (see Fig. 2.21) and the development carried out previously is not completely correct as it introduces estimation errors in the determination of internal proximity effects.

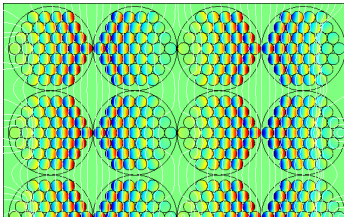
However, rectangular Litz wires are tightly packed round conductors and conduction loss characterization is correctly done with Dowell's expression along with the porosity factor.



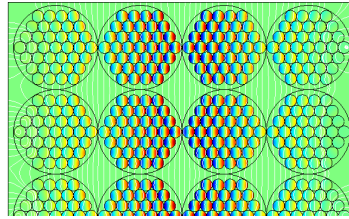
(a) Current density and magnetic field lines, $\Delta = 1.5$.



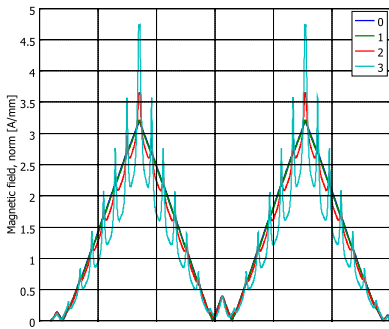
(b) Current density and magnetic field lines, $\Delta = 1.5$.



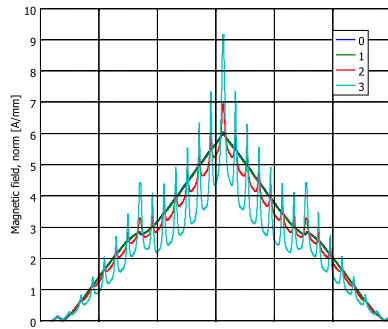
(c) Current density and magnetic field lines, $\Delta = 3$.



(d) Current density and magnetic field lines, $\Delta = 3$.



(e) Magnetic field throughout the boundary line for various Δ .



(f) Magnetic field throughout the boundary line for various Δ .

Figure 2.20: Four layer winding, two primary and two secondary. First column, layers are interleaved, $m=1$. Second column, consecutive layers, $m=2$.

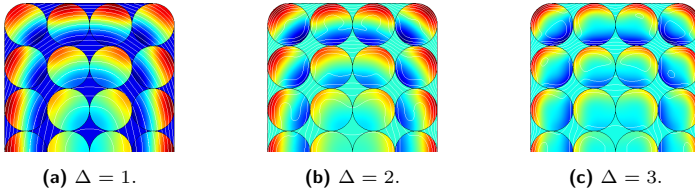


Figure 2.21: Isolated rectangular Litz bundle (half) for various penetration ratios.

2.2.3. Leakage Inductance

The leakage inductance of a transformer represents the field that leaks from the core and returns through the air, not linking both windings and causing imperfect coupling. This effect is modeled by a series leakage inductance in the primary, as well as, in the secondary of the transformer. Due to the leakage field, a certain amount of magnetic energy is stored within the windings, which can be detrimental in some applications due to potential overvoltages. In those cases, the value of the inductance is reduced to its minimum. However, for resonant and non-resonant converters, a known and tuned value of the leakage inductance is necessary for proper operation, much lower in the case of resonant converters.

Although extensive theoretical and empirical research has taken place to establish the variation of winding losses with frequency, there has been much less effort applied to the equivalent theoretical calculation of leakage inductance, especially at higher frequencies where eddy current effects become significant. Only Dowell provides a theoretical approach for the estimation of the combined skin and proximity effects, and the resulting leakage inductance variation with frequency. In general, the focus of the effort to characterize the high-frequency behavior of windings, in particular leakage inductance, has been concentrated on the application of finite element analysis.

2.2.3.1. Foil Windings

As the leakage field does not link both windings, if the secondary winding is short-circuited, the ampere-turns generated by the primary and the secondary

will be equal (almost canceling each other outside the winding area). However, within winding layers and between them the magnetic field will have the same direction and a certain amount of energy will be stored (see Fig. 2.22) which will be represented by the leakage inductance.

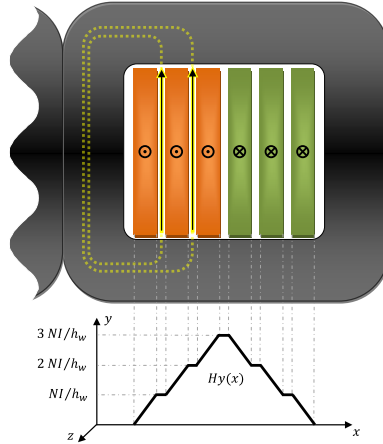


Figure 2.22: Transformer winding with several primary and secondary layers and equivalent dc magnetic field distribution within foil conductors according to Ampere’s circuital law.

The energy stored within the core window is determined from the magnetic field distribution.

$$W_m = \frac{1}{2} \mu \int_V \mathbf{H} \cdot \mathbf{B} \, dv \tag{2.48}$$

The energy in each winding space and interwinding spaces is calculated independently and then combined to provide the complete leakage inductance value, referred to a single winding. Dowell makes the point that by dividing the energy regions into winding and spaces, the winding regions are frequency dependent, due to eddy current and proximity effects, but the interwinding spaces are not. The overall expression for the leakage inductance in the case of Fig. 2.22 is given in (2.49), where L_{w_1} and L_{w_2} are the leakage inductances of the primary and secondary winding layers, respectively, L_g is the leakage inductance due to the in-

terwinding gap and L_{i_1} and L_{i_2} are the leakage inductances due to the interlayer gaps of the primary and secondary, respectively.

$$L_{\sigma} = F_{L_1} L_{w_1} + F_{L_2} L_{w_2} + L_g + L_{i_1} + L_{i_2} \quad (2.49)$$

where F_L represents the inductance factor for each of the windings.

The leakage inductance calculation is carried out, once more, considering complete window height foil conductors, like in the case of foil resistances. Thus, the magnetic field in cartesian coordinates will have only one component.

$$W_m = \frac{1}{4} \mu \int_V |H_y^2(x)| \, dv = \frac{1}{4} \mu \int_{x=0}^{x=d} |H_y^2(x)| h_w l_w \, dx \quad (2.50)$$

where l_w is taken as a constant, the mean value, for the whole transformer windings. Although for more precise expressions, the lengths of each of the winding parts can be taken into account.

In interwinding and interlayer spaces the magnetic field is constant. Considering the winding distribution of Fig. 2.22 there is a unique interwinding space, therefore

$$H_y = m \frac{I}{h_w} \quad (2.51)$$

and the stored energy is

$$W_{m_g} = \frac{1}{4} \mu \int_{x=0}^{x=d_g} \left(m \frac{I}{h_w} \right)^2 h_w l_w \, dx = \frac{1}{4} \mu \frac{l_w d_g}{h_w} m^2 I^2 \quad (2.52)$$

where d_g is the interwinding gap thickness.

In the case of inter-layer gaps, there will be $m - 1$ spaces and the energy stored at all these gaps will be,

$$W_{m_i} = \frac{1}{4} \mu \frac{l_w d_i}{h_w} \frac{(m - 1)}{2m} m^2 I^2 \quad (2.53)$$

where d_i is the inter-layer gap thickness.

For the calculation of the magnetic energy of winding spaces or foil conductors, the frequency-dependent expression of the magnetic field distribution (2.6) will be used (developed in subsection 2.2.2.1).

The magnetic field expression is integrated over the winding thickness and after some mathematical developments, the stored magnetic energy in a winding layer will be

$$W_{m_w} = \frac{1}{4} \mu \frac{l_w h_w \delta}{2} \left[(H_{ext} + H_{int})^2 \varphi_1 - 2 H_{int} H_{ext} \varphi_2 \right] \quad (2.54)$$

where

$$\varphi_1 = \frac{\sinh(2\Delta) - \sin(2\Delta)}{\cosh(2\Delta) - \cos(2\Delta)} \quad \text{and} \quad \varphi_2 = \frac{\sinh(\Delta) - \sin(\Delta)}{\cosh(\Delta) - \cos(\Delta)} \quad (2.55)$$

Replacing the boundary conditions introduced in subsection 2.2.2.1 in the previous expression and summing up the energy of all the m layers of the winding, the total magnetic energy of the winding layers will be

$$W_{m_{ac}} = \frac{1}{4} \mu \frac{l_w \delta}{2 h_w} \frac{1}{3 m} m^2 I^2 \left[(4m^2 - 1) \varphi_1 - 2(m^2 - 1) \varphi_2 \right] \quad (2.56)$$

On the other hand, the dc magnetic energy of m foil layers is

$$W_{m_w} = \frac{1}{4} \mu \int_{x=0}^{x=m d_w} \left| \left(\frac{I}{h_w} \frac{x}{d_w} \right)^2 \right| h_w l_w dx = \frac{1}{4} \mu \frac{l_w d_w}{h_w} \frac{m}{3} m^2 I^2 \quad (2.57)$$

From the ac and dc magnetic energies, the inductance factor expression can be deduced

$$F_L = \frac{1}{2 m^2 \Delta} \left[(4m^2 - 1) \varphi_1 - 2(m^2 - 1) \varphi_2 \right] \quad (2.58)$$

Once the magnetic energy of the whole winding area is defined, the total leakage inductance will be referred to the primary or to the secondary winding. Since $|m_1 I_1| = |m_2 I_2|$ the energy in each winding space referred to the primary will be,

Primary Winding	$W_{m_{w1}}$	$\frac{1}{4} \mu \frac{l_w d_{w1}}{h_w} \frac{m_1}{3} m_1^2 I_1^2 F_{L1}$
Secondary Winding	$W_{m_{w2}}$	$\frac{1}{4} \mu \frac{l_w d_{w2}}{h_w} \frac{m_2}{3} m_1^2 I_1^2 F_{L2}$
Interwinding	W_{m_g}	$\frac{1}{4} \mu \frac{l_w d_g}{h_w} m_1^2 I_1^2$
Primary Interlayer	$W_{m_{i1}}$	$\frac{1}{4} \mu \frac{l_w d_{i1}}{h_w} \frac{(m_1 - 1)}{2 m_1} m_1^2 I_1^2$
Secondary Interlayer	$W_{m_{i2}}$	$\frac{1}{4} \mu \frac{l_w d_{i2}}{h_w} \frac{(m_2 - 1)}{2 m_2} m_1^2 I_1^2$

Table 2.3: Magnetic energies in different winding spaces referred to the primary current.

Equating the total energy with the energy stored by a I_1 current in an inductance

$$W_m = \frac{1}{2} L_\sigma \frac{I_1^2}{2} \quad (2.59)$$

Then the final expression for the total leakage inductance of a winding with consecutive primary and secondary layers will be

$$L_\sigma = \mu m_1^2 \frac{l_w}{h_w} \left[d_{w1} \frac{m_1}{3} F_{L1} + d_{w2} \frac{m_2}{3} F_{L2} + d_g + d_{i1} \frac{(m_1 - 1)}{2 m_1} + d_{i2} \frac{(m_2 - 1)}{2 m_2} \right] \quad (2.60)$$

Reducing Leakage Inductance: Interleaving The main purpose of using foil windings is to reduce the leakage inductance of transformers. The leakage inductance is related with the magnetic field distribution, and to reduce the magnetic field profile, foil layers are usually interleaved (see Fig. 2.23), removing the number of consecutive layers.

This way foil layers will only be subjected to skin effect and the inductance

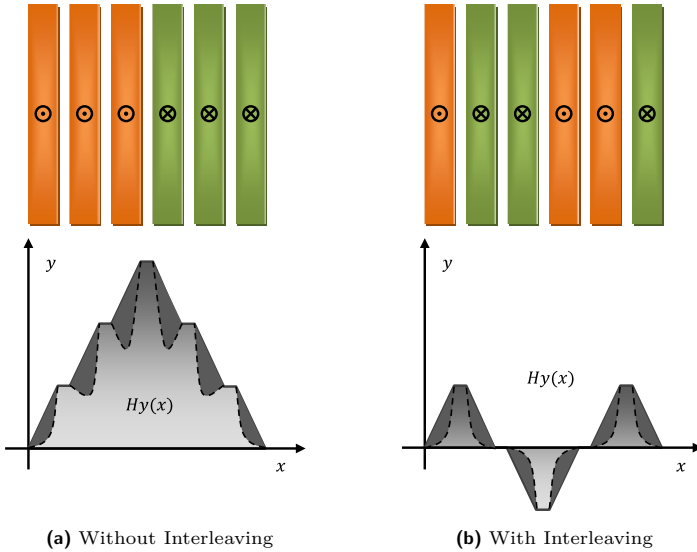


Figure 2.23: Magnetic field distribution in a transformer composed of three layers per winding, dc field (-) and ac field (--)representation.

factor expression will be reduced to

$$F_L = \frac{3}{2\Delta} \varphi_1 \quad (2.61)$$

As there are no consecutive layers the leakage inductance due to this phenomena will be zero, $L_{i_1} = L_{i_2} = 0$. Besides being affected only by skin effect, the reduction of the external magnetic field for each foil (to m number of section interfaces) and also of the external magnetic field around each foil conductor (by m too) reduces the total magnetic energy by a factor of m^2 . Nevertheless, as there are m interwinding gaps, the final leakage inductance expression for interleaved windings will be,

$$L_{\sigma_i} = \mu \frac{l_w}{h_w} m \left[d_{w_1} \frac{1}{3} F_{L_1} + d_{w_2} \frac{1}{3} F_{L_2} + d_g \right] \quad (2.62)$$

A comparison example is illustrated in Fig. 2.24, where a transformer with 3

primary and secondary copper layers is considered with and without interleaving. The interleaved leakage inductance is $\sim 3^5$ times smaller. Besides a reduced dc leakage inductance, the frequency effects due to proximity between consecutive layers are reduced, and the leakage inductance at higher frequencies decreases much slower.

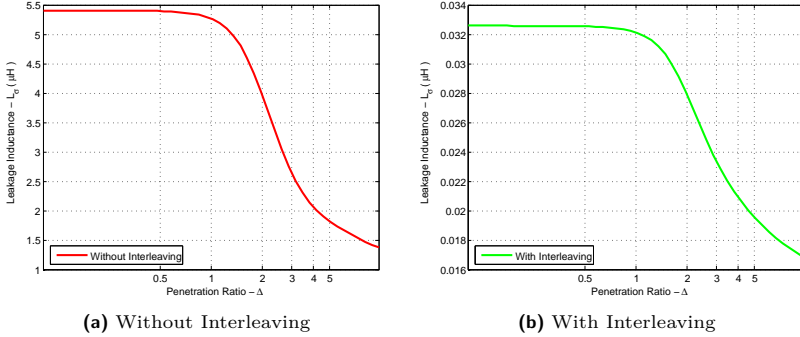


Figure 2.24: Leakage inductance ($\mu\text{H}/\text{m}$) in a transformer with 3 primary and secondary copper layers, with $d_{w1} = d_{w2} = 2$ mm, $d_g = d_{i1} = d_{i2} = 1$ mm and $h_w = 20$ mm.

Increasing Leakage Inductance When a minimum leakage inductance is required the number of winding turns is increased and no interleaving is applied. If the primary and secondary of the transformer are composed of N_1 and N_2 turns respectively, the final expression for the leakage inductance will increase by a factor of N_1^2 referred to the primary winding, reaching the final expression

$$L_\sigma = \mu N_1^2 \frac{l_w}{h_w} \left[d_{w1} \frac{m_1}{3} F_{L1} + d_{w2} \frac{m_2}{3} F_{L2} + d_g + d_{i1} \frac{(m_1 - 1)}{2m_1} + d_{i2} \frac{(m_2 - 1)}{2m_2} \right] \quad (2.63)$$

Once more using the porosity factor defined by Dowell as a correction factor, the leakage inductance factor is modified to account for round, rectangular or short foil conductors.

$$F_L' = \frac{1}{2m^2 \Delta'} \left[(4m^2 - 1) \varphi_1' - 2(m^2 - 1) \varphi_2' \right] \quad (2.64)$$

with $\Delta' = \sqrt{\eta_w} \Delta$ and

$$\varphi'_1 = \frac{\sinh(2\Delta') - \sin(2\Delta')}{\cosh(2\Delta') - \cos(2\Delta')} \quad \text{and} \quad \varphi'_2 = \frac{\sinh(\Delta') - \sin(\Delta')}{\cosh(\Delta') - \cos(\Delta')} \quad (2.65)$$

Once more, rectangular Litz bundles are supposed to be tightly packed round conductors, and Dowell's inductance expression value is directly applicable. Contrary to winding losses, round Litz bundles will be correctly characterized with this expression, because the magnetic field, as long as the penetration ratio is kept controlled, describes a trapezoidal form in the winding area.

2.3. Magnetic Core, Magnetic Losses

In 1892, even before microscopic magnetization process was defined, Charles Proteus Steinmetz [Steinmetz, 1892] introduced an expression for the characterization of magnetic loss density (2.66). From the analysis of various loss curves, Steinmetz ended up with this expression.

$$P_s = \eta B_m^b \quad (2.66)$$

where η and b are determined by the material characteristic, and B_m is the peak induction value in a bidirectional magnetization case.

Nowadays, a more general expression is widely used in the design of magnetic power devices (2.67); like transformers, electric machines or inductors.

$$P_s = K f^a B_m^b \quad (2.67)$$

where K and a are determined by the material characteristic, and f is the frequency of the sinusoidal waveform.

As well as the Steinmetz equation, a usual proceeding to analyze core loss in more detail is to break it up into three separate terms: static hysteresis loss P_h , classic eddy current loss P_e , and excess eddy current or anomalous loss P_a . Therefore, it is assumed that three different physical effects are contributing to

magnetization losses. It should be noted that this procedure is mainly applied in the characterization of electric machines.

$$P_s = P_h + P_e + P_a \quad (2.68)$$

Another usual procedure to get magnetization losses is the determination of the hysteresis model. The static hysteresis model is usually used in combination with the loss separation approach, while more complex models have been proposed lately which consider the dynamic behavior of the magnetic material. Most of the hysteresis models can be sorted out in two model categories, the Jiles-Atherton model [Jiles and Atherton, 1984] and the Preisach model [Preisach, 1935], although also other simplified models can be found in the literature.

However, in order to understand the variety of characterization methodologies a short description of the hysteresis will be introduced.

2.3.1. Magnetic Hysteresis

The phenomenon exhibited by a system, often a ferromagnetic material, in which the reaction of the system to changes is dependent upon its past reactions to change.

Magnetization process can be divided into several steps. In the demagnetized state, all domains cancel each other resulting in a zero magnetic field. When an external magnetic field is applied, the magnetic domains change from an initial reversible magnetization state, to an irreversible one. In this state, the domain walls are first displaced and then rotated in another reversible state, and finally a saturation state is reached where all domains are aligned.

Depending on the magnetization processes and the history of the material, the magnetic characteristic describes different curves, i.e. different types of hysteresis behaviors, some of them are illustrated in Fig. 2.25.

The major loop is the magnetization curve when the applied field is high enough to force the material into saturation, closing the loop at the tips. Every loop inside the major loop is defined as a minor loop, these loops can be asymmetric or symmetric with respect to the origin. In the case of transformer cores, the

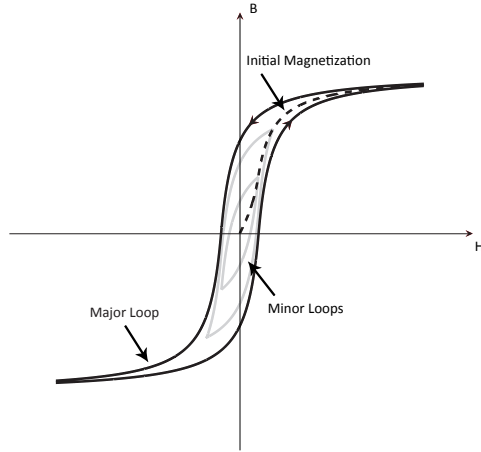


Figure 2.25: Types of hysteresis loops and magnetization curves.

magnetization is always symmetric like the minor loops illustrated in Fig. 2.25. The initial magnetization curve is the transition of the magnetization induction from the initial condition of zero flux to the tip of the major loop.

2.3.2. Hysteresis Models

As presented before, there are two main hysteresis models currently applied in circuit simulation or finite element analysis, the Jiles-Atherton [Jiles and Atherton, 1984] model and the Preisach [Preisach, 1935] model. In addition, the simplicity of the Chan-Vladirimescu [Chan et al., 1991] model, makes it an attractive solution to be used with core materials where the steady-state magnetization processes are symmetrical and the hysteresis loop is longitudinal. The main characteristics of the three methods are briefly introduced in the following section.

2.3.2.1. Jiles-Atherton Model

The model of Jiles and Atherton [Jiles and Atherton, 1984] was developed between 1983-1986 and separates the hysteresis loop on the reversible magnetization

M_{rev} , or anhysteretic curve, and the irreversible one M_{irr} , or the equivalent loss energy.

$$M = M_{rev} + M_{irr} \quad (2.69)$$

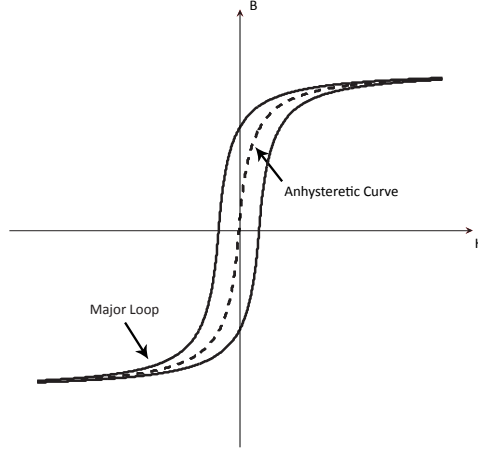


Figure 2.26: Anhysteretic curve and mayor loop.

The anhysteretic curve, illustrated in Fig. 2.26, is characterized by a modified Langevin function (2.70).

$$M_{an} = M_s \left[\coth \left(\frac{H_e}{A} \right) - \frac{A}{H_e} \right] \quad (2.70)$$

where A modifies the curvature of the function and H_e is the effective applied field, with $H_e = H + \alpha M$ and α representing the iteration between domains.

The expression of the irreversible magnetization is obtained from a lumped model of the losses determined from the domain wall displacement (2.71).

$$\frac{M_{irr}}{dH} = \frac{M_{an} - M}{\frac{\delta k}{\mu} - \alpha (M_{an} - M)} \quad (2.71)$$

where k represents the energy dissipation and δ is the direction of the applied field (+1 for positive and -1 for negative slope).

And finally the total magnetization rate is obtained from the relative ratio, given by c , between the reversible and the irreversible magnetizations.

$$\frac{dM}{dH} = \frac{1}{1+c} \frac{M_{an} - M}{\frac{\delta k}{\mu} - \alpha(M_{an} - M)} + \frac{c}{1+c} \frac{dM_{an}}{dH} \quad (2.72)$$

One of the difficulties with the Jiles-Atherton model is the extraction of model parameters, already pointed out in [Jiles et al., 1992]. The algorithm requires nine experimentally measured parameters. (1) The coercivity H_c , (2) the remanence B_r , (3) the initial susceptibility χ'_{in} ², (4) the initial anhysteretic susceptibility χ'_{an} , (5) the differential susceptibility at the coercive point χ'_{H_c} , (6) the differential susceptibility at remanence χ'_{B_r} and (7)(8) the maximum magnetization points (H_{max} , M_{max}) on the loop tip, as well as (9) the differential susceptibility of the initial magnetization curve at the same point, χ'_{max} . The algorithm yields to the five previously mentioned model parameters, M_s , a , k , α , and c . The model parameters are extracted from the initial magnetization curve, the mayor loop and the anhysteretic curve, which can be determined from the mayor hysteresis loop.

2.3.2.2. Preisach Model

The model of Ferenc Preisach [Preisach, 1935] has survived to more than 60 years of scientific analysis and competition with other models that have been forgotten. The original Preisach model, or the classical Preisach model, was forgotten until the Russian mathematician Krasnoselskii came across the model and understood the general mathematical idea [Mayergoyz, 1986], introducing the algebraic theory of the model. From the work carried out by Krasnoselskii, Issak D. Mayergoyz introduced and analyzed the properties of the model, as well as, the required experimental data for its characterization.

One of the greater controversies around the Preisach model is its phenomenological character. Even if the model does not have any relationship with the phys-

²Susceptibility, relationship between magnetization M and magnetic field H , $\chi = M/H$.

ical processes occurring in the magnetization process of magnetic materials, it reproduces the hysteresis curve and the field history with a great reliability. Nevertheless, it does not explain what happens in the material. The Preisach method uses a finite number of bistable units which consider the previous state of the material as well as its future evolution (see Fig. 2.27a). The combination of these finite

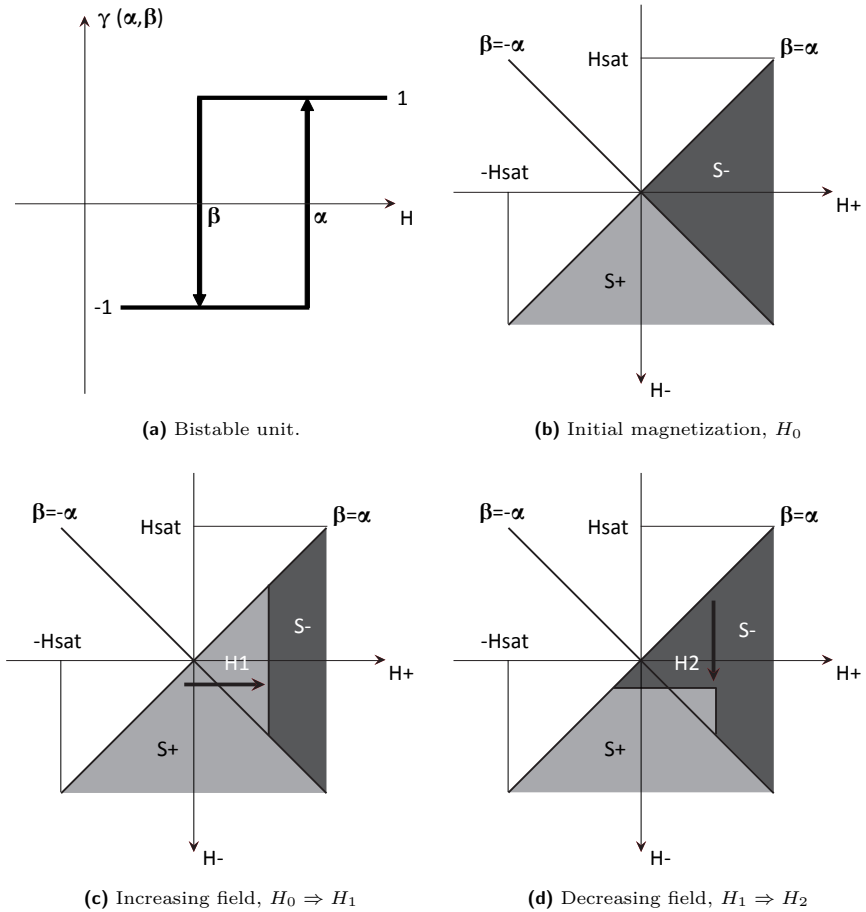


Figure 2.27: Preisach bistable unit and Preisach plane, or triangle.

number of bistable units $\gamma(\alpha, \beta)$, describes the evolution of the magnetic material. If H_{sat} represents the saturation magnetic field and B_{sat} the corresponding saturation induction of the material, when the applied field is $H > H_{sat}$, all bistable units are positive and the induction is $B = B_{sat}$. However, if the applied field is $H < -H_{sat}$, all bistable units are negative and the induction is $B = -B_{sat}$. Therefore, these bistable units must satisfy $\alpha < H_{sat}$ and $\beta > -H_{sat}$, and as the hysteresis phenomena is dissipative, then $\alpha > \beta$. These three conditions define the Preisach plane illustrated in Fig. 2.27.

In the initial magnetization state, zero magnetization, the number of positive and negative bistable units must be the same ($S_+ = S_-$), which is easily represented on the Preisach plane by distributing equally the bistable units within the triangle using the $\beta = -\alpha$ symmetry line (see Fig. 2.27b).

When the applied field is increased $H+$, the corresponding α axis bistable units are switched to their positive state (see Fig. 2.27c, $S_+ > S_-$). On the contrary, if the field is reduced $H-$, the corresponding β axis bistable units are switched to their negative state (see Fig. 2.27d, $S_+ < S_-$). The calculation of the net magnetization is the integration of the positive and negative bistable units.

A specific magnetic material is characterized with a distribution function $\mu(\alpha, \beta)$, known as Preisach function or weighting function, that describes the weighting values of each bistable unit in the Preisach plane. The main difficulty with the Preisach model lies on the determination of this density function. The Preisach distribution function γ can be implemented using an Everett integral [Mayergoyz, 1986], which requires several experimental first order reversal curves for its correct characterization. Another way of getting the density function lies on the supposition that the distribution function describes a specific pattern, like a Lorentzian [Bertotti, 1992] or Gaussian function [della Torre and Vajda, 1994]. The simplest of the procedures to determine the distribution function is described in [Hui and Zhu, 1995] where only the mayor loop is required.

2.3.2.3. Chan-Vladirimescu Model

The Chan-Vladirimescu model [Chan et al., 1991] employs only manufacturer-supplied data like the coercivity H_c , the maximum magnetic induction B_s and

its corresponding magnetic field H_s as well as the remanence B_r . The magnetic characteristic is described with two hyperbolic curves. The upper branch of the loop, or the downward part of the loop ($H_s \Rightarrow -H_s$), is given by:

$$B_+(H) = B_s \frac{H + H_c}{|H - H_c| + H_c \left(\frac{B_s}{B_r} - 1 \right)} \quad (2.73)$$

The lower branch of the loop, or the upward part of the loop ($-H_s \Rightarrow H_s$), is given by:

$$B_-(H) = B_s \frac{H - H_c}{|H - H_c| + H_c \left(\frac{B_s}{B_r} - 1 \right)} \quad (2.74)$$

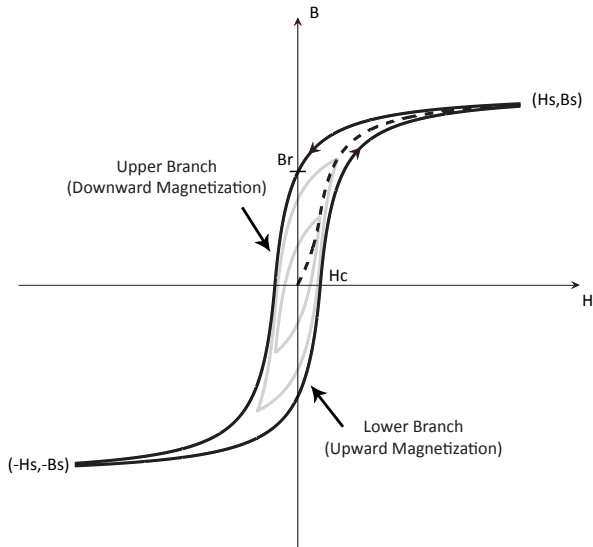


Figure 2.28: Chan-Vladirimescu model with initial magnetization curve, mayor loop and minor symmetrical loops.

The initial magnetization curve is deduced from the average value of the upper

and lower branches (2.75).

$$B_{mag}(H) = \frac{B_+(H) + B_-(H)}{2} \quad (2.75)$$

In order to characterize the minor loops of the material, the upper branch is reduced by a B_d magnetization induction value, while the lower branch is increased by the same value.

$$\text{Upper Branch} \quad B(H) = B_+(H) - B_d \quad (2.76)$$

$$\text{Lower Branch} \quad B(H) = B_-(H) + B_d$$

The intersection of the upper and lower branches of the minor loop will lie on the magnetization curve $B_{mag} = H$. These intersection points are just the extreme points of the minor loop, and the difference between the upper or lower major branches and the magnetization curve in those extreme points will determine the B_d magnetization induction value.

2.3.3. Loss Separation Approach

Traditionally core loss has been divided up into two terms: hysteresis loss P_h and eddy current loss P_e (2.77).

$$P_v = P_h + P_e \quad (2.77)$$

where

$$P_h = k_h f B_m^b \quad \text{and} \quad P_e = k_e f^2 B_m^2 \quad (2.78)$$

However, the traditional two term method assumed that magnetization process was perfectly homogeneous in space, which was latter on proven to be incorrect. Although there were already some theories about the anomalous behavior of magnetic materials, Bertotti [Bertotti, 1986] introduced a physical explanation of

this excess phenomena and a generally approved expression (2.79). According to Bertotti , the excess in dynamic loss is a consequence of domain wall motion.

$$P_s = P_h + P_e + P_a \quad (2.79)$$

with

$$P_a = k_a B_m^{1.5} f^{1.5} \quad (2.80)$$

P_a is referred as the excess or anomalous loss and k_a is related to the material cross-sectional area A , conductivity σ and a parameter which describes the material microstructure η_o , as well as a numerical constant G .

$$k_a = 8 \sqrt{\sigma G A \eta_o} \quad (2.81)$$

Excess eddy current loss calculation is not straightforward. Manufacturers do not supply information about the microstructure of the material, so curve fitting is necessary to get the parameter k_a related to excess loss.

Classical eddy current loss expression P_e derives from Maxwell equations. The time average eddy current loss, per unit volume, is determined getting a widely used expression (2.82).

$$P_e = \frac{\pi^2 d^2}{6 \rho} f^2 B_m^2 \quad (2.82)$$

From the average eddy current loss expression the constant k_e related with the loss separation approached is established.

$$k_e = \frac{\pi^2 d^2}{6 \rho} \quad (2.83)$$

Usually for the characterization of hysteresis loss the primitive expression of the Steinmetz equation, without frequency parameter α , is used (2.84).

$$P_h = K f B_m^b \quad (2.84)$$

If the parameters b and K of the primitive Steinmetz equation are not provided by the manufacturer a curve fitting is necessary. As well as the Steinmetz primitive equation, the primitive hysteresis models (static models) are used in some cases.

2.3.3.1. Time Domain, General Expression

The expressions introduced up to now are only valid for sinusoidal excitation cases, therefore, so as to get magnetic losses for a more general case, a time domain expression has been developed [Lin et al., 2004; Roshen, 2007]. This new general expression has to be consistent with the sinusoidal expression in the frequency domain.

On the one hand, in the case of excess loss, an expression that will fit correctly with the sinusoidal expression is (2.85).

$$p_a(t) = k_2 \left(\frac{dB(t)}{dt} \right)^{1.5} \quad (2.85)$$

The time average value of a sinusoidal flux density for this new expression is equated to the sinusoidal frequency domain expression (2.86).

$$P_a = k_2 \frac{1}{T} \int_0^T \left(\frac{dB(t)}{dt} \right)^{1.5} dt = k_a B_m^{1.5} f^{1.5} \quad (2.86)$$

From where the new constant parameters will be defined,

$$k_2 = \frac{k_e}{\sqrt{2\pi} \int_0^{2\pi} \cos(\theta)^{1.5} d\theta} \quad (2.87)$$

On the other hand, in the case of classical eddy current loss, a similar procedure is applied to get the time domain expression.

$$P_e = k_1 \frac{1}{T} \int_0^T \left(\frac{dB(t)}{dt} \right)^2 dt = k_a B_m^2 f^2 \quad (2.88)$$

From where,

$$k_1 = \frac{k_e}{2\pi^2} \quad (2.89)$$

Regarding hysteresis loss, the equivalent elliptical loop introduced by Lin [Lin et al., 2004] is used. Magnetic loss density is defined as,

$$P_h = \frac{1}{T} \int_0^T H(t) \frac{dB(t)}{dt} dt \quad (2.90)$$

The hysteresis loop can be decomposed in two components; a reversible component, and an irreversible component related to the hysteresis loss. Consequently, the instantaneous hysteresis loss will be,

$$p_h(t) = H_{irr}(t) \frac{dB(t)}{dt} \quad (2.91)$$

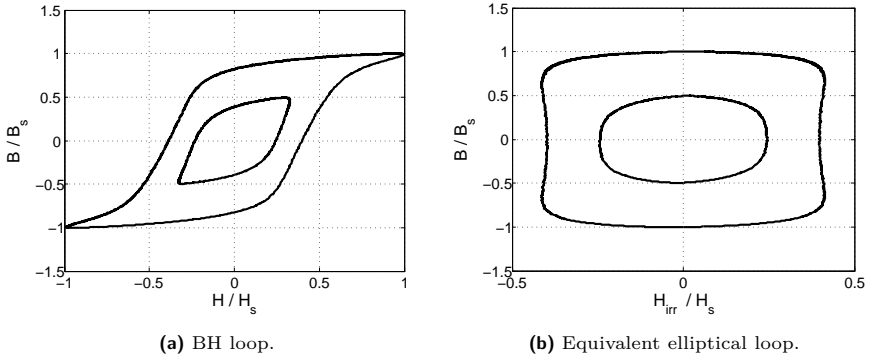


Figure 2.29: Magnetic characteristic and equivalent elliptical loop.

The irreversible component of the magnetic loop describes an ellipse (see Fig. 2.29) that can be defined as,

$$B = B_m \sin(\theta) \quad \text{and} \quad H_{irr} = H_m \cos(\theta) \quad (2.92)$$

Equating the surface of the elliptical loop for a sinusoidal excitation case,

$$P_h = H_m B_m 2\pi f \frac{1}{T} \int_0^T \cos^2(2\pi f t) dt = H_m B_m \pi f \quad (2.93)$$

with the time-average hysteresis loss for sinusoidal excitation $k_h f B_m^b$, the representation for H_m is obtained, and consequently H_{irr} .

$$H_{irr} = \pm \frac{1}{C_b} k_h |B_m \cos(\theta)|^{b-1} \quad (2.94)$$

Finally, the instantaneous hysteresis loss expression will be,

$$p_h(t) = \pm \frac{1}{C_b} k_h |B_m \cos(\theta)|^{b-1} \left(\frac{dB(t)}{dt} \right) \quad (2.95)$$

where,

$$C_b = 4 \int_0^{\pi/2} \cos^b(\theta) d\theta \quad (2.96)$$

Taking into account the developments carried out for each of the loss terms, the time domain general expression for the loss separation approach is reached,

$$P_s = k_0 \frac{1}{T} \int_0^T |B_m \cos(\theta)|^{\beta-1} \left(\frac{dB(t)}{dt} \right) dt + \quad (2.97)$$

$$k_1 \frac{1}{T} \int_0^T \left(\frac{dB(t)}{dt} \right)^2 dt + k_2 \frac{1}{T} \int_0^T \left(\frac{dB(t)}{dt} \right)^{1.5} dt$$

where,

$$k_0 = \pm \frac{k_h}{4 \int_0^{\pi/2} \cos^b(\theta) d\theta} \quad (2.98)$$

$$k_1 = \frac{k_e}{2\pi^2} \quad \text{and} \quad k_2 = \frac{k_a}{\sqrt{2\pi} \int_0^{2\pi} \cos(\theta)^{1.5} d\theta}$$

This three part expression is usually used in the characterization of electric machines, where the magnetic parts are made of rolled steel and the determination of classical eddy current effects are straightforward.

2.3.4. Empirical Methods, Steinmetz Equation

Another major group of core-loss calculation methods is based on empirical measurement observations. One of the advantages of these methods is that they are easy to use, especially to designers who do not have much expertise on magnetism. Lacking of physical bases, empirical methods are usually applicable to particular

material and operating conditions. Loss in the magnetic material is often predicted using a power law equation:

$$P_s = K f^a B_m^b \quad (2.99)$$

where B_m is the peak flux density value of the ac waveform (if the flux density waveform has no time average). K , a and b are determined by the material characteristic and usually obtained from the manufacturer's datasheet. For different magnetic materials, different values are used. The Steinmetz equation is basically a curve fitting of measured core-loss density under sinusoidal magnetization waveform. Therefore, it can be extracted from the manufacturers data, and without knowing the detailed material characteristics.

The empirical Steinmetz equation (2.99) has proven to be the most useful tool for the calculation of magnetization losses. It requires only three parameters, which are usually provided by the manufacturer. For sinusoidal flux waveform it provides a high accuracy and is quite simple to use. However, the original Steinmetz equation (OSE) and the corresponding set of parameters fail to represent correctly losses for non-sinusoidal waveforms. There is no direct and clear way to extend the Steinmetz equation to arbitrary operating waveforms, like in the case of the loss separation approach.

Intuitively, it has been tried to apply a Fourier transform to any arbitrary waveform to obtain a series of sine waves, applying the Steinmetz equation to each frequency component. However, the summation of calculated losses of each frequency is not the total core loss, because there is no orthogonality between different orders of harmonics. Furthermore, it is not universally appropriate to apply the Fourier transform to a magnetic component [Reinert et al., 2001], which is non-linear inherently.

Lately, derivations of the Steinmetz equation have been published to deal with non-sinusoidal waveforms, where general time dependent compact expressions have been developed. The Modified Steinmetz Equation (MSE), the Improved Generalized Steinmetz Equation (IGSE) or the Natural Steinmetz Extension (NSE), the Waveform-coefficient Steinmetz Equation (WcSE) and the Equivalent Elliptical Loop (EEL) have been proposed to extend the original Steinmetz equation to

non-sinusoidal applications, using only the Steinmetz parameters provided by the manufacturer.

2.3.4.1. Modified Steinmetz Equation (MSE)

According to [Reinert et al., 2001], the macroscopic magnetization rate dM/dt is directly related to the core losses. The task is then to replace the frequency from the Steinmetz equation with the physical loss parameter dM/dt which is proportional to the rate of change of magnetic induction, dB/dt . This method introduces an equivalent frequency which is related to the magnetization rate.

Based on physical understanding that loss depends on dB/dt , [Reinert et al., 2001] averages dB/dt over a flux excursion to get:

$$\left\langle \frac{dB(t)}{dt} \right\rangle = \frac{1}{\Delta B} \int_0^T \left(\frac{dB(t)}{dt} \right)^2 dt \quad (2.100)$$

Where ΔB is the peak-to-peak flux amplitude and T is the period of the flux waveform. From the averaged magnetization rate an equivalent frequency f_{eq} can be calculated using the normalization constant $2/\Delta B \pi^2$:

$$f_{eq} = \frac{2}{\Delta B^2 \pi^2} \int_0^T \left(\frac{dB(t)}{dt} \right)^2 dt \quad (2.101)$$

Developing the theory, and supposing that the magnetization is repeated with a period of $T_r = 1/f_r$, [Reinert et al., 2001] states that the power losses can be described with:

$$P_s = (K f_{eq}^{a-1} B_m^b) f_r \quad (2.102)$$

2.3.4.2. Improved Generalized Steinmetz Equation (IGSE)

The improved generalized Steinmetz equation (IGSE) [Venkatachalam et al., 2002] and the natural Steinmetz extension (NSE) [van den Bossche et al., 2004], although they have different names (because they are from different authors), they use the same expression to characterize core losses in case of a non-sinusoidal

excitation. They both stem from the generalized Steinmetz equation (GSE) [Li et al., 2001].

The generalized Steinmetz equation is developed from a general hypothesis for instantaneous core loss, which assumes that magnetic loss depends on the rate of change of the magnetic flux density and its instantaneous value [Lancarotte, 2001].

$$p_s(t) = p_d \left(\frac{dB(t)}{dt}, B(t) \right) \quad (2.103)$$

The work carried out in this publication analyzes the behavior of FeSi steel sheets under different magnetization rates ($dB(t)/dt$) and induction levels ($B(t)$). According to [Lancarotte, 2001], finding an expression depending on this two variables would lead to the definition of magnetic losses for all type of waveforms. A careful analysis of the work introduced in this article has to be done, because the term "average dissipated power" can lead to erroneous conclusions. According to the author, those waveforms which have the same magnetization rates and induction levels, will describe the same characteristic curve and will have the same average dissipated power.

This fact can be verified in Fig. 2.30d. The core of a FeSi transformer has been excited with three different waveforms (see Fig. 2.30a), each of them with the same maximum voltage, which will consequently lead to the same rate of change of the magnetic flux density (see Fig. 2.30c). Moreover, the voltages have been applied with different frequencies and different duty cycles to reach the same maximum flux density.

Due to the zero voltage period on the 50Hz wave and the 100Hz wave (see Fig. 2.30a), the BH loop presents a slight difference in comparison to the 200Hz wave (see Fig. 2.30d). During the zero voltage period, some of the energy is lost and consequently the area of the loop gets a bit wider.

As mentioned before, the term dissipated power can be misunderstood. The conclusion to this test is that the energy (the area of the loop), is the same. However, the power will increase linearly because this loop has to be multiply with the waveform frequency.

Based on this fact the proposed generalized Steinmetz equation (GSE) will

look like (2.104),

$$P_s = \frac{1}{T} \int_0^T k_1 \left| \frac{dB(t)}{dt} \right|^a |B(t)|^{b-a} dt \quad (2.104)$$

However, according to [Venkatachalam et al., 2002], the dependence of the instantaneous loss on the instantaneous parameters only, is a potential problem, which is solved by the same authors in the proposed Improved Generalized Steinmetz Equation (IGSE). The Natural Steinmetz Extension (NSE) [van den Bossche

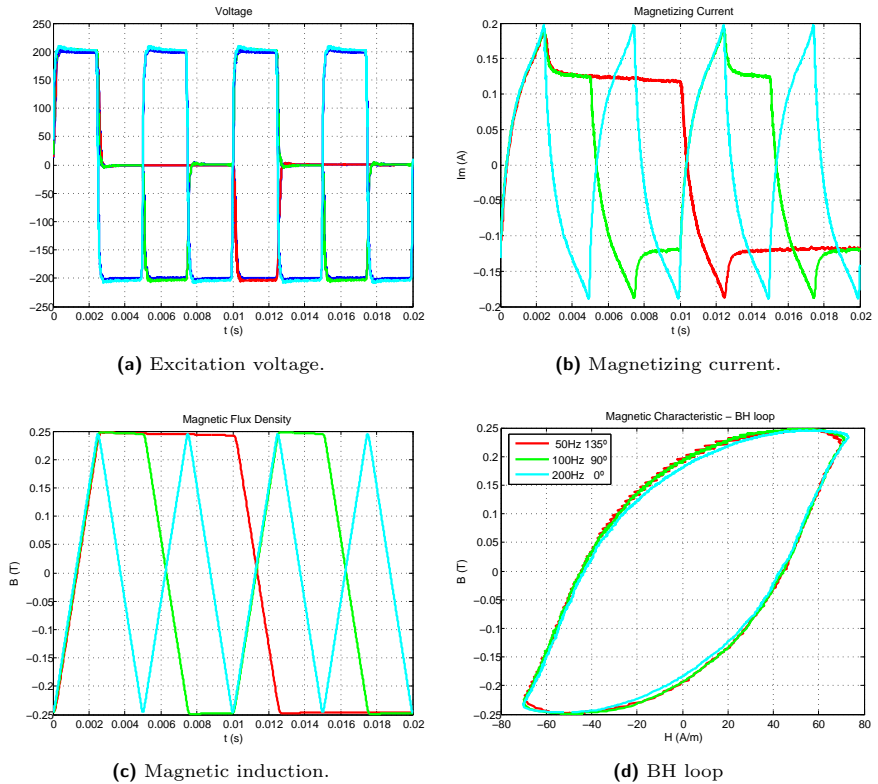


Figure 2.30: Measurements carried out in a FeSi transformer in order to verify the magnetic induction slope dependency.

et al., 2004] is introduced some time later, and although it looks a bit different in a first sight, actually it uses the same expression (2.105).

$$P_s = \frac{1}{T} \int_0^T k_i \left| \frac{dB(t)}{dt} \right|^a (\Delta B)^{b-a} dt \quad (2.105)$$

where,

$$k_i = \frac{K}{(2\pi)^{a-1} \int_0^{2\pi} |\cos(\theta)|^a 2^{b-a} d\theta} \quad (2.106)$$

Which is determined equating the loss expression for a sinusoidal excitation case with the Steinmetz equation.

$$P_s = \frac{1}{2\pi} k_i (2\pi f)^a B_m^b \int_0^{2\pi} |\cos(\theta)|^a 2^{b-a} d\theta = K f^a B_m^b \quad (2.107)$$

2.3.4.3. Equivalent Elliptical Loop (EEL)

Apart from the expression proposed for the time dependent hysteresis loss introduced in the previous section, [Lin et al., 2004] proposes a modified Steinmetz equation based on the same development. The only difference lies in the frequency exponent of the Steinmetz equation that is introduced in this case:

$$p_s(t) = |C| \left| \frac{dB(t)}{dt} \right|^a \quad (2.108)$$

where

$$C = \pm \frac{1}{C_{ab}} K \left| B_m \cos(\theta) \right|^{b-a} \quad (2.109)$$

and

$$C_{ab} = \frac{2}{\pi} (2\pi)^a \int_0^{\pi/2} \cos^b(\theta) d\theta . \quad (2.110)$$

2.3.4.4. Waveform coefficient Steinmetz Equation (WcSE)

In [Shen, 2006] another concept is used to modify the Steinmetz equation, the waveform coefficient concept which correlates the Steinmetz equation with non-sinusoidal waveforms. This approach attempts to correlate the non-sinusoidal waveforms to the sinusoidal one with the same peak flux density, through calculating the "area" of the flux waveform. First of all, for the sinusoidal flux waveform, the integral of the half cycle is derived.

$$W_{sin} = \frac{1}{T B_m} \int_0^{T/2} B_m \sin(\omega t) dt = \frac{2}{\pi} \quad (2.111)$$

Similarly, for example in the case of a rectangular voltage waveform and thereby a triangular flux waveform, the "area" of the triangular waveform is found for the same maximum flux density,

$$W_{sq} = \frac{4}{T B_m} \int_0^{T/4} \left(\frac{4 B_m}{T} t \right) dt = \frac{1}{2} \quad (2.112)$$

From which the flux waveform coefficient, FWC, of the square voltage waveform (triangular flux waveform) can be defined as:

$$FWC_{sq} = \frac{W_{sq}}{W_{sin}} = \frac{\pi}{4} \quad (2.113)$$

So, according to [Shen, 2006], the core loss can be obtained from:

$$P_s = FWC_{sq} K f^a B_m^b \quad (2.114)$$

2.3.5. Methodology Comparison

As it has been shown, currently several different approaches are applied to determine magnetic losses. Generally, the hysteresis models are used when there is an unknown flux pattern in the material. The hysteresis model describes the behavior of a specific material and therefore measurement data are required for each of the materials.

In the case of the Jiles-Atherton model, the precision lies on the effort made in the measurement process: once the measurements are done the model only requires the evaluation of three equations. In contrast, with the Preisach model, the precision of the distribution function depends on the selected measurement evaluation method. Besides the high number of measurements, the method will be as time consuming as the precision of the distribution function. Although the Jiles-Atherton method presents higher estimation errors, the simplicity of the evaluation algorithm makes it the best candidate for circuit or finite element simulations.

Between the loss separation approach and the empirical methods based on the Steinmetz equation the choice is clear. Both methodologies are based on the same sinusoidal dependent loss curves provided by the manufacturer, or measured in a sinusoidal basis. The applied parameters belong in each case to a specific frequency range, however in the case of the loss separation approach, there is an initial curve fitting aimed at getting the three parameters. Then, the three parameters are evaluated for non-sinusoidal waveforms, and after that three loss expressions are derived and summed up at the end. In the Steinmetz based equations, the initial curve fitting is avoided (unless manufacturer data is missing), only one parameter is evaluated for non-sinusoidal waveforms and the loss evaluations needs only one development stage.

Although it is almost impossible to represent the complex relationship among loss, magnetic induction, and frequency by such an explicit exponential function, the high accuracy provided, at least for sinusoidal waveforms, by the empirical Steinmetz equation makes it an ideal choice for our case study: a non-sinusoidally fed medium-frequency power transformer. Moreover, the operational frequency of the transformer does not vary as much as the Steinmetz equation parameters may, and the saturation zone will be avoided.

2.4. Thermal Behavior and Temperature Rise

The losses generated in the core and the winding of a transformer give rise to heating. The heat is transferred to the surface and then further to the ambient by radiation and convection. An equilibrium temperature is reached when the heat generated by the losses balances the heat transferred away. The volume

reduction for higher power density transformers also reduces the cooling surface and consequently the equilibrium temperature rises. Therefore, in high-power density transformers the temperature rise is most often a restricting variable. Too high temperatures may deteriorate, or even destroy, the isolation of a transformer winding.

When the heat dissipation requirements are very high the transformer is usually immersed in oil or silicone. Due to the thermal characteristics of these fluids (see Appendix B.1) the equivalent conductance between the transformer and the fluid increases (compared to air), reducing the temperature gradient and therefore the overall temperature of the transformer.

2.4.1. Simplified Thermal Model: Equivalent Nodal Network

The term simplified refers to two aspects:

- A simple thermo-physical model of the object is simulated (e.g. only one heat transfer mode considered).
- A reduced number of equations that can correctly describe the object is simulated (e.g. reduced number of state variables).

An equivalent nodal network is a simplified thermal model, which uses the well-known analogy between electrical circuits and thermal models. The network, or circuit, is composed of nodes representing different zones where the temperature is more or less homogeneous. The connection between these nodes is made by equivalent thermal resistances, and the heat sources are connected in the corresponding nodes. The heat capacity of each node represents the thermal inertia of the respective zone (see Fig. 2.31).

In an equivalent nodal network, the temperatures of nodes 1 to m must be evaluated while the ones from nodes $m + 1$ to n are considered to be fixed (e.g. the outside air temperature or ambient temperature).

For each of the control nodes, j , an energy balance equation can be found,

$$C_j \frac{dT_j}{dt} = \sum_{i=1, i \neq j}^n \frac{1}{R_{th_{i,j}}} (T_i - T_j) + P_j \quad (j = 1, \dots, m) \quad (2.115)$$

where

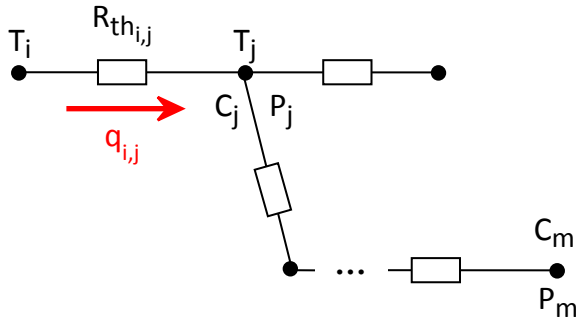


Figure 2.31: Basic configuration of an equivalent nodal network.

P_j represents the heat source related to the node.

T_j represents the node temperature.

$R_{th_{i,j}}$ represents the thermal resistance between nodes.

C_j represents the equivalent heat capacity of the node.

Rearranging the equation,

$$\begin{aligned} \frac{dT_j}{dt} = \frac{1}{C_j} \sum_{i=1}^m \frac{1}{R_{th_{i,j}}} T_i - \frac{1}{C_j} \sum_{i=1}^n \frac{1}{R_{th_{i,j}}} T_j + \frac{1}{C_j} P_j \\ + \frac{1}{C_j} \sum_{i=m+1}^n \frac{1}{R_{th_{i,j}}} T_i \quad (j = 1, \dots, m) \end{aligned} \quad (2.116)$$

Therefore, there will be m first order differential equations, whose behavior can be expressed with a matrix representation,

$$dT/dt = A T + B U, \quad (2.117)$$

where

T represents the node temperatures (T_1 to T_m).

U represents the external excitations (P_1 to P_m followed by T_{m+1} to T_n).

A and B represent the system matrices.

$$T = \begin{bmatrix} T_1 \\ T_2 \\ \vdots \\ T_m \end{bmatrix}_{m \times 1} \quad U = \begin{bmatrix} P_1 \\ P_2 \\ \vdots \\ P_m \\ T_{m+1} \\ \vdots \\ T_n \end{bmatrix}_{n \times 1}$$

$$A = \begin{bmatrix} -\frac{1}{C_1} \sum_{i=1}^n \frac{1}{R_{th_{i,1}}} & \frac{1}{C_1} \frac{1}{R_{th_{2,1}}} & \cdots & \frac{1}{C_1} \frac{1}{R_{th_{m,1}}} \\ \frac{1}{C_2} \frac{1}{R_{th_{1,2}}} & -\frac{1}{C_2} \sum_{i=1}^n \frac{1}{R_{th_{i,2}}} & \cdots & \frac{1}{C_2} \frac{1}{R_{th_{m,2}}} \\ \vdots & \vdots & \ddots & \vdots \\ \frac{1}{C_m} \frac{1}{R_{th_{1,m}}} & \frac{1}{C_m} \frac{1}{R_{th_{2,m}}} & \cdots & -\frac{1}{C_m} \sum_{i=1}^n \frac{1}{R_{th_{i,m}}} \end{bmatrix}_{m \times m}$$

$$B = \left[\begin{array}{cccc|ccc} \frac{1}{C_1} & 0 & \cdots & 0 & \frac{1}{C_1} \frac{1}{R_{th_{m+1,1}}} & \cdots & \frac{1}{C_1} \frac{1}{R_{th_{n,1}}} \\ 0 & \frac{1}{C_2} & \cdots & 0 & \frac{1}{C_2} \frac{1}{R_{th_{m+1,2}}} & \cdots & \frac{1}{C_2} \frac{1}{R_{th_{n,2}}} \\ \vdots & \vdots & \ddots & \vdots & \vdots & \ddots & \vdots \\ 0 & 0 & \cdots & \frac{1}{C_m} & \frac{1}{C_m} \frac{1}{R_{th_{m+1,m}}} & \cdots & \frac{1}{C_m} \frac{1}{R_{th_{n,m}}} \end{array} \right]_{m \times n}$$

The use of an equivalent nodal network, along with the matrix representation makes the manipulation and resolution of the thermal problem much easier.

2.4.2. Heat Transfer Coefficients

Heat transfer takes place only when there is a temperature difference. Heat energy moves from a higher temperature potential to a lower potential one [John H. Lienhard IV and John H. Lienhard V, 2004]. Three modes of heat transfer can be distinguished: conduction, convection, and radiation. Usually in power magnetic design, linear thermal resistances, or at least non-temperature dependent thermal resistances, are used to define the various heat transfer mechanisms. However, only conduction heat transfer presents this kind of behavior, while convection and radiation heat transfer mechanisms are different.

The thermal resistance of a material from node i to node j is defined as,

$$R_{i,j} = \frac{1}{h_{i,j} A} \quad (2.118)$$

where A is the considered heat transfer area, and $h_{i,j}$ represents the equivalent heat transfer coefficient. This equivalent coefficient can be a pure conductance, i.e. only conductive heat transfer, or an equivalent conductance, e.g. radiative or convective heat transfer. The subsequent sections deal with the basic laws of heat transfer modes and their respective heat transfer coefficients.

2.4.2.1. Conduction

Heat transfer by conduction can take place in solids, liquids or gases. Conduction is a mechanism that takes place when the media is stationary and is governed by Fourier's law [John H. Lienhard IV and John H. Lienhard V, 2004], which predicts the rate of heat transfer:

The heat flux, q , resulting from thermal conduction is proportional to the magnitude of the temperature gradient and opposite to its sign.

$$q = -\lambda \nabla T \quad (2.119)$$

where the proportionality factor λ , called the thermal conductivity, is a property of the material.

The one-dimension scalar form of the Fourier Law becomes:

$$q = \lambda \frac{\Delta T}{l} \quad (2.120)$$

where l is the thickness of the material in the direction of the heat flux, and from which the conduction heat transfer coefficient, h_c , is defined as

$$h_c = \frac{\lambda}{l}, \quad (2.121)$$

2.4.2.2. Convection

Convection heat transfer occurs when heat is transferred in a moving medium. Convection heat transfer is usually considered when heat is transferred from a solid plane at one temperature to an adjacent moving fluid at another temperature. Heat energy is conducted from the solid to the moving fluid, where energy is carried away by combined effects of conduction and bulk motion of the fluid. The heat transfer from the solid system to the fluid can be expressed by the empirical equation (2.122), known as Newton's Law of Cooling [John H. Lienhard IV and John H. Lienhard V, 2004].

$$q = h_{cc} (T_s - T_f) \quad (2.122)$$

where T_s and T_f referred to the solid and fluid temperature (far from the solid), respectively.

The proportionality factor, h_{cc} , is known as the convection equivalent conduction coefficient. This coefficient depends on the geometry of the system, the fluid flow pattern near the surface and the fluid properties. The fluid flow pattern can be natural or forced, like in the case of fans, pumps or turbines. The convection equivalent conduction coefficient, h_{cc} , is a combination of the convection and conduction heat transfer mechanisms, and it is defined as

$$h_{cc} = Nu \frac{\lambda}{D}, \quad (2.123)$$

where λ is the thermal conductivity of the fluid, and D refers to the surface characteristic length. Depending on the surface the characteristic length will be defined with (2.124).

$$D = h \quad \text{for vertical surfaces} \tag{2.124}$$

$$D = \frac{2wl}{w+l} \quad \text{for horizontal surfaces}$$

where h is the height of the vertical surface, and l and w are the length and the width of the horizontal surface, respectively.

The dimensionless Nusselt number, Nu , represents the flow of the fluid near the surface, for laminar flows depending on the surface and heat direction, the Nusselt number will present different values. In case of vertical surfaces (2.125).

$$Nu = 0.56 (Gr \cdot Pr)^{0.25} \quad \text{for} \quad 1 \cdot 10^4 < Gr < 1 \cdot 10^9 \tag{2.125}$$

For horizontal surfaces with an upward heat flux

$$Nu = 0.54 (Gr \cdot Pr)^{0.25} \quad \text{for} \quad 1 \cdot 10^5 < Gr < 2 \cdot 10^7 \tag{2.126}$$

and finally for a downward heat flux

$$Nu = 0.27 (Gr \cdot Pr)^{0.25} \quad \text{for} \quad 3 \cdot 10^5 < Gr < 3 \cdot 10^{10} \tag{2.127}$$

where Gr and Pr are the dimensionless Grasshof and Prandtl numbers, respectively.

$$Gr = \frac{\rho^2 g \beta D^3 \Delta T}{\mu^2} \tag{2.128}$$

$$Pr = c_p \frac{\mu}{\lambda} \tag{2.129}$$

where ρ , β , μ , λ and c_p are the density, volumetric expansion coefficient, dynamic viscosity, thermal conductivity and specific heat capacity of the fluid, respectively.

All these variables are evaluated at film temperature, average between the fluid temperature and the surface temperature.

Once the definition for the Nusselt number is settled, the heat transfer coefficient expression can be reduced to,

$$h_{cc} = k_{cc} \left(\frac{\Delta T}{D} \right)^{0.25} \quad (2.130)$$

where

$$k_{cc} = k_c \lambda^{0.75} \left(\frac{c_p \rho^2 g \beta}{\mu} \right)^{0.25} \quad (2.131)$$

and k_c depends on the selected surface (2.125), (2.126) or (2.127).

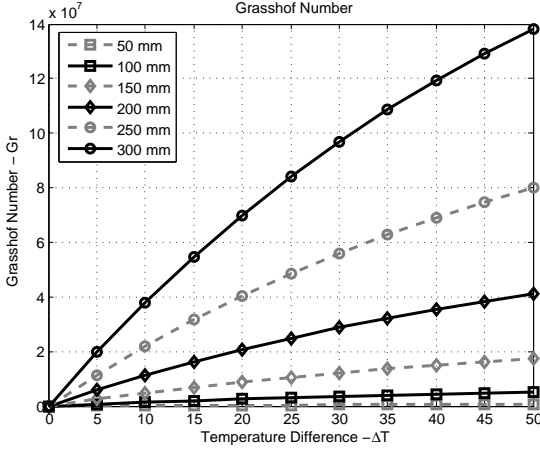


Figure 2.32: Grashof number for various characteristic lengths D , with $T_f = 30^\circ\text{C}$. Fluid air.

It should be noted that previously introduced constants for each Nusselt number are correct while the heat flow keeps laminar, i.e. while the Grashoff number rests within the boundaries introduced for each convection surface.

2.4.2.3. Radiation

Thermal radiation can take place without a medium. Solid surfaces, gases, and liquids all emit, absorb, and transmit thermal radiation to different extends. The radiation heat transfer is described by Stefan-Boltzmann law,

$$Q = A \varepsilon \sigma T_s^4 \quad (2.132)$$

where σ is the Stefan-Boltzmann constant $5.669 \cdot 10^{-8}$, A represents the radiation surface, ε is the emissivity of the radiative surface, and T_s is the surface temperature. Considering a simple two body system with non-participating medium, the radiation equation can be written as

$$Q_{ij} = A_i \varepsilon_i \sigma (T_i^4 - T_j^4) \quad (2.133)$$

where Q_{ij} is the net radiation from body i with higher temperature T_i to body j with lower temperature T_j , A_i represents the radiation surface and ε_i the emissivity of body i .

For a linear resolution of the nodal network, the radiative flow can be approximated by

$$Q_{ij} = A_i h_{ij} (T_i - T_j) , \quad (2.134)$$

where the radiation heat transfer coefficient is defined by

$$h_{ij} \approx 4 \sigma \varepsilon_i \langle T \rangle^3 \quad (2.135)$$

and where $\langle T \rangle$ is the average temperature of the nodes. The original radiation equation (2.133) along with the linear approximation is illustrated in Fig. 2.33, where the introduced error is shown.

2.4.3. Basic Static Network

The analyzed transformer structure, as well as, the basic equivalent nodal network are illustrated in Fig. 2.34. It is a shell-type transformer with a conduction

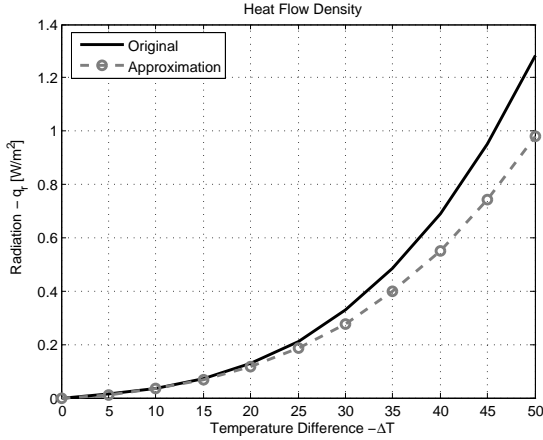
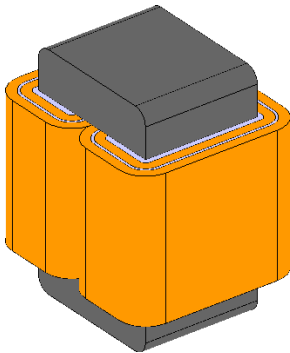
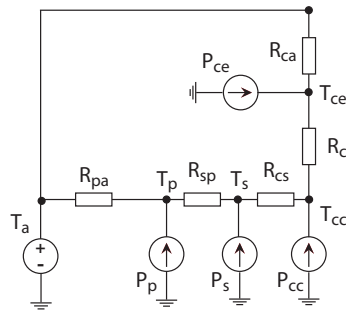


Figure 2.33: Radiation approximation for various temperature differences with $T_f = 30^\circ\text{C}$ and $\varepsilon = 0.9$.

foil for the primary, as well as, for the secondary with an isolation layer in between, and between the secondary and the core.



(a) Transformer geometry.



(b) Equivalent nodal network.

Figure 2.34: Analyzed transformer geometry and basic equivalent nodal network.

A transient thermal model can be found in [Villar et al., 2008], which varies slightly compared to the one introduced in this section.

Step 1. Node Selection Although it is supposed that core losses are uniformly distributed throughout the whole magnetic volume, the core is divided into two zones. The heat generated in the center leg of the core has to be conducted to the external part before it is dissipated by convection and radiation, thus increasing center leg temperature with regard to the external part.

Copper losses are also uniformly distributed in each of the foil conductors. Each conductor represents a different temperature node, due to the thermal barrier imposed by the isolation layer.

Step 2. Governing Equations Once the equivalent thermal circuit is chosen, the energy balance equations can be easily defined.

$$0 = \frac{1}{R_{ce}} (T_{ce} - T_{cc}) + \frac{1}{R_{cs}} (T_s - T_{cc}) + P_{cc} \quad (2.136)$$

$$0 = \frac{1}{R_{ce}} (T_{cc} - T_{ce}) + \frac{1}{R_{ca}} (T_a - T_{ce}) + P_{ce} \quad (2.137)$$

$$0 = \frac{1}{R_{cs}} (T_{cc} - T_s) + \frac{1}{R_{sp}} (T_p - T_s) + P_s \quad (2.138)$$

$$0 = \frac{1}{R_{sp}} (T_s - T_p) + \frac{1}{R_{pa}} (T_a - T_p) + P_p \quad (2.139)$$

In a matrix form,

$$0 = AT + BU \quad (2.140)$$

with

$$T = \begin{bmatrix} T_{cc} \\ T_{ce} \\ T_s \\ T_p \end{bmatrix}_{4 \times 1} \quad U = \begin{bmatrix} P_{cc} \\ P_{ce} \\ P_s \\ P_p \\ T_a \end{bmatrix}_{5 \times 1} \quad B = \begin{bmatrix} 1 & 0 & 0 & 0 & | & 0 \\ 0 & 1 & 0 & 0 & | & \frac{1}{R_{ca}} \\ 0 & 0 & 1 & 0 & | & 0 \\ 0 & 0 & 0 & 1 & | & \frac{1}{R_{pa}} \end{bmatrix}_{4 \times 5}$$

$$A = \begin{bmatrix} -\frac{1}{R_{ce} + R_{cs}} & \frac{1}{R_{ce}} & \frac{1}{R_{cs}} & 0 \\ \frac{1}{R_{ce}} & -\frac{1}{R_{ce} + R_{ca}} & 0 & 0 \\ \frac{1}{R_{cs}} & 0 & -\frac{1}{R_{cs} + R_{sp}} & \frac{1}{R_{sp}} \\ 0 & 0 & \frac{1}{R_{sp}} & -\frac{1}{R_{sp} + R_{pa}} \end{bmatrix}_{4 \times 4}$$

Step 3. Loss Determination Following the theory introduced in Sections 2.2 and 2.3.

Step 4. Thermal Resistance Within the magnetic core and through the winding layers, heat is transferred by conduction. The equivalent heat transfer coefficient is given by (2.121). When there is more than one material in series between two nodes, like in the transformer winding (copper+isolation+copper, between the centers of each foil conductor), the resulting equivalent thermal resistance is given by

$$R_{eq} = \sum_{i=1}^n \frac{1}{h_{c_i} A_i} = \sum_{i=1}^n R_i \quad (2.141)$$

where A_i represents the external surface of the winding layer. The thermal conductivity of copper is higher than the thermal conductivity of the isolation material, thus the contribution of the conductor layers in the equivalent conduction conductance can be neglected.

The equivalent thermal resistance between the core or winding and the fluid is a combination of the convection and radiation heat transfer resistances, as mentioned before. Both thermal resistance are in parallel, reaching an equivalent thermal resistance for all the transformer surfaces, vertical, as well as, horizontal surfaces (2.142).

$$R_{eq} = \frac{1}{\sum_{i=1}^n A_i \left(\frac{1}{h_{cc_i}} + \frac{1}{h_{r_i}} \right)} \quad (2.142)$$

In transformer structures the correct characteristic length selection can be confusing due to the extending winding volume. In order to select the right equivalent convection heat transfer coefficient, several fluid flow finite element simulations have been carried out. The horizontal characteristic length of transformers is quite clearly determined, however, the vertical height of the transformer has to be modified, because it does not directly correspond to the characteristic length of the vertical surface (see Fig. 2.35).

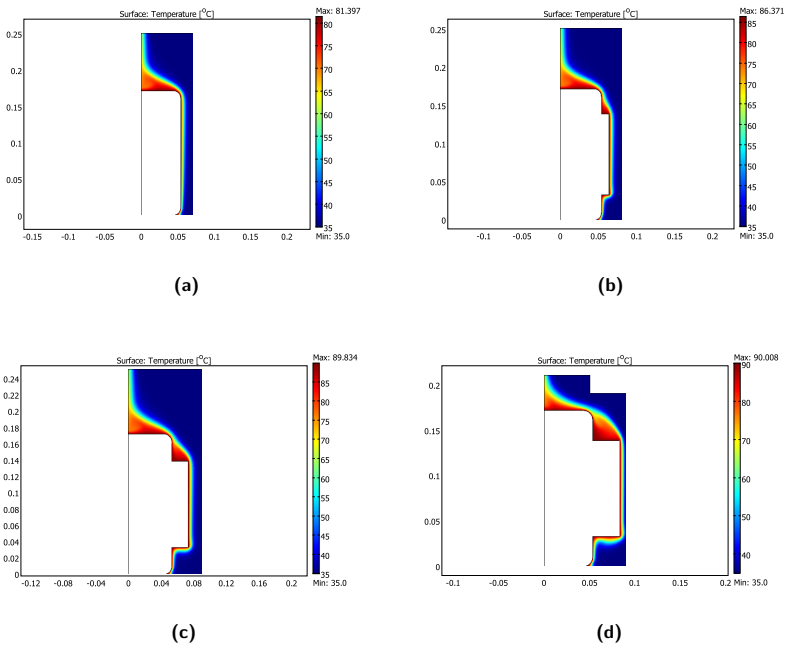


Figure 2.35: Temperature distribution for different winding geometries.

In the vertical surfaces involving windings, the heat flux changes the path depending on the relationship between the height and the width of the bobbin. Instead of following a vertical flux direction, the heat flux describes a diagonal path in the corners of the bobbin. If the heat flux path gets longer (see Fig. 2.35d),

transformer temperature gets higher, which corresponds to a larger characteristic length and a worst convection coefficient value (2.130). It should be mentioned, that within this fluid flow simulations, the bottom surface of the transformer is supposed to be isolated.

Step 5. System Solution The equivalent thermal resistances between the winding or core surfaces and the surrounding air are temperature dependent, therefore the system of equations is solved iteratively so as to minimize the following equation:

$$\mathbf{0} = \mathbf{A}(\mathbf{T}) \mathbf{T} + \mathbf{B}(\mathbf{T}) \mathbf{U}(\mathbf{T}) \quad (2.143)$$

And finally with the results from this equation the temperature rise within different parts of the transformer is determined.

2.5. Conclusions

In this chapter several transformer characterization methods have been introduced, both for the winding and for the magnetic core. Winding characterization shows a large number of studies within the literature related to Dowell's equation and its validity, which was proven to be accurate. However, there is a lack of Litz wire winding characterization comparison, where the validity of each proposed expression can be verified. In this chapter, those equations within the literature have been compare with FEM simulations and a simplified expression proposed, suitable for medium-frequency transformer windings.

In relation with core losses, several methodologies have been briefly introduced in order to have a general overview of the complexity and suitability of each methodology. For medium-frequency transformer characterization, the empirical expressions were found as the best suited ones, reaching a high level of accuracy, at least with sinusoidal waveforms. Their applicability in medium-frequency transformers will be analyzed in the following chapter.

Finally, the thermal characterization procedure has been introduced with a specific example where the required criteria for a correct model have been pointed out.

3

Medium-Frequency Transformer Design Methodology

Summary

Power transformer design entails the selection of the right magnetic core, along with the optimal conductor size and winding disposition following different design criteria like; efficiency, volume, weight, cost, temperature rise or isolation. In this chapter a design methodology for medium-voltage medium-frequency power transformers is introduced applying the theory presented in the previous chapter. The methodology is based on existing high-power low-frequency magnetic cores, suitable for medium-frequency applications.

3.1. Design Flow Chart

Usually, low-power magnetic cores, due to their wide application, have standard and fixed dimensions. Therefore, optimized transformer or inductance designs are based on look-up tables where various available cores are introduced, and the best suited ones are selected according to the power handling requirements of the application [McLyman, 2004]. Afterwards, the loss sharing criterion between the core and the windings is determined, as well as the maximum magnetic induction value. Then, winding turn number and wire diameter are established, and winding losses reevaluated. If volumetric or thermal limits are accomplished the design is finished. However, high-power magnetic cores are designed on demand [METGLAS], or with a few dimensional references or ranges. Thus, the optimized design of the magnetic component is not based on the selection of the right magnetic core but on the definition of its best dimensions.

In medium-voltage medium-frequency applications the value of the leakage inductance is essential for proper operation, both of resonant and non-resonant converters. The volume and weight needs to be optimized by tuning correctly the leakage inductance of the transformer without adding any external inductances. Therefore, the optimization process needs to consider, besides maximum power loss or minimum volume, the value of the leakage inductance. If the final geometry of the winding is not known, the leakage inductance can not be correctly determined and the optimization process neglects an essential design criterion.

The winding geometry will depend on the chosen conductor (foil, solid or Litz), which will present an optimal diameter for each current waveform and winding

structure. Consequently, the proposed methodology is based on the definition of the winding area, by making use of pre-established optimal conductor sizes, for which the best ratio between ac and dc winding losses will be fixed. This is a significant change compared to conventional medium/high-frequency design methodologies. Then, the most suitable transformer core is designed by optimizing parameters like maximum power loss, equal loss sharing or maximum thermal limits, along with the adjustment of the leakage inductance value. Thus, once the optimal conductor area is determined, the length of the winding and the core are adjusted to reach the best transformer solution. The knowledge of the final winding geometry, with actual conductor sizes, is essential to tune the leakage inductance value and optimize transformer geometry and efficiency. The flow chart of the proposed methodology for medium-voltage medium-frequency transformer design is presented in Fig. 3.1.

Initially, main desired transformer characteristics are defined (user defined inputs): rated power, voltage, frequency, isolation requirements, magnetic material, current waveform, and desired leakage inductance. Then, a preliminary study of the optimal conductor diameter is carried out, which together with user-defined inputs, will be used to calculate the initial variable guess (number of turns, number of layers, maximum magnetic induction, effective cross-sectional area, etc.) of the optimization process.

During each iteration of the process, several calculations are made. First, (1) the number of turns is evaluated, and (2) the conductor is selected (from a look-up table), which is used to (3) define the dimensions of the windings. Afterwards, (4) the core geometry is defined and (5) transformer losses are estimated, together with its (6) power dissipation capability (temperature rise). Finally, (7) the leakage inductance is determined from the winding geometry. With these calculations, the optimization functions are checked until the guessed variables accomplish the design criteria limits.

In the following sections, each of the optimization steps will be thoroughly explained based on Fig. 3.1: Data, Process and finally, Optimization.

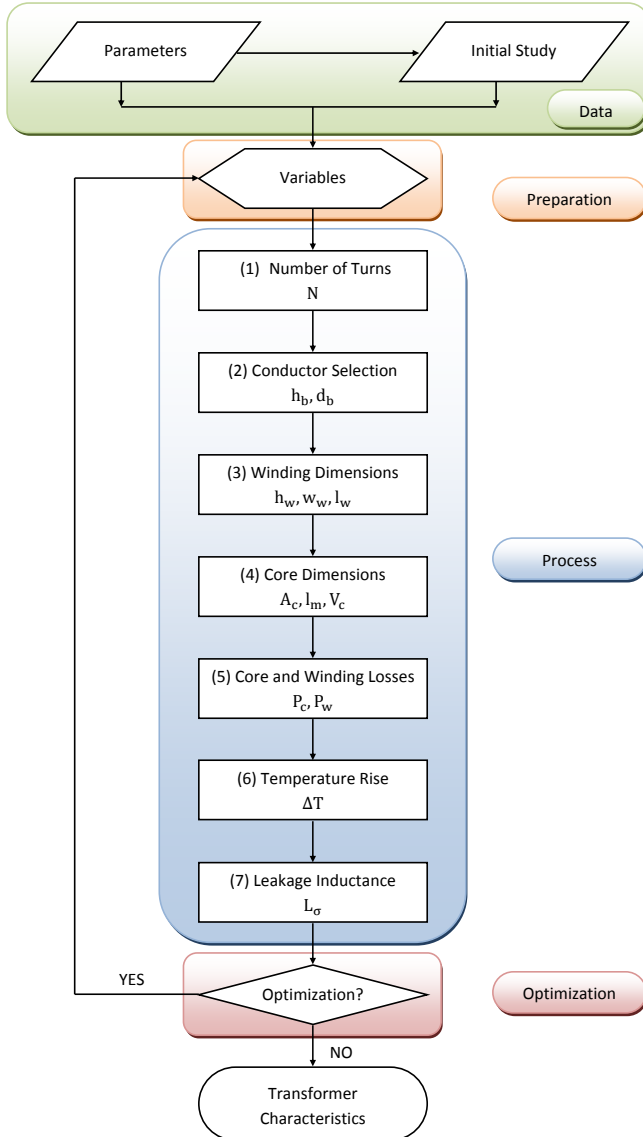


Figure 3.1: Proposed medium-frequency transformer design methodology flow chart.

3.2. Data: Transformer Characteristics and Constraints

In an initial stage, transformer specifications are determined and the magnetic material is selected, the maximum current density set and the optimal wire look-up table is generated.

3.2.1. High-Power Medium-Frequency Magnetic Cores

In low-power applications, the selection of the magnetic material, as well as the optimum magnetic core choice can be a complex task. Given the great number of low-power high-frequency applications, manufacturers offer a wide variety of magnetic core materials, shapes and sizes. Nevertheless, in high-power applications, the choices are drastically reduced.

Not so long ago, the operation of magnetic materials in medium-voltage medium-frequency applications was inconceivable due to the limitations of high-power semiconductor devices. Nevertheless, with the continuous improvement of power semiconductors, as well as converter topologies and switching techniques, the incursion of magnetic devices in medium-voltage medium-frequency applications is feasible. Although there are great expectations with SiC semiconductors for future medium-voltage applications, until present high-power IGBTs are the most widely-spread and known solution for medium-voltage medium-frequency applications (with IGCTs following the lead). They can offer the required operational characteristics within, obviously, some voltage and frequency limits. Depending on the converter topology, power and the selected control principle, commercially available high-power IGBTs can vary considerably. For example, in the case of resonant converters with almost lossless commutations, the operation frequency of high-power semiconductors can be as high as 10 kHz (see Table 1.1). Nevertheless, if the converter is a hard/soft-switching one, where only some of the commutations are lossless, the switching frequency will be limited to approximately 2 kHz.

One of the objectives of new high-voltage power electronic transformers is to increase the power density of the whole conversion system, thus, an optimized transformer and converter operation frequency will range between 1 kHz to 10 kHz (see Table 1.1). This application requires a different solution with respect to

conventional high-power low-frequency applications (silicon-steel alloy, FeSi), and high-power high-frequency applications (ferrites). In the first case, FeSi materials, although they present a high-saturation induction (~ 2 T), they have significant high-frequency losses and their operation frequency is limited usually to 400 Hz [Hugo et al., 2007]. In the second case, ferrites [Aggeler et al., 2008; Morren et al., 2001], due to their low-saturation induction (~ 0.4 T), their application in medium-voltage systems will result in too voluminous designs, because a large number of winding turns or large magnetic cross-sectional areas will be necessary in order to cope with medium voltages with the above mentioned frequencies.

As a result, two special magnetic materials can be best suited for this kind of applications: iron-based amorphous alloys [UNIFLEX],[Meyer et al., 2007] and nanocrystalline materials [Akagi and Inoue, 2006; Heinemann, 2002; Steiner and Reinold, 2007]. The magnetic structure of this two materials is transformed to exhibit less resistance to magnetic field variations, keeping as far as possible the high-saturation induction values of FeSi alloys. The former, is a non-crystalline amorphous alloy, which presents a disordered structure, known as glass, and as a result they are commonly referred as "metallic glasses". The latter, is a crystalline alloy which is derived from crystallizing amorphous ribbons of specific families. Characterized by 10 nm-25 nm sized grains, they are homogeneously dispersed in an amorphous matrix. Nanocrystalline cores, due to their nanometric particles, exhibit low-magnetic loss densities with acceptable saturation inductions (~ 1.2 T), having high efficiencies [VITROPERM]. Nevertheless, although a few power prototypes made with nanocrystalline materials can be found in the literature [Heinemann, 2002], the magnetic core for high-power applications is not standardized and they are only manufactured on demand. Besides the lack of standardized commercially available cores, the manufacturing cost is very high, resulting in a final expensive magnetic core, which penalizes their total cost and makes them for this application for the time being, non-affordable. In contrast, iron-based amorphous materials, due to their longer existence (since the 1980s), and current market deployment can offer standardized cores for low-frequency high-power distribution transformers with high-saturation inductions (~ 1.56 T), which can also be used in the low/medium-frequency range [UNIFLEX],[Meyer et al., 2007]. According to manufacturers [METGLAS], this magnetic material presents lower loss densities at

low frequencies (50 Hz-60 Hz) than FeSi alloys. Thereby, according to the current technological state-of-the-art, the most feasible medium-frequency transformer for medium/low-voltage applications, will be based on IGBTs and iron-based amorphous alloys, and consequently, these will be the technologies considered in the rest of this report.

3.2.2. The Amorphous Magnetic Core

Amorphous alloy cores are made of micro-thin ribbons ($25\ \mu\text{m}$), namely tape wound cores. Power System cores or AMDT cores (Amorphous Material Distribution Transformer), present an almost C-core structure [METGLAS] with slight modifications due to thermal and structural requirements. In order to propose a general methodology, the C-core structure illustrated in Fig. 3.2 has been taken as a reference. The only difference with the AMDT core lies on the joint build, which in the upper part describes a semicircle, while in this case is supposed to be symmetrical. Moreover, there is no cooling duct within the analyzed core.

According to the manufacturer, Power System cores have the dimensional limits summarized in Table 3.1, which will be the boundary constraints of the optimiza-

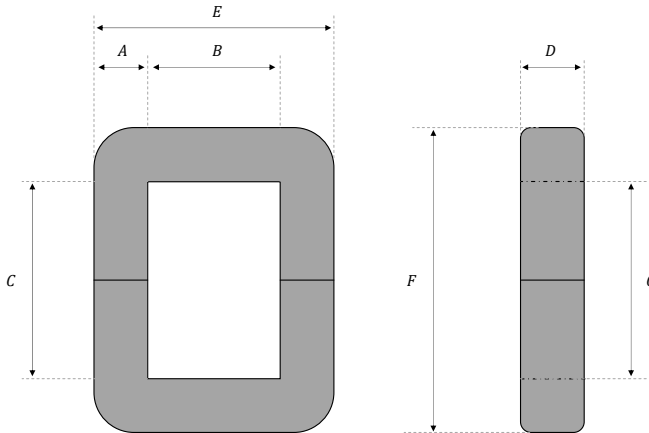


Figure 3.2: C-core dimensions.

Description		Minimum	Maximum	Increment
Column Width	<i>A</i>	25 mm	75 mm	1 mm
Window Width	<i>B</i>	80 mm	250 mm	5 mm
Window Height	<i>C</i>	180 mm	600 mm	10 mm
Core Maximum Weight	<i>W_c</i>	30 kg	225 kg	
Depth	<i>D</i>	142/170/213 mm + 4 mm edge cover		
Outer Circumference Limit	<i>l_{o,max}</i>	< 2.5 m		

Table 3.1: Dimensional limits for iron-based amorphous alloys in Power System cores [METGLAS].

tion process. Mention that the manufacturer offers three standard ribbon widths, i.e. core depths, although other lengths can be manufactured on demand. The following study will be limited to this three standard lengths, although multiple core combinations are not neglected.

The heat dissipation capacity of Power System cores will be evaluated to establish the maximum current density of the possible transformer geometries, and in order to have an initial design criterion.

3.2.3. Heat Dissipation Capacity

A given volume has a maximum power dissipation capacity if natural convection is considered. The external surfaces of the volume transfer heat by both convection and radiation, and from horizontal and vertical surfaces (see Section 2.4.2).

$$\max P_d = \max (P_{conv} + P_{rad}) \tag{3.1}$$

Thus, maximum dissipation power will be proportional to minimum thermal resistance, $\max P_d \propto \min R_{sa}$, which is a parallel combination of convective and

radiative thermal resistances (3.2).

$$\min R_{sa} = \min \left(\frac{R_{conv} R_{rad}}{R_{conv} + R_{rad}} \right) = \min \left(\frac{1}{h_{cc} A + h_r A} \right) \quad (3.2)$$

Then, the relationship between heat dissipation capacity and convection and radiation coefficients is

$$\max P_d \propto \max (h_{cc} A + h_r A) \quad (3.3)$$

As mentioned in Section 2.4.2, depending on the surface direction the convection heat transfer coefficients and the radiation coefficient vary according to (3.4).

$$\begin{aligned} \max P_d \propto & \left[k_h \left(\frac{w+l}{2wl} \right)^{0.25} (2wl) + k_v \left(\frac{1}{h} \right)^{0.25} (2hw)(2hl) \right] (\Delta T)^{0.25} \\ & + 4\sigma\varepsilon(T)^3 [2(hw+hl+wl)] \end{aligned} \quad (3.4)$$

This maximum power dissipation equation will be used in further sections to establish the thermal limits of Power System cores.

3.2.4. Loss Distribution for Maximum Efficiency

The efficiency of a transformer is the ratio between the output P_{out} and the input P_{in} powers.

$$\eta = \frac{P_{out}}{P_{in}} \quad (3.5)$$

The difference between input and output power corresponds to transformer losses.

$$P_{in} = P_{out} + P_d \quad (3.6)$$

where $P_d = P_w + P_c$, which is the sum of winding and core losses, respectively. Thus, rewriting the expression for the efficiency, it turns into (3.7).

$$\eta = \frac{P_{out}}{P_{out} + P_d} \quad (3.7)$$

No-load losses, or core losses depend on the maximum magnetic induction value and on the frequency of the waveform (see subsection 3.3.4). In almost every optimized medium-frequency conversion topology [Aggeler et al., 2008; Norrga, 2006; Reinold and Steiner, 1999] the maximum magnetic induction and the frequency of the voltage waveform are kept constant. Thus, core losses will be constant, too. However, winding losses depend on the square of the load current, and therefore on the square of the output power (3.8).

$$P_w = R_{ac} I_n^2 \propto P_{out}^2 \quad (3.8)$$

Rewriting, once more, the expression for transformer efficiency,

$$\eta = \frac{P_{out}}{P_{out} + (P_c + cP_{out}^2)} \quad (3.9)$$

where c is a constant value.

The maximum efficiency of the transformer is determined from (3.10).

$$\max \left(\frac{d\eta}{dP_{out}} \right) = \max \left(\frac{P_c + P_{out} + cP_{out}^2 - P_{out}(1 + 2cP_{out})}{P_c + P_{out} + cP_{out}^2} \right) \quad (3.10)$$

which results in equal core and winding losses for maximum transformer efficiency [McLyman, 2004].

$$P_c = cP_{out}^2 = P_w \quad (3.11)$$

3.2.5. Maximum Power Level

The maximum dissipation capacity is the maximum of the sum of transformer core losses and winding losses (3.12). As mentioned in the previous subsection, for maximum efficiency, both losses must be equal. However, this is not usually attainable due to geometrical limitations.

$$\max P_d = \max (P_c + P_w) \quad (3.12)$$

In order to determine the maximum dissipation capability of medium-frequency power transformers, and therefore the maximum current and power densities, two possible transformer configurations have been studied: shell-type and core-type transformers (see Fig. 3.3). Although there are three-phase topologies in the literature for medium-voltage medium-frequency applications [Meyer et al., 2007], within this thesis only single-phase transformers will be considered.

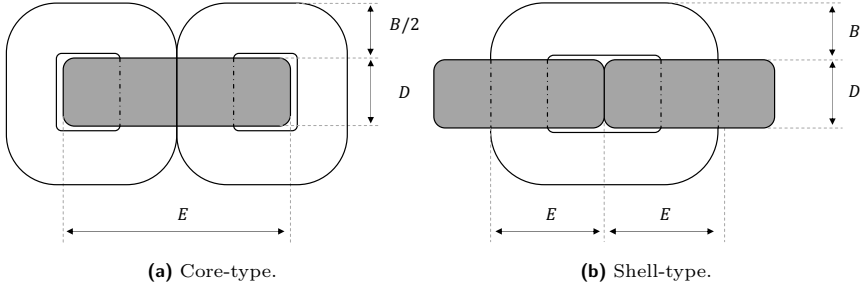


Figure 3.3: Core-type or shell-type transformer structures for the same fictive volume.

In the shell-type transformer, the core is built with two C-cores (see Fig. 3.3b), and the maximum winding part will be equal to the core window width, B . In the case of the core-type transformer, the maximum winding part around the core will have half the core window value, $B/2$ (see Fig. 3.3a). Therefore, for the same total fictive volume, $V_t = w l h$ (see Table 3.2), the shell-type transformer has 15% more magnetic material, while, it has a 36% less winding part. Therefore, for a maximum dissipation capacity and equal loss distribution, the maximum magnetic induction and maximum current density will vary too.

Within this study, the same possible transformer cores are considered, with the constraints introduced in Table 3.1. Therefore, the shell-type transformer will reach higher volumes, and thus, higher power levels. Considering the limitations of Table 3.1 and using the expressions of Table 3.2, the maximum output power of a wide range of possible transformers is illustrated in Fig. 3.4. All possible core window areas for an specific core depth ($D = 146$ mm) and for three core column widths ($A = [25$ mm, 50 mm, 75 mm]) are plotted in Fig. 3.4. In order to determine

Description		Core-Type	Shell-Type
Core Mean Length	l_m	$2(B + C) + 4A$	$2(B + C) + 4A$
Core Total Area	A_c	AD	$2AD$
Core Volume	V_c	$l_m A_c$	$l_m A_c$
Winding Mean Length	l_w	$2(D + A) + \pi(B/2)$	$2(D + 2A) + \pi B$
Winding Total Area	A_w	CB	CB
Winding Volume	V_w	$l_w A_w$	$l_w A_w$
Total Width	w	$E + B$	$2E$
Total Height	h	F	F
Total Depth	l	$D + B$	$D + 2B$
Total Fictive Volume	V_t	wlh	wlh
Total Fictive Surface	S_t	$wl + wh + lh$	$wl + wh + lh$

Table 3.2: Dimensional characteristics for the core-type and shell-type transformers.

the maximum power level of this set of transformers, an efficiency of $\eta = 99\%$ is considered (3.13).

$$P_{out} = \frac{\eta}{1 - \eta} P_d \tag{3.13}$$

Moreover, mention that the different dimensions of the transformer, like the core column width and depth, or the height of the core window area are considered separately to point out the importance not only of the core surfaces but also of the composition of those surfaces, e.g. the ratio between the width and the depth of the core column.

The transformers are supposed to be naturally cooled (see Appendix B.1 for fluid properties), with an emissivity of 0.8, within an ambient temperature of 40° and a maximum surface temperature of 100° . Moreover, the results are plotted

for the area product [McLyman, 2004] of each possible core configuration. The area product is the product of the core window area and core cross-sectional area (3.14), and according to [McLyman, 2004] the area product is proportional to the power handling capability of the transformer, and is used by some manufacturers to catalogue their cores [METGLAS].

$$A_p = A_w A_c \quad (3.14)$$

On the one hand, in Fig. 3.4, one can clearly see the difference in power handling capability between core-type and shell-type transformers. However, for both transformer configurations the smallest core column width presents the best thermal behavior, the higher power level to area product ratio. On the other hand, it is also clearly illustrated that the power level of the transformer and its area product are not linearly related, for the same area product there are multiple maximum power levels. Although all possible transformer geometries can not be exactly described with the same behavior, apparently there exists a dependency on the ratio between the core column width and its depth, $\propto D/A$. For higher ratios all possible transformer structures present a better thermal behavior, with higher

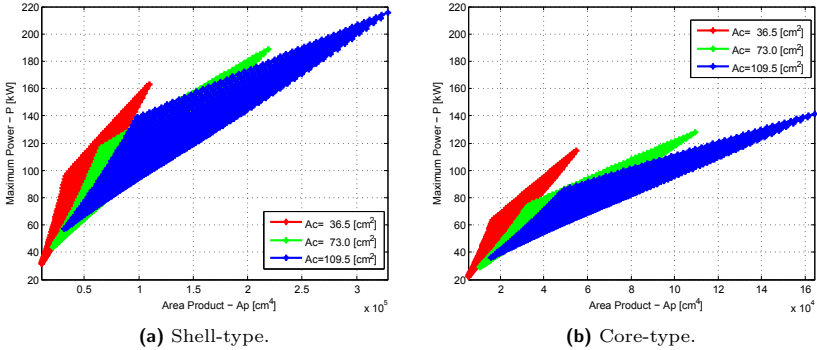


Figure 3.4: Maximum power, supposing an efficiency of $\eta = \%99$. Possible transformer configurations with $D = 146$ mm and $A = [25$ mm (red), 50 mm (green), 75 mm (blue)]. Natural convection with $T_{amb} = 40^\circ\text{C}$, $T_{surface} = 100^\circ\text{C}$ and $\varepsilon = 0.8$.

power levels in equal area products.

3.2.6. Maximum Current Density

Once the maximum dissipation capability has been determined, the maximum current density of the winding can be determined. Transformer winding losses, considering an ideal resistance ratio $F_r = 4/3$ [Hurley et al., 2000], depend on the current density J_n , on the filling or packing factor of the winding p_f , and on the conductivity of the conductor σ [Mohan et al., 2002].

$$P_w = F_r R_{dc} I_n^2 = \left(\frac{4}{3} J_n^2 p_f \sigma \right) V_w \quad (3.15)$$

where V_w is the total volume of the winding, with

$$R_{dc} = \frac{l_w}{A_b \sigma p_f} \quad \text{and} \quad I_n^2 = (J_n A_b p_f)^2 \quad (3.16)$$

and where A_b is the total conductor surface.

In high-voltage high-power transformers the packing factor is usually small due to isolation requirements. Moreover, in medium-frequency applications the winding will be composed probably of Litz wire conductors, which inherently present low packing factors. Therefore, for comparison purposes a packing factor of 0.2 has been selected.

Regarding maximum power levels, a considerable difference was detected between core-type and shell-type transformers. However, the maximum current density hardly changes from one structure to the other (see Fig. 3.5a and Fig. 3.5b), because the winding window area variation is the same in both cases. The small current density variations come from the difference between winding and core part ratios in core-type and shell-type transformers.

According to these results, the maximum current density in dry-type transformers should not be higher than 1.7 A/mm^2 , with a filling factor of 0.2. This filling factor value is low, but typical in high-power transformer designs, where high-isolation spaces are required. Thus, a more compact winding design should have an even lower maximum current density in the windings for an identical power loss distribution. Obviously, if the maximum current density is almost equal in both

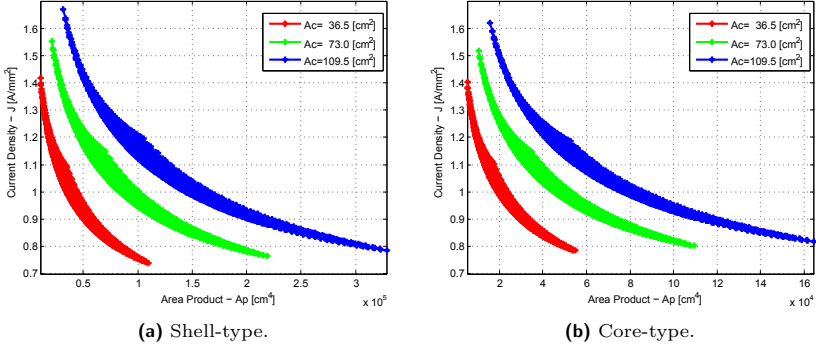


Figure 3.5: Current density vs area product. Possible transformer configurations with $D = 146$ mm and $A=[25$ mm (red), 50 mm (green), 75 mm (blue)]. Natural convection with $T_{amb} = 40$ °C, $T_{surface} = 100$ °C and $\varepsilon = 0.8$. Filling factor 0.2.

cases, but the shell-type transformer can reach higher power levels, the maximum permissible magnetic induction value will be higher too in the case of shell-type transformers.

One way to increase maximum current density, is the redistribution of power losses. Increasing the winding-loss ratio from $1/2$ to $2/3$, increases the maximum current density to 2 A/mm² for naturally cooled transformers. Another way to change maximum current density lies on the variation of the window area form. For the same surface, the maximum dissipation capability is reached with square surfaces. However, the core window variation is not possible within the manufacturers constructional limits.

The same analysis but with oil has been carried out (see Appendix B.2), where a maximum current density of 4 A/mm² is achieved. From this analysis, it can be concluded that for a naturally cooled transformer the maximum permissible current density is 2 A/mm², while in the case of forced cooled transformers this limit will be increased to 4 A/mm². This two maximum current density limits, depending on the chosen cooling system, will be introduced as optimization inputs.

3.2.7. Operating Frequency Range

With the right conductor size along with the optimal winding arrangements, detrimental frequency effects can be avoided in transformer windings. However, the maximum operating frequency of the medium-frequency power transformer will be limited by the chosen magnetic material.

Transformer core losses depend on the frequency of the applied flux waveform and on the maximum magnetic induction value (3.17). For explanatory and comparison purposes the values provided by the manufacturer for sinusoidal waveforms are used [METGLAS].

$$P_c = \left(K f^a B_m^b \right) V_c \tag{3.17}$$

with $K = 6.5$, $a = 1.51$ and $b = 1.74$, and V_c the volume of the core.

Once more an efficiency of 99%, equal loss distribution within transformer winding and magnetic core, and natural cooling is considered. The maximum core-loss capacity of iron-based amorphous cores in their Power System series will be limited to a (f, B_m) pair. The maximum operating frequency of possible shell-type and core-type transformers is illustrated in Fig. 3.6 and Fig. 3.7, respectively,

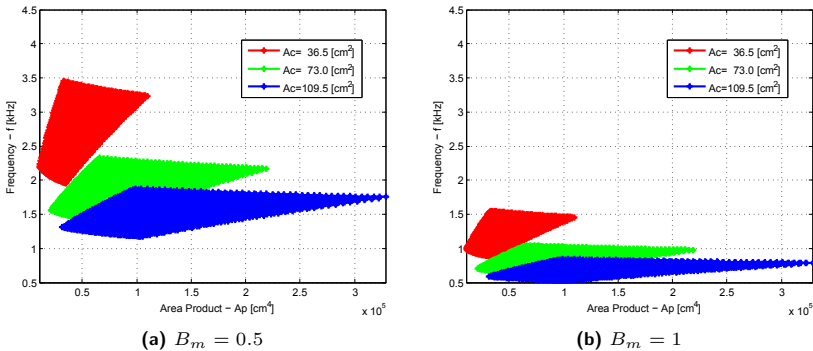


Figure 3.6: Operating frequency range for a shell-type transformer. Possible transformer configurations with $D = 146$ mm and $A=[25$ mm (red), 50 mm (green), 75 mm (blue)]. Natural convection with $T_{amb} = 40^\circ\text{C}$, $T_{surface} = 100^\circ\text{C}$ and $\varepsilon = 0.8$.

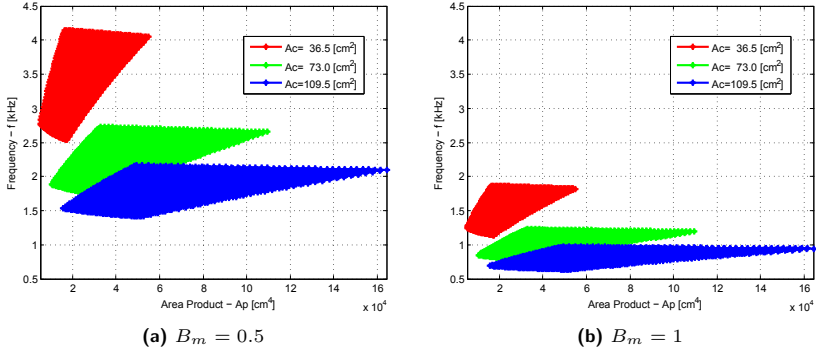


Figure 3.7: Operating frequency range for a core-type transformer. Possible transformer configurations with $D = 146$ mm and $A=[25$ mm (red), 50 mm (green), 75 mm (blue)]. Natural convection with $T_{amb} = 40$ °C, $T_{surface} = 100$ °C and $\varepsilon = 0.8$.

for two magnetic induction values.

Clearly, for smaller induction values higher frequencies can be reached (see Fig. 3.6a and Fig. 3.7a). Therefore, with these magnetic cores and considering natural cooling, a maximum operating frequency of 4 kHz can be reached (see Fig. 3.7a). In order to reach this frequency range, not only the magnetic core must be able to dissipate the heat, but also transformer configuration must be able to comply with the requirements of the chosen application, like maximum voltage or the required number of turns. Thus, these frequencies are the absolute maximums for each configured type of core.

In the case of forced cooling, like oil, the maximum frequency can be increased up to 12 kHz (see Appendix B.2). Thus, if resonant converters are considered for the application with higher frequencies, in order to control switching losses and reduce transformer size, the medium-frequency power transformer will require forced cooling, increasing inherently the final dimensions of the transformer.

3.2.8. Optimal Conductor Thickness

The optimization process receives an optimal conductor for each number of layers. The generation of this optimal wire table is based on the maximum current

density determined in the previous chapter, the current waveform through the transformer and the frequency-dependent winding-loss expressions introduced in subsection 2.2.2. The two different loss expressions for rectangular Litz bundles or solid conductors and for round Litz bundles have already been shown in subsection 2.2.2. This subsection will be divided in those two cases, too.

3.2.8.1. Rectangular Litz bundles or solid conductors

If the ac resistance of a foil (or equivalent foil conductor) depends on its thickness d and the number of winding layers m (see section 2.2.2.1), there will be an optimal value of d which makes the ac resistance minimum (see Fig. 3.8) for each number of layers.

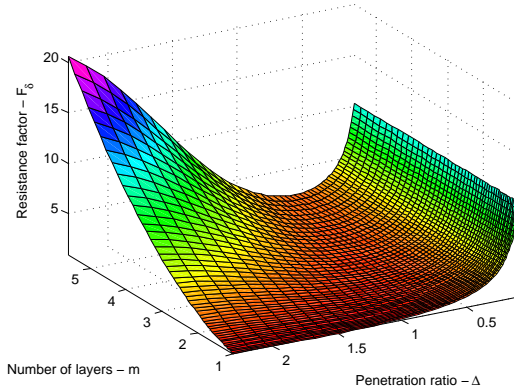


Figure 3.8: Resistance factor expression for various penetration ratios and number of layers.

Consider R_δ the dc resistance of a foil conductor with a δ_0 thickness, i.e. the fundamental skin depth.

$$R_\delta = \frac{d}{\delta_0} R_{dc} = \Delta R_{dc} \quad \Rightarrow \quad \frac{R_{ac}}{R_{dc}} = \Delta \frac{R_{ac}}{R_\delta} \quad (3.18)$$

For a sinusoidal current, the relationship becomes

$$F_\delta = \frac{R_{ac}}{R_\delta} = \left[\frac{\sinh(2\Delta) + \sin(2\Delta)}{\cosh(2\Delta) - \cos(2\Delta)} + \frac{2}{3} (m^2 - 1) \frac{\sinh(\Delta) - \sin(\Delta)}{\cosh(\Delta) + \cos(\Delta)} \right] \quad (3.19)$$

and the optimal thickness for each number of layers can be directly derived.

However, if the current through the transformer is non-sinusoidal, an iterative process will have to be carried out:

- First of all, the harmonic content of the waveform needs to be evaluated.
- In a second step the losses for each harmonic have to be determined.
- In a third step the total losses for each thickness will be established.
- And finally, in the last step, the minimum from the calculated data has to be found.

In order to avoid this long processus, a straightforward methodology is proposed in [Hurley et al., 2000], where the optimum layer thickness d_{opt} is defined from the optimal penetration ratio Δ_{opt} (3.20), which is determined with the rms values of the current and its derivative (3.21).

$$d_{opt} = \delta_0 \Delta_{opt} \quad \text{where} \quad \delta_0 = \sqrt{\frac{2}{\omega_0 \mu_0 \sigma}} \quad (3.20)$$

and

$$\Delta_{opt} = \frac{1}{\sqrt[4]{\Psi}} \sqrt{\frac{\omega I_n}{I_n'}} \quad \text{with} \quad \Psi = \frac{5m^2 - 1}{15} \quad (3.21)$$

However, instead of having foil conductors, if the winding is composed of round or rectangular Litz bundles, the optimal diameter is

$$d_{s_{opt}} = d_{opt} \sqrt{\frac{4}{\pi}} \quad (3.22)$$

It is important to notice that if the optimal penetration ratio turns to be ≥ 0.75 , the approximation introduced in the development is no longer valid, and an error of up to 50% can be obtained. The mathematical development, as well as, the source of the errors is developed in Appendix C.1.

In order to have a better understanding of the methodology, an example is presented. Thus, for example, in the case of resonant converters the current through the transformer is sinusoidal (3.23).

$$I_n = \frac{I}{\sqrt{2}} \quad \text{and} \quad I_n' = \frac{2\pi I}{T\sqrt{2}} \quad (3.23)$$

Then, according to (3.20) and (3.21) the optimal layer thickness versus the number of layers will be

$$d_{opt} = \delta_0 \frac{1}{\sqrt[4]{\Psi}} \tag{3.24}$$

If the layer is composed of round conductors, and using Dowell's porosity factor, the optimal round conductor diameter will be,

$$d_{s_{opt}} = \delta_0 \frac{1}{\sqrt[4]{\Psi}} \sqrt{\frac{4}{\pi}} \tag{3.25}$$

The optimal penetration ratio, as well as the optimal conductor diameter are illustrated in Fig. 3.9. As mentioned before, the optimal diameter value is not correct for a single layer winding, due to the fact that the optimal penetration ratio turns to be ≥ 0.75 . Thus, an iterative expression should be used.

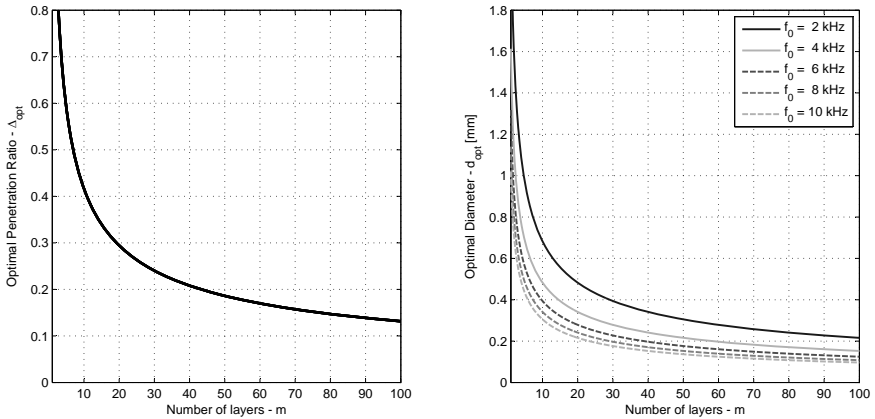


Figure 3.9: Optimal penetration ratio and optimal conductor diameter for sinusoidal waveforms.

However, usually in medium-voltage medium-frequency power transformers the winding will be composed of Litz wires, due to their high-power density. Therefore, even if the winding is composed of a single bundle layer, there will be several strand layers, improving the validity of the expression.

From the optimum conductor diameter and the maximum current density, a pre-selection of optimum conductors for each number of layers or range of layers

is derived, i.e. a wire look-up table. As every final conductor will not present the same effective conductive area, the current density will be reevaluated in the optimization process. Finally, with this look-up table, the area of the conductor will be determined (exact conductor geometry), generating a precise loss and leakage inductance estimation, and improving the optimization with real and final conductor sizes.

3.2.8.2. Round Litz bundles

In the case of round Litz wires another expression was highlighted as resistance factor expression

$$F_r = \frac{\gamma}{2} \left(\tau_1(\gamma) - \frac{\pi^2 n_s p_f}{24} \left(16 m^2 - 1 + \frac{24}{\pi^2} \right) \tau_2(\gamma) \right) \quad (3.26)$$

with $\gamma = \Delta/\sqrt{2}$. Contrary to the previous case, the resistance factor expression for round Litz wire windings does not only depend on the number of layers (see Fig. 3.10), but also on the number of strands (see Fig. 3.11). Therefore, there will be an optimal couple (n_s, m) which makes the ac resistance minimum.

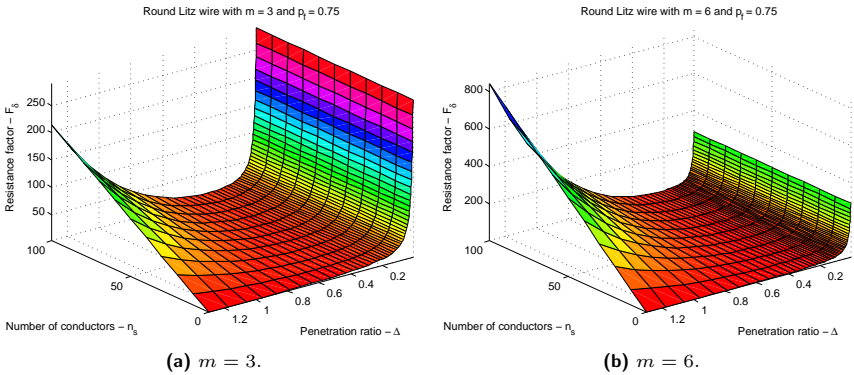


Figure 3.10: Resistance factor expression for various penetration ratios and number of strands, and for two number of layers.

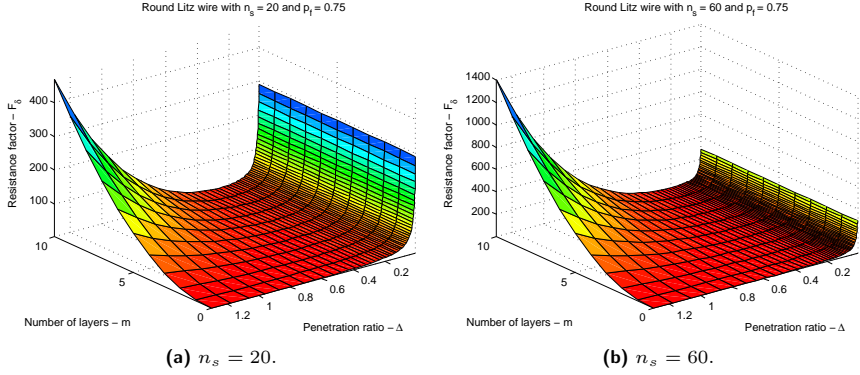


Figure 3.11: Resistance factor expression for various penetration ratios and number of layers, and for two number of strands.

The development for the optimal conductor diameter in the case of round Litz bundles is carried out in the same way as in [Hurley et al., 2000]. The skin and proximity effect factors, τ_1 and τ_2 respectively, are expanded and only the terms up to the order of γ^3 are used (3.27). In subsection 2.2.2.3 it has already been proven that the approximation is precise enough for small penetration ratios, the optimal penetration range according to Fig. 3.10 and Fig. 3.11 is then

$$F_r = 1 + \frac{\gamma^4}{192} \left(\frac{1}{6} + \frac{\pi^2 n_s p_f}{4} \left(16 m^2 - 1 + \frac{24}{\pi^2} \right) \right) \quad (3.27)$$

Rewriting (3.27) for easier manipulation turns into

$$F_r = 1 + \frac{\Psi}{3} \gamma^4 \quad (3.28)$$

where

$$\Psi = \frac{1}{64} \left(\frac{1}{6} + \frac{\pi^2 n_s p_f}{4} \left(16 m^2 - 1 + \frac{24}{\pi^2} \right) \right) \quad (3.29)$$

which has the same variables as in the case of the optimal foil thickness for rectangular Litz bundles and solid conductors [Hurley et al., 2000]. Therefore, the

optimal strand diameter is

$$d_{s_{opt}} = \delta_0 \frac{1}{\sqrt[4]{\Psi}} \sqrt{\frac{\omega I_{rms}}{I'_{rms}}} \tag{3.30}$$

thus

$$d_{s_{opt}} = \delta_0 \frac{4}{\sqrt[4]{\frac{1}{6} + \frac{\pi^2 n_s p_f}{4} \left(16 m^2 - 1 + \frac{24}{\pi^2}\right)}} \sqrt{\frac{\omega I_{rms}}{I'_{rms}}} \tag{3.31}$$

In this case a more exhaustive study has to be done in order to get the right set of conductors, because the optimal Litz strand diameter depends on both the number of strands, and on the number of layers. However, if the maximum current density is already known, the required number of strands is determined directly, and the number of layers can be optimized. In Fig. 3.12 the optimal penetration ratio for a sinusoidal excitation case is illustrated.

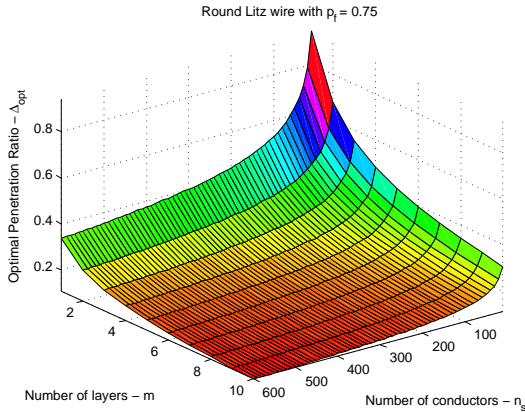


Figure 3.12: Optimal penetration ratio for sinusoidal waveforms, for various number of layers and strands.

3.3. Process: Parameterized Equations

Once the parameters of the transformer and the dimensional constraints are introduced, along with the wire look-up table, transformer equations are introduced

to begin with the optimization process (see flowchart of Fig. 3.1).

3.3.1. Number of turns

When designing a transformer, one of the main equations relates the induced voltage in the transformer to the number of turns in the winding, and the magnetic induction in the core. Supposing that the core has a high permeability value, and that the flux distribution within the core area is uniform, the previous relationship can be written as:

$$v(t) = N \frac{d\phi(t)}{dt} = N A_c \frac{dB(t)}{dt} \tag{3.32}$$

where ϕ is the magnetic flux.

One of the common characteristics of medium-frequency power transformers is their excitation by means of rectangular voltage waveforms (see Fig. 3.13), where

$$B_m = \frac{1}{2} \frac{V_{dc}}{N A_c} \left(\frac{T}{2} - T_0 \right) \quad \text{with} \quad T_0 = \Omega \frac{T}{2\pi} \tag{3.33}$$

and Ω is the length of the zero voltage period in radians.

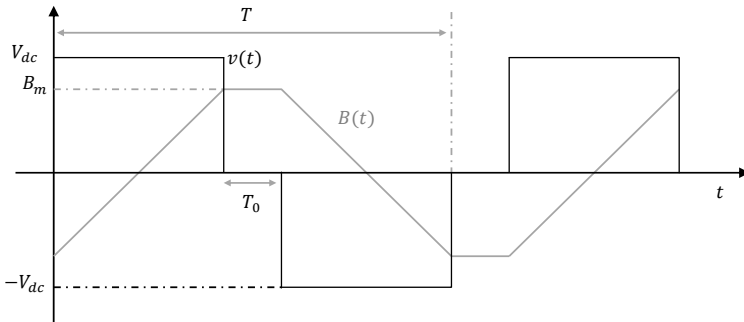


Figure 3.13: Rectangular voltage waveform and trapezoidal magnetic induction.

Therefore, the relationship between the winding turn number and the maximum magnetic induction turns to be (3.34).

$$N = \frac{V_{dc}}{4 f A_c B_m} D \tag{3.34}$$

where D is the duty ratio of the rectangular voltage waveform (3.35).

$$D = 1 - \frac{\Omega}{\pi} \quad (3.35)$$

Mention that iron-based amorphous alloys are made of micro-thin ribbons. In order to avoid eddy current effects within the core, isolation between ribbons is introduced, reducing the effective magnetic area (3.36). In the case of the AMDT cores, the lamination factor l_f is 0.84.

$$A_c = ADl_f \quad (3.36)$$

3.3.2. Winding Dimensions

In the case of the winding arrangement, two types of winding configurations have been considered (see Fig. 3.14): concentric and split windings. Interleaving is not considered in order to avoid voltage isolation problems, and high parasitic capacitance values [Prieto et al., 1998].

For concentric windings the height and the width of the whole winding are considered in the same direction, as in the case of the core window lengths (see Fig. 3.14a). However, in the case of the split winding the height is in the direction of the core window width, while the winding width is in the direction of the core window height (see Fig. 3.14b). This variation has been applied in order to correctly determine the leakage field within the core window area (see subsection 3.3.6). Besides directional differences, the number of layers is also considered in perpendicular directions.

Based on the number of turns and the number of layers, a conductor is selected from the look-up table, and then the winding height can be determined

$$\begin{aligned} \text{Concentric) } h_w &= \left\lfloor \frac{N}{m} + 1 \right\rfloor h_b \quad \text{or} \\ \text{Split) } h_w &= \left\lfloor \frac{N}{m} + 1 \right\rfloor d_b + \left\lfloor \frac{N}{m} - 1 \right\rfloor d_{intra} \end{aligned} \quad (3.37)$$

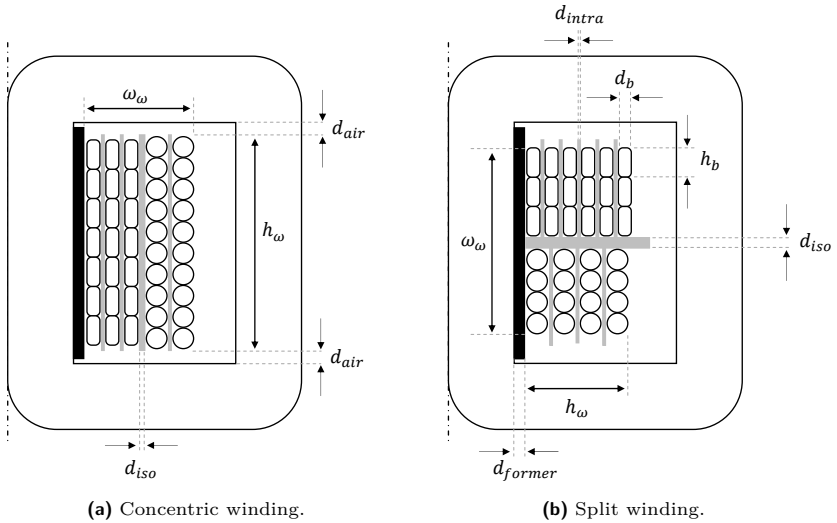


Figure 3.14: Winding configurations.

where h_b represents the height and d_b the width of the conductor or Litz bundle, and d_{intra} represents the isolation between layers, usually a Nomex [NOMEX] layer. The winding of the conductors forces the introduction of the intra-layer space in the same direction in both cases. Moreover, the turn-to-layer division is rounded downwards, and an additional winding turn is included due to the fact that the last winding turn has to be closed, too (see Fig. 3.15).

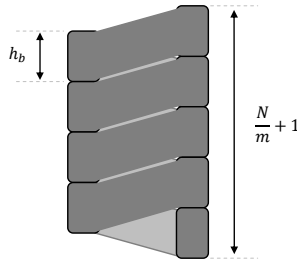


Figure 3.15: Winding total height, considering the ending loop of the last turn.

Like the winding height, the winding width will be

$$\text{Concentric) } w_w = 2 (m d_b + (m - 1) d_{intra}) + d_{iso} \quad \text{or} \quad (3.38)$$

$$\text{Split) } w_w = 2 m h_b + d_{iso}$$

The mean turn length of a winding can be approximated with

$$\text{Concentric) } l_w = \left[\left(\frac{A}{2} \right) N_C + d_{former} + \frac{w_w}{2} \right] 2\pi + 2D \quad \text{or} \quad (3.39)$$

$$\text{Split) } l_w = \left[\left(\frac{A}{2} \right) N_C + d_{former} + \frac{h_w}{2} \right] 2\pi + 2D$$

where N_C represents the number of cores, 1 for core-type and 2 for shell-type transformers (see Fig. 3.16). The isolation between the interior part of the winding and the core is represented with d_{former} . The width and height of the coil former are selected in order to comply with minimum clearance and creepage distances to the core. Although the winding in Fig. 3.16a is located on one of the core columns, the dimensions are exactly the same as in the configuration illustrated in Fig. 3.3a.

And finally, the winding volume will be

$$V_w = l_w h_w \quad (3.40)$$

3.3.3. Core Dimensions

Once the complete winding geometry is defined, core main dimensions can be determined (see Fig. 3.17). On the one hand, the core window width will be

$$\text{Concentric) } B = d_{former} + w_w + d_{air} \quad \text{or} \quad (3.41)$$

$$\text{Split) } B = d_{former} + h_w + d_{air}$$

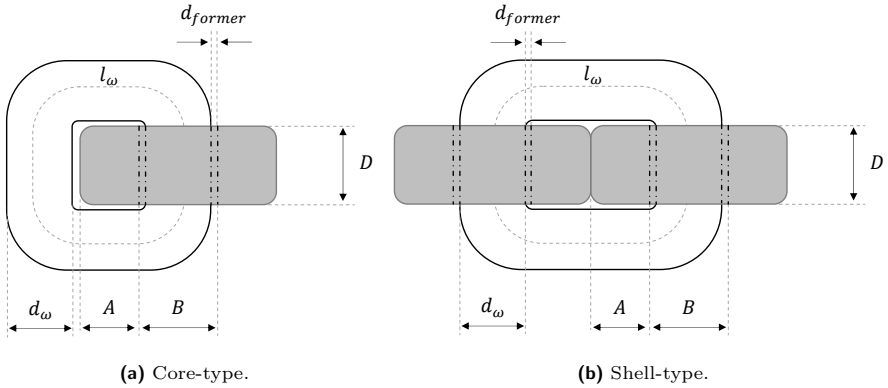


Figure 3.16: Winding length depending on transformer composition.

On the other hand, the core window height will be

$$\text{Concentric) } C = 2 d_{air} + h_w \quad \text{or} \quad (3.42)$$

$$\text{Split) } C = 2 d_{air} + w_w$$

where d_{air} represents the necessary clearance distance to the core.

With the core window dimensions, the external core geometry can be established directly

$$F = C + 2 A \quad \text{and} \quad E = B + 2 A \quad (3.43)$$

As well as, the core effective cross-sectional area

$$A_c = N_C A D l_f \quad (3.44)$$

and the mean core path

$$l_m = 2(B + D) + 4 A \quad (3.45)$$

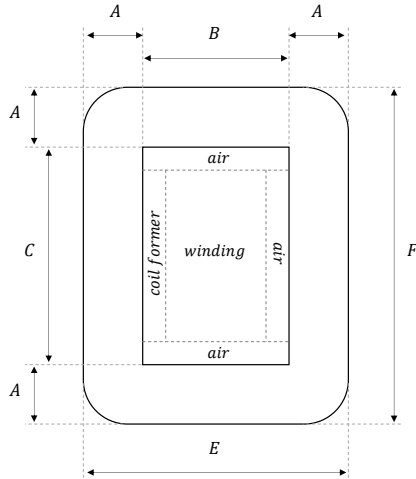


Figure 3.17: Core and winding arrangement, considering the clearance and creepage distances.

Finally, the core volume is determined.

$$V_c = A_c l_m \quad (3.46)$$

3.3.4. Core Losses

Once the dimensions of the transformer are established, the losses can be evaluated. As mentioned before, medium-voltage medium-frequency power transformers are usually excited with rectangular voltage waveforms [UNIFLEX]. In order to determine the losses, previously presented empirical loss-expressions for non-sinusoidal waveforms (see section 2.3.4) are extended to a rectangular waveform case. The proposed extended expressions are compared and the most suitable one is selected based on measurement results.

Like many other non-sinusoidal waveforms related with voltage conversion systems, the three-level voltage profile (see Fig. 3.13) can be accurately represented using a piecewise linear model (PWL). In the same way, for the description of the

magnetic induction profile this PWL model will be used (3.47).

$$B(t) = B_m \begin{cases} -1 + \frac{1}{TD} t & 0 < t < \frac{T}{2} - T_0 \\ 1 & \frac{T}{2} - T_0 < t < \frac{T}{2} \\ 1 - \frac{1}{TD} \left(t - \frac{T}{2} \right) & \frac{T}{2} < t < T - T_0 \\ -1 & T - T_0 < t < T \end{cases} \quad (3.47)$$

Applying this PWL model in the modified Steinmetz expressions introduced in subsection 3.3.4, some easy to use expressions are derived for the determination of magnetic core losses. The calculated expressions for each of the modified empirical core-loss evaluation methods along with the original Steinmetz equation are listed in Table 3.3.

Method	Expression
OSE	$K f^a B_{sq}^b D^b$
MSE	$(8/\pi^2)^{a-1} K f^a B_{sq}^b D^{b-a+1}$
IGSE	$2^{a+b} k_i f^a B_{sq}^b D^{b-a+1}$
WcSE	$\frac{\pi}{4} (1 + \Omega/\pi) K f^a B_{sq}^b D^b$
EEL	$\frac{C_{ba}}{C_{ab}} K f^a B_{sq}^b D^{b-a+1}$ <i>where</i> $C_{ba} = 4^a \frac{2}{\pi} \int_0^{\pi/2} \cos(\theta)^{b-a} d\theta$

Table 3.3: Core-loss expressions for rectangular voltage profiles.

B_{sq} refers to the peak induction value in a square waveform excitation case (3.48).

$$B_{sq} = \frac{T}{4} \frac{V_{dc}}{NA} \quad (3.48)$$

Careful attention must be paid to the equivalent elliptical loop method because the velocity of the ellipse angle from $-B_m$ to B_m and the frequency of the waveform

are not equal, and therefore a relative velocity has to be determined.

$$\theta = \frac{\pi}{T/2 - T_o} t \quad (3.49)$$

In magnetic materials the exponent of the magnetic induction b is higher than the exponent of the frequency a . Therefore, analyzing the equations listed in Table 3.3, it can be observed that the reduction of the duty ratio $D \rightarrow 0$ ($\Omega \rightarrow \pi$) provokes the decrease of the magnetic loss density (for the same dc voltage), due to the fact that the peak magnetic induction will also decrease. However, this downward behavior will be slightly counteracted with a higher influence of the waveform slope, except for the OSE, which only depends on frequency and peak magnetic induction. Fig. 3.18 presents an example of the behavior of a transformer made with an iron-based amorphous alloy core.

In order to choose the right empirical loss expression, and to verify the loss expression provided by the manufacturer for iron-based amorphous alloys, measurements on a transformer made with Power System cores have been carried out. The transformer was built for the UNIFLEX-PM project and is composed of two Power System cores (see Fig. 3.19). It has a rated power of 61.6 kVA, a frequency

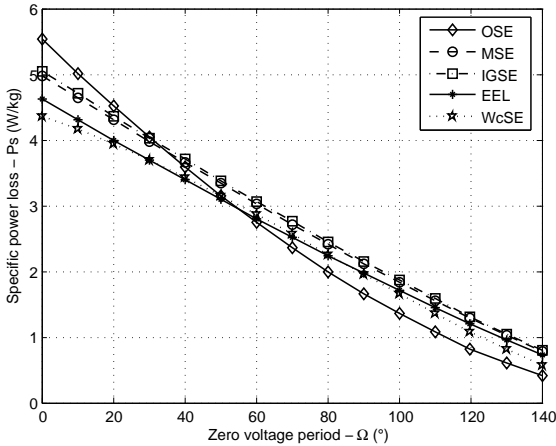


Figure 3.18: Loss method comparison for various rectangular voltage waveforms, with $f = 2$ kHz, $B_{sq} = 500$ mT, $K = 6.5$, $a = 1.51$ and $b = 1.74$. Theoretical results.

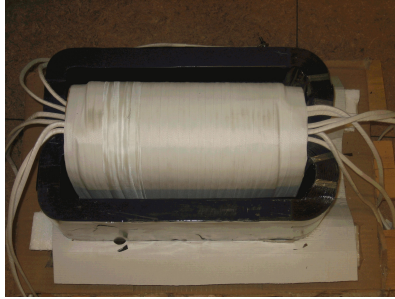


Figure 3.19: Transformer from the UNIFLEX-PM project, composed of two Power System cores.

of 2 kHz, a rated voltage of 1100 V and a turn ratio of 1.

The transformer makes part of a dc-ac converter. The primary of the transformer is excited with a H-bridge converter developed in the context of the UNIFLEX-PM European project [UNIFLEX, 2006]. The secondary of the transformer is open circuited. The current through the primary winding and the induced voltage in the secondary are measured (see Fig. 3.20a). The sampled waveforms are registered and transferred to a PC to calculate the magnetic field and the magnetic induction (see Fig. 3.20b) in the core. The surface of the magnetic characteristic of the material is measured to determine transformer core losses.

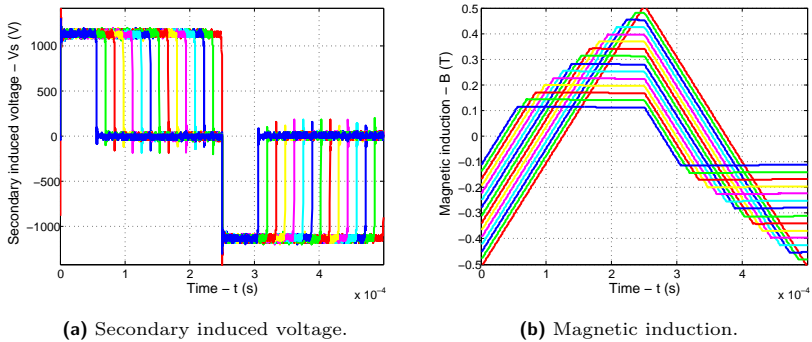


Figure 3.20: Measurements carried out in the UNIFLEX-PM project. Transformer built with two Power System cores.

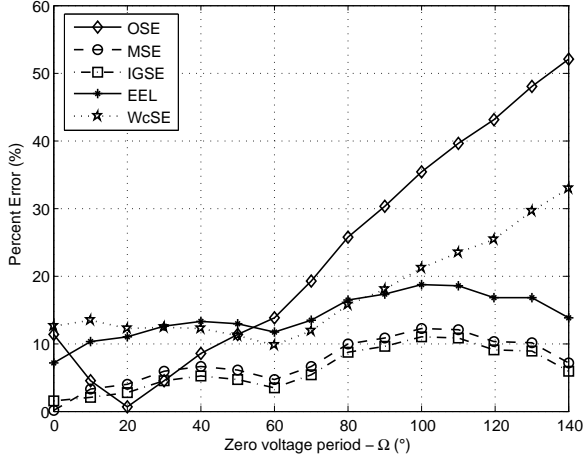


Figure 3.21: Measurement results for various rectangular voltage waveforms, with $f = 2$ kHz, $B_{sq} = 500$ mT, $K = 6.5$, $a = 1.51$ and $b = 1.74$.

In Fig. 3.21 the estimation error of each of the expressions summarized in Table 3.3 is illustrated. According to Fig. 3.21, the MSE and the IGSE show the best and almost identical estimation behavior. The EEL follows the same estimation behavior but with a higher estimation error. As it was mentioned in subsection 2.3.4, the MSE is not consistent with the OSE for sinusoidal waveforms, and therefore the IGSE will be the chosen expression. The expression has been rewritten to be directly applicable in the optimization algorithm (3.50).

$$P_c = 2^{a+b} k_i f^a B_m^b D^{1-a} \quad (3.50)$$

3.3.5. Winding Losses

Regarding winding losses, due to the linearity of copper, they are determined in a harmonic basis. Thus, first of all, the harmonic content of the current in the transformer has to be evaluated.

The penetration ratio for each of the harmonic components is

$$\Delta = \frac{d_s}{\delta} = d_s \sqrt{\pi f \nu \mu_0 \sigma} \quad (3.51)$$

From the penetration ratio, the resistance factor expression can be deduced (see section 2.2.2.1)

$$F_r = \Delta' \left[\zeta'_1 + \frac{2}{3} (m^2 - 1) \zeta'_2 \right] \quad (3.52)$$

with $\Delta' = \sqrt{\eta_w} \Delta$ and

$$\zeta'_1 = \frac{\sinh(2\Delta') + \sin(2\Delta')}{\cosh(2\Delta') - \cos(2\Delta')} \quad \text{and} \quad \zeta'_2 = \frac{\sinh(\Delta') - \sin(\Delta')}{\cosh(\Delta') + \cos(\Delta')} \quad (3.53)$$

where the correct porosity factor can be determined, as the conductors have been selected in a previous phase with their final geometry, and the required isolation has been introduced previously as a parameter of the optimization process.

From the geometry of the core, the primary and secondary mean length turn can be determined (3.54). In the case of concentric windings, the secondary is supposed to be inside the primary of the transformer (see Fig. 3.22).

$$\text{Concentric) } l_s = 2 N_C A + 8 d_{former} + 4 m d_c + 4 (m - 1) d_{intra} + 2 D \quad \text{and}$$

$$l_p = l_s + 8 m d_c + 8 (m - 1) d_{intra} + 8 d_{iso} + 2 D \quad \text{or}$$

$$\text{Split) } l_p = l_s = 2 N_C A + 8 d_{former} + 4 \left[\frac{N}{m} \right] d_c + 4 \left[\frac{N}{m} - 1 \right] d_{intra} + 2 D \quad (3.54)$$

Therefore, the resistance for each of the windings is

$$R_s = \frac{N l_s}{\sigma A_{cu}} \quad \text{and} \quad R_p = \frac{N l_p}{\sigma A_{cu}} \quad (3.55)$$

where the conductivity of copper is evaluated at surface temperature.

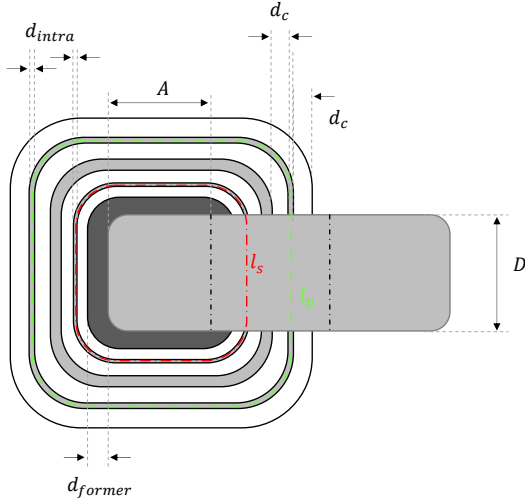


Figure 3.22: Primary and secondary winding length, considering the intra-layer and inter-winding isolation distances.

And finally the conduction losses will be $P_w = P_p + P_s$, that will be calculated for each current harmonic ν , and with their respective resistance factor expression.

$$P_s = \sum_{\nu=1}^n \left(\frac{I_\nu}{\sqrt{2}} \right)^2 F_{r_\nu} R_s \quad \text{and} \quad P_p = \sum_{\nu=1}^n \left(\frac{I_\nu}{\sqrt{2}} \right)^2 F_{r_\nu} R_p \quad (3.56)$$

3.3.6. Leakage Inductance

Finally the leakage inductance expression based on the generated geometry is introduced. The trapezoidal field distribution for the concentric winding is in the x direction, while in the case of split windings the same distribution can be found in the y direction (see Fig. 3.23)

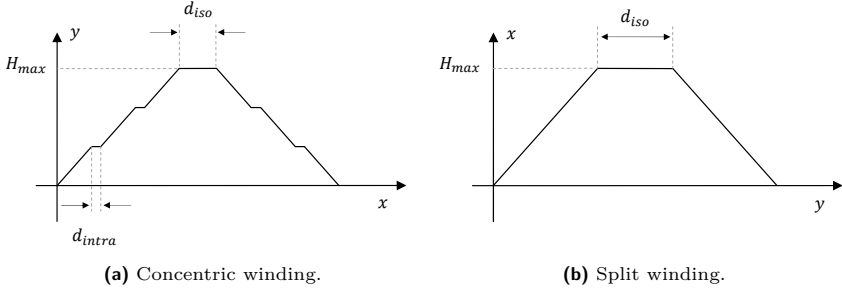


Figure 3.23: Magnetic field distribution within the considered winding structures.

Therefore, the leakage inductance is

$$\begin{aligned}
 \text{Concentric) } L_{\sigma} &= \mu N^2 \frac{l_w}{h_w} \left[d_c \frac{2m}{3} F_L + d_{iso} + d_{intra} \frac{(m-1)}{m} \right] \quad \text{or} \\
 \text{Split) } L_{\sigma} &= \mu N^2 \frac{l_w}{h_w} \left[d_c \frac{2m}{3} F_L + d_{iso} \right]
 \end{aligned} \tag{3.57}$$

where the leakage inductance factor will be

$$F_L' = \frac{1}{2m^2 \Delta'} \left[(4m^2 - 1) \varphi_1' - 2(m^2 - 1) \varphi_2' \right] \tag{3.58}$$

with $\Delta' = \sqrt{\eta_w} \Delta$ and

$$\varphi_1' = \frac{\sinh(2\Delta') - \sin(2\Delta')}{\cosh(2\Delta') - \cos(2\Delta')} \quad \text{and} \quad \varphi_2' = \frac{\sinh(\Delta') - \sin(\Delta')}{\cosh(\Delta') - \cos(\Delta')} \tag{3.59}$$

Once more the evaluation of the correct inductance factor expression is possible due to the initial winding geometry definition with actual conductor sizes. However, mention that the estimation of the leakage inductance value in a core-type transformer presents higher errors, due to the fact that the field trajectory on the external part of the winding is not exactly known, unless finite element simulations are carried out [Doebbelin et al., 2008].

3.4. Optimization: Minimization Functions

Optimization refers to choosing the best element from some set of available alternatives. In the simplest case, this means solving problems in which one seeks to minimize or maximize a real function by systematically choosing the values of real or integer variables from within an allowed set. More generally, it means finding "best available" values of some objective function given a defined domain, including a variety of different types of objective functions and different types of domains.

3.4.1. The Problem

Given a set X and a function $f : X \rightarrow \mathbb{R}$ (the objective or cost function), the objective is to find $x^* \in X$, that holds $f(x) \geq f(x^*)$ [Bonnans et al., 2006]. The variable x is usually known as the control variable.

We will consider only the case where X is a subset of \mathbb{R}^n , defined by constraints, i.e. given a number $m_I + m_E$ of functions $c_j : \mathbb{R}^n \rightarrow \mathbb{R}$ for $j = 1, \dots, m_I + m_E$, the problem is [Bonnans et al., 2006]

$$\begin{cases} \min f(x) & x \in \mathbb{R}^n \\ c_j(x) \leq 0 & j \in I \\ c_j(x) = 0 & j \in E \end{cases} \quad (3.60)$$

Here, I and E are two disjoint sets of integers, of cardinalities m_I and m_E , respectively [Bonnans et al., 2006]. We thus have m_I inequality constraints, indexed in I , and m_E equality constraints, indexed in E .

Transformer optimization problem has a set of inequality constraints m_I and the cost or objective function is formulated as a non-linear least-squares problem, therefore it is classified as a non-linear programming problem (NLP). There is no closed-form solution to a non-linear least-squares problem. Instead, numerical algorithms are used to find the value of the parameters which minimize the objective function. Most algorithms involve choosing initial values for the parameters. Then, the parameters are refined iteratively, i.e. the values are obtained by successive approximation.

The optimization problem is defined in MATLAB[®] and the non-linear least-squares solver, `lsqnonlin`, has been used to tune the leakage inductance value and minimize the transformer total losses. The general equation that describes the optimization problem is

$$\min_x \frac{1}{2} \|F(x)\|_2^2 = \frac{1}{2} \sum_i f_i(x)^2 \quad (3.61)$$

The solver starts at the point x_0 and finds a minimum of the sum of squares of the functions described in $F(x)$ (3.62), where the solution is always in the range $l_b \leq x \leq u_b$, lower and upper bounds, respectively.

$$\min_x \frac{1}{2} \|F(x)\|_2^2 = \frac{1}{2} \min_x (f_1(x)^2 + f_2(x)^2 + \dots + f_n(x)^2) \quad (3.62)$$

The optimization problem has bound constraints, for which MATLAB[®] uses the large-scale algorithm, a subspace trust-region method which is based on the interior-reflective Newton method. The large-scale algorithm does not solve underdetermined systems. Therefore, it requires that the number of equations within the objective function is at least as great as the number of variables x .

3.4.2. Objective or Cost Function

Throughout this methodology chapter several transformer characterization equations have been introduced. Within all these equations there are known parameters, pre-established parameters, dependent parameters and optimization variables.

- **Known parameters:** The rated power, the rated voltage, the operating frequency and the turns ratio, which are specific for each application.
- **Pre-established parameters:** The magnetic core, the maximum current density, conductor dimensions and the minimum isolation distances are pre-established values, derived from the known parameters and directly related to the application.

- **Dependent parameters:** The dependent parameters can be directly established from the known parameters, the pre-established parameters and the values of the optimization variables.
- **Optimization variables:** Variables adjusted within the optimization process to establish the dependent parameters.

The optimization variables in these case are the column width A , the maximum magnetic induction B_m and the number of layers m . With an initial guess on the column width and the maximum magnetic induction, and the pre-established number of cores N_c and depth of the core D , the number of turns is evaluated N . With the number of turns and with an initial guess on the number of layers, the winding geometry is determined, taking into account the pre-established minimum isolation distances d_{iso} and d_{intra} , and the selected winding composition. With the winding geometry and the pre-established creepage and clearance distances d_{air} , the minimum core window area is determined B and C . Using the initial column width guess, and the core window area dimensions, the core minimum dimensions are established. Once the core and winding dimensions are known, the losses are evaluated P_c and P_w , and the thermal limits verified. Finally, the resulting leakage inductance is determined L_σ . For each type of core and winding combination a different optimization process is carried out, unless initial design requirements pre-established a specific configuration.

There are three optimization variables, thus, three minimization functions need to be defined. The first one is the approximation to the desired leakage inductance value L_s .

$$f_1(A, B_m, m) = |L_s - L_\sigma| \quad (3.63)$$

The second one is the minimization of transformer total losses (3.64).

$$f_2(A, B_m, m) = P_w + P_c \quad (3.64)$$

And the third one equates winding and core losses, improving the efficiency of the transformer (see subsection 3.2.4).

$$f_3(A, B_m, m) = |P_w - P_c| \quad (3.65)$$

This three functions compose the cost or objective function (3.66).

$$F(A, B_m, m) = f_1(A, B_m, m)^2 + f_2(A, B_m, m)^2 + f_3(A, B_m, m)^2 \quad (3.66)$$

The expressions given above present different uncertainties, requiring specific weighting factors for each minimized function. In the case of the leakage inductance value, the estimation error is normalized to the desired leakage inductance value.

$$f_1(A, B_m, m) = \frac{|L_s - L_\sigma|}{L_s} \quad (3.67)$$

Similarly, the equal loss estimation error and the maximum loss are normalized to the expected loss density, calculated from the expected minimum efficiency. In the case of the maximum loss density, the normalization is done considering twice the loss density value.

$$f_2(A, B_m, m) = \frac{P_w + P_c}{2 P_d} \quad (3.68)$$

and

$$f_3(A, B_m, m) = \frac{|P_w - P_c|}{P_d} \quad (3.69)$$

3.5. Conclusions

In this third chapter a transformer design methodology has been thoroughly explained. The methodology is based on the initial selection of the optimal conductor, which minimizes the ratio between winding ac and dc losses. Once the best conductor is selected, the optimization process determines the best transformer dimensions that improve the efficiency of the transformer (equal core and winding-loss sharing), always keeping the target of the desired leakage inductance value. The selection of the optimal conductor is simple and straightforward, both for solid conductors and Litz wires. An expression for the optimal strand diameter for round Litz wires has been proposed, and verified.

Moreover, it has been shown that a current density higher than 1.75 A/mm² requires forced cooling, as well as, an operation frequency higher than 4 kHz in the standard forms of the AMDT cores.

Several empirical expressions for the characterization of non-sinusoidal core losses, fed with rectangular excitation voltages, have been proposed, which use only manufacturer provided data and are based on piecewise linear models. From measurement results and comparison tests the IGSE has shown the best estimation behavior.

Finally, the optimization process with the parameterized equations have been introduced. Two type of winding configurations have been characterized, with two type of cores. The key points of the optimization process have been introduced, with their respective characterization equations. And in the final section of this third chapter, the selected optimization algorithm along with the proposed cost or objective function have been shown.

4

Design and Experimental Verification of a Dedicated Medium-Frequency Power Transformer

Summary

The aim of the present chapter is the application of the proposed transformer-design methodology to a particular case study: an indirect-conversion structure developed in the Industrial Electronics Laboratory for the UNIFLEX-PM project. First of all, the case study is presented and transformer constraints are analyzed. Briefly, the main design steps are described. Then, the prototype, along with the measurement set-up is introduced. Finally, the measurement results are analyzed, compared and verified.

4.1. Context

Between 2006-2009 the Industrial Electronics Laboratory (LEI) has been involved in the European Research Project of the 6th Framework Program called UNIFLEX-PM [UNIFLEX], aimed at studying the use of medium-frequency conversion systems in the medium-voltage distribution grids (10 kV-20 kV).

The UNIFLEX-PM project deals with a three-phase power electronics structure, which is able to control the transfer of energy between different grids with medium-frequency isolation modules (converter cells).

A schematic of a possible three-port structure is illustrated in Fig. 4.1, where three different networks can be interconnected, showing the flexibility and modularity of the UNIFLEX-PM proposal. The proposed conversion system is based on a cascaded structure where individually isolated modules are connected in series to reach the desired medium-voltage level for different and various medium-voltage grids.

The main role of the Industrial Electronics Laboratory in the project was to define the best solution for the conversion cells represented in Fig. 4.1, choosing among different existing bidirectional isolated dc-dc and ac-dc converters [Siemaszko et al., 2009], i.e. between direct and indirect-conversion structures. The compared conversion structures are shown in Fig. 4.2. On the one hand, the direct-conversion structure studies the behavior of a cycloconverter (see Fig. 4.2b) which is directly connected to the grid on one side, and to the medium-frequency power transformer on the other side, while the secondary of the transformer is connected to a rectifier. On the other hand, the indirect-conversion structure (see Fig.

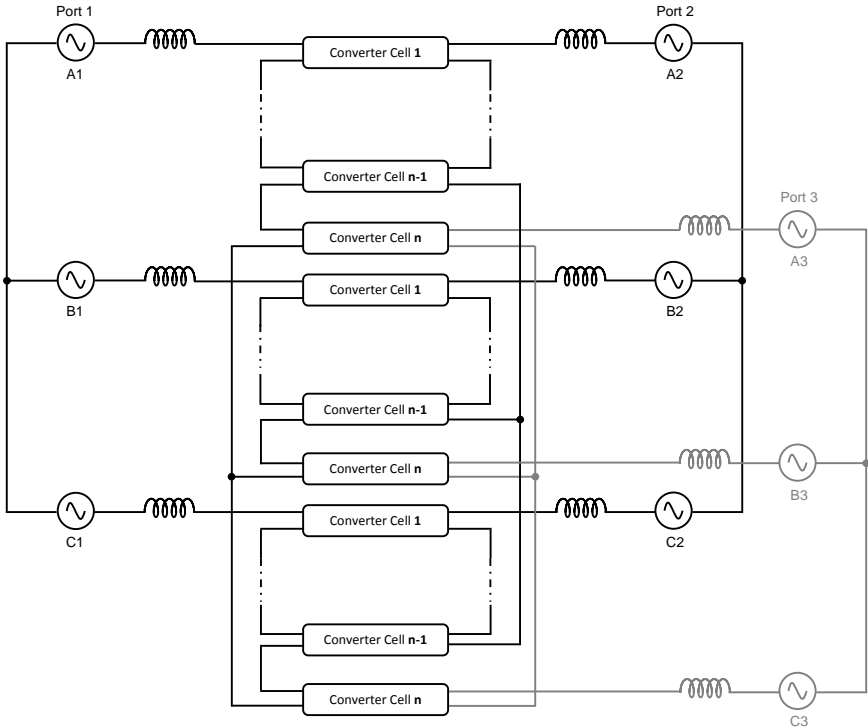


Figure 4.1: Three-port structure proposal on the UNIFLEX-PM European Project.

4.2a) is composed of a rectifier, a dc-link, an inverter connected to the medium-frequency power transformer and once more a rectifier connected to the secondary of the transformer.

Between the two structures the efficiency of the indirect conversion was found to be higher [Siemaszko et al., 2009]. Apparently, the innate characteristics of the isolated dc-dc converter present lower commutation losses and do not need any clamping circuit. On the contrary, the operation principle of the cycloconverter depends strongly on the parasitic inductances and capacitances of the transformer, creating undesired over-voltages, and requiring auxiliary circuits to restrict them. Therefore the indirect-conversion structure was the chosen one for the global cascaded system [UNIFLEX].

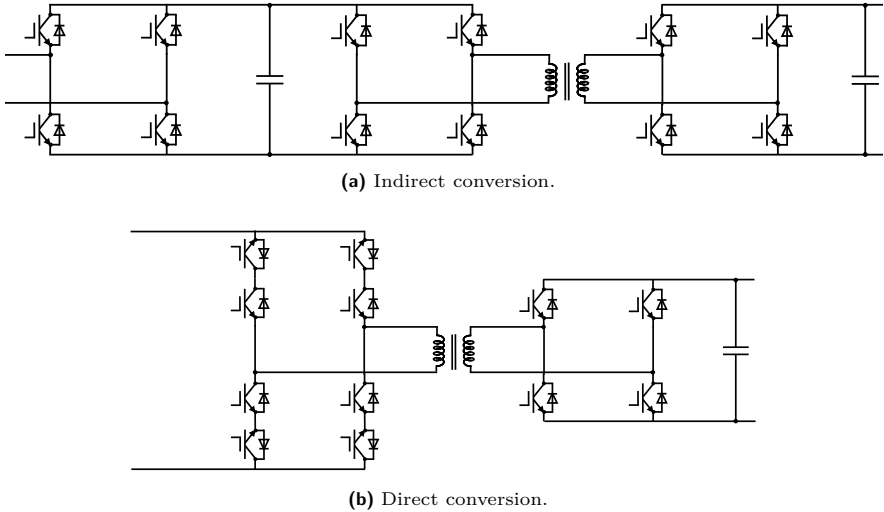


Figure 4.2: Medium-frequency individual conversion cell structures compared within the UNIFLEX-PM project.

In order to validate the proposed medium-frequency conversion system, a reduced-scale prototype has been built in the context of the UNIFLEX-PM European project. The reduced-scale prototype is intended to connect two 3.3kV three-phase ports. The schematic of the reduced-scale conversion system is illustrated in Fig. 4.3. The reduced-scale prototype includes the interconnection of four conversion modules per-phase. In the Industrial Electronics Laboratory the two conversion cells or possible isolation modules were built, tested and compared, along with the medium-frequency power transformers, which were made by ABB Sécheron. Once the indirect-conversion structure was selected the Industrial Electronics Laboratory built the other fifteen modules for the complete conversion system, which is currently in the final testing period in Nottingham.

Although the transformers for the conversion system were already built, in order to verify the methodology introduced in the previous chapter, a medium-frequency power transformer has been designed and built keeping the same requirements. The characteristics of the conversion system and the individual modules

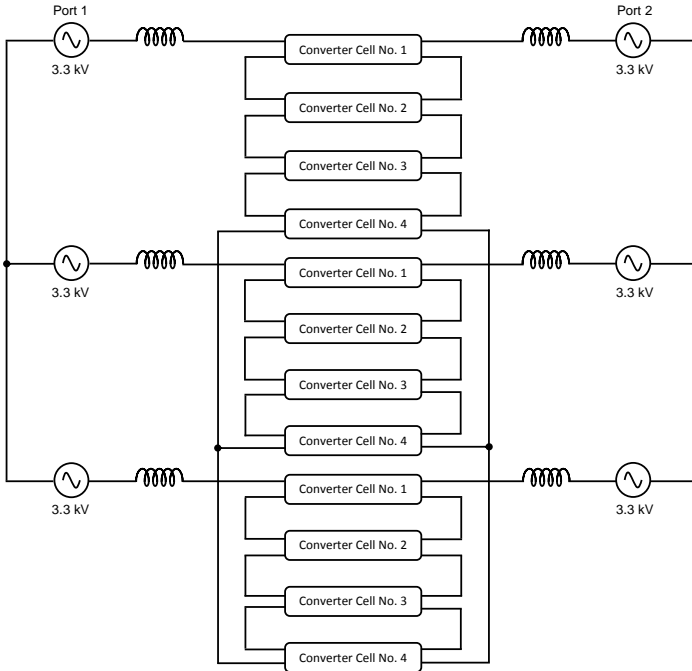


Figure 4.3: Two-port reduced-scale conversion system.

are summarized in Table 4.1.

Total Rated Power	P_{tot}	300	[kW]
AC Grid Voltages	$U_{a,b,c}$	3.3	[kV]
Module Rated Power	P_n	25	[kW]
DC Link Voltages	U_{dc1}, U_{dc2}	1.1	[kV]
Transformer Rated Power	S_n	36.3	[kVA]
Transformer RMS Current	I_n	33	[A]
Switching Frequency	f	2	[kHz]
Transformer Ratio	n	1:1	

Table 4.1: Main parameters of the reduced-scale prototype and the indirect-conversion structure.

4.2. Operation Principle of the Dual Active Bridge (DAB)

The core element of the indirect-conversion system within the UNIFLEX-PM project is the bidirectional isolated dc-dc converter or Dual Active Bridge (see Fig. 4.4). The DAB was first introduced in [de Doncker et al., 1988] where the three-phase structure was proposed for high-power applications.

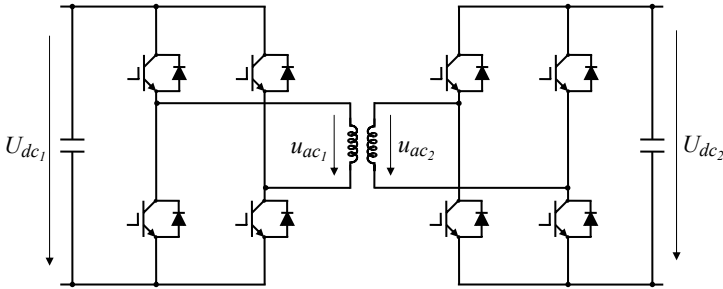


Figure 4.4: Bidirectional isolated dc-dc converter, the Dual Active Bridge (DAB).

The working principle lies in the phase-shift, γ , introduced between the rectangular voltages generated by the two bridges. If the two voltages u_{ac1} and u_{ac2} are exactly the same, there is no power transfer. However, as soon as a phase-shift is introduced between them, an ac current is generated, i_{ac} . This current will depend on the voltage difference, as well as, on the stray inductance, L_σ , of the medium-frequency power transformer.

Supposing that the winding resistance of the transformer is smaller than its leakage inductance and that the magnetizing inductance is much larger, the simplified schematic of Fig. 4.5 can be used to represent the operation principle of the Dual Active Bridge.

Each converter is able to generate a positive, a negative and a zero voltage, but usually a rectangular voltage waveform with no zero voltages and with a 50% duty cycle is used (see Fig. 4.6).

From the phasor representation, and using geometric relationships, the active

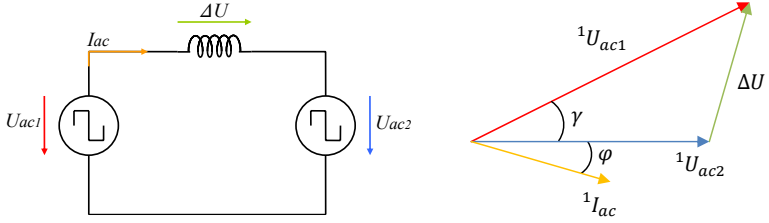


Figure 4.5: Equivalent operation principle schema of the DAB and phasor representation for the first harmonic.

and reactive powers are

$$P_2 = \frac{{}^1U_{ac1} {}^1U_{ac2} \sin(\gamma)}{L_\sigma \omega} = \frac{4U_{dc1} U_{dc2} \sin(\gamma)}{L_\sigma \pi^3 f} \quad (4.1)$$

$$Q_2 = \frac{{}^1U_{ac2} ({}^1U_{ac1} \cos(\gamma) - {}^1U_{ac2})}{L_\sigma \omega} = \frac{4U_{dc2} (U_{dc1} \cos(\gamma) - U_{dc2})}{L_\sigma \pi^3 f}$$

where

$${}^1U_{ac1} = U_{dc1} \frac{2\sqrt{2}}{\pi} \quad \text{and} \quad {}^1U_{ac2} = U_{dc2} \frac{2\sqrt{2}}{\pi} \quad (4.2)$$

It can be concluded, that high active power transfer implies also a high reactive

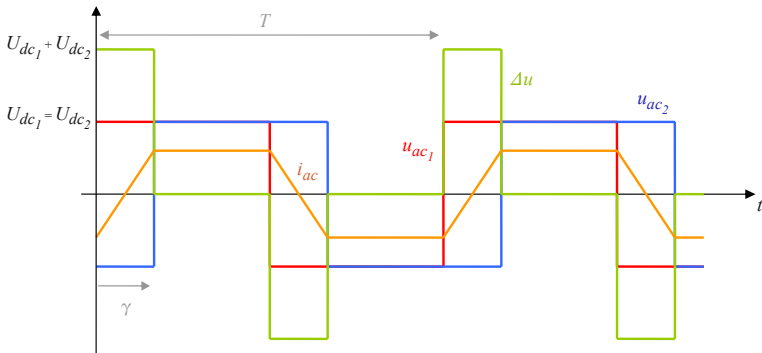


Figure 4.6: Voltage and current waveforms in the converter and transformer when both dc voltages are equal.

power circulation, and therefore, it is necessary to operate the dc-dc converter with low phase-shift values in order to limit this reactive power circulation.

4.3. Application Characteristics and Transformer Constraints

In the UNIFLEX-PM project, in order to take advantage of the benefits provided by the Dual Active Bridge and to reduce the circulating reactive power, the voltage difference between the dc sides was limited to 100 V and the phase-shift variation to the soft-switching range. This range is widely analyzed in [Schibli, 2000], and fulfills (4.3) in the case of rectangular modulation control.

$$\gamma < \frac{\pi}{2} \left(1 - \frac{U_{dc1}}{U_{dc2}} \right) \quad (4.3)$$

If the converter is operating correctly and both ac-side bridges regulate both dc voltages to the same level, the converter will be operating in the soft-switching region within the whole phase-shift range. However, if the maximum voltage difference is taken into account, the worst case scenario will force a minimum phase-shift for soft-switching commutations (4.4).

$$\gamma < \frac{\pi}{2} \left(1 - \frac{1100}{1200} \right) = 0.1309 \text{ [rad]} = 7.5 \text{ [}^\circ\text{]} \quad (4.4)$$

Therefore, in order to assure a soft-switching scenario within the whole voltage range, the phase-shift between the bridges will have to reach at least 7.5° , which will determine the maximum circulating reactive power.

Once the maximum phase-shift has been established, the maximum power transfer will be limited by the leakage inductance of the transformer. Isolating the leakage inductance from (4.1), turns into

$$L_\sigma > \frac{4U_{dc1}U_{dc2}\sin(\gamma)}{P_2\pi^3f} \quad (4.5)$$

The minimum leakage inductance for a 25 kW-2 kHz (see Table 4.1) application will be

$$L_\sigma > \frac{4 \cdot 1100 \cdot 1200 \cdot \sin(0.1309)}{25 \cdot 10^3 \cdot \pi^3 \cdot 2 \cdot 10^3} = 444.5 \text{ [}\mu\text{H]} \quad (4.6)$$

The reactive power circulating in the converter, for the worst case scenario, will be

$$Q_2 = \frac{4 \cdot 1200 \cdot (1100 \cdot \cos(0.1309) - 1200)}{444.5 \cdot 10^{-6} \cdot \pi^3 \cdot 2 \cdot 10^3} = -Q_1 = -19 \text{ [kVAR]} \quad (4.7)$$

Thus, the transformer will be designed to withstand a minimum apparent power of

$$S_2 = \sqrt{P_2^2 + Q_2^2} = 31.4 \text{ [kVA]} \quad (4.8)$$

When the voltage difference between the dc links is the highest permissible one, the rms current through the transformer will be

$$I_n = 31.11 \text{ [A]} \quad (4.9)$$

Considering the constraints of the transformer, the leakage inductance has been established at $480 \mu\text{H}$. With the dc link voltage levels, the frequency of the waveform and the leakage inductance value, the circulating power depending on the phase-shift is illustrated in Fig. 4.7, for different and equal voltage levels. With higher voltage differences, the ratio between active and reactive power reduces, carrying a high reactive power circulation for almost equal active power levels.

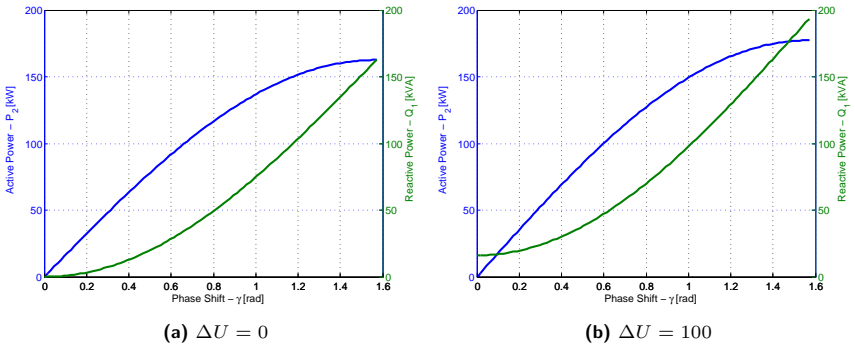


Figure 4.7: Active and reactive power for various phase-shifts with $L_\sigma = 480 \mu\text{H}$, $f = 2 \text{ kHz}$, $U_{dc1} = 1100$ and **(a)** $U_{dc2} = 1100$ or **(b)** $U_{dc2} = 1200$.

Thus, the medium-frequency transformer has been designed using the values already introduced in Table 4.1 and the characteristics calculated above. In addition, the transformer must be able to withstand the total grid voltage, 3.3 kV, as the transformers within a grid phase will be part of a multilevel structure.

4.4. Medium-Power Amorphous Cores

Even if the ultimate goal of the UNIFLEX-PM project is the development of medium-frequency conversion systems for medium-voltage applications (10 kV-20 kV), the first prototype has been designed for a 3.3 kV grid, with medium-frequency isolated modules of 25 kW.

The isolated dc-dc converter demands a high-leakage inductance value. For the same winding configuration, the leakage inductance of core-type transformers is slightly higher, due to external leakage fields. However, the value of the leakage inductance and the trajectory of the magnetic field are more easily controlled in shell-type transformers, because the magnetic field trajectory closes using the core path. Thus, a shell-type transformer will be considered.

For a 25 kW module, and expecting an efficiency of the transformer of at least %99, transformer losses will be at most 250 W. In the previous chapter the loss dissipation capabilities of iron-based amorphous alloys in the Power Systems series were analyzed. In the case of shell-type transformers, the smallest of these cores was capable of handling a power of 40 kW, and therefore this kind of cores will be over dimensioned for an application of 25 kW, and lower power structures made with the same material and by the same manufacturer are chosen. The manufacturer of the Power System series offers some amorphous rectangular forms (Powerlite) which can be built in any desired form following some constructional limits [METGLAS]. The information provided by the manufacturer, as well as the geometry of these magnetic bars, is illustrated in Table 4.2. The use of these forms allows the application of the proposed design methodology, due to the fact that the core dimensions can be determined in the optimization process, and because the optimization is not forced to select a pre-established standard core.

The loss curve of these expressions is the same as that of the Power System series cores (iron-based amorphous alloy, 2605SA1). It should be mentioned that

Powerlite Forms			
	Minimum	Maximum	Tolerance
Length	50 mm	300 mm	± 0.5 mm
Width	20 mm	50 mm	± 0.5 mm
Height	10 mm	100 mm	± 0.2 mm

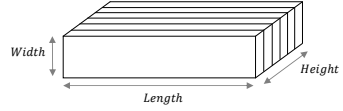


Table 4.2: Powerlite form dimensions, made of iron-based amorphous alloy 2605SA1 ribbons or laminations.

these forms are recommended for magnetic devices working below 20 kHz and for powers up to 500 kW.

Once the magnetic material has been chosen, the optimal conductors for various number of layers will be selected.

4.5. Conductor Selection

In order to select the right conductor for the transformer winding, the optimal layer thickness expression will be used. Thus, to apply the optimal conductor thickness expression (see subsection 3.2.8), the current through the transformer has to be established first, considering the working principle of the converter. In the case of the DAB, the current and its derivative for soft-switching cases are represented in Fig. 4.8, where

$$I_{ac2} = \frac{U_{dc2} \pi + U_{dc1} (2 \gamma - \pi)}{4 \pi f L_{\sigma}}, \quad I_{ac1} = \frac{U_{dc1} \pi + U_{dc2} (2 \gamma - \pi)}{4 \pi f L_{\sigma}} \quad (4.10)$$

First of all, the rms value expression for the current waveform is derived (4.11).

$$I_n = \sqrt{\frac{2}{T} \left(\int_0^{T/2-t_d} \left(\frac{I_{ac1} - I_{ac2}}{T/2 - t_d} \right)^2 dt + \int_0^{t_d} \left(\frac{I_{ac1} + I_{ac2}}{t_d} \right)^2 dt \right)} \quad (4.11)$$

where $t_d = \gamma/\omega$ with $\omega = 2\pi/T$, which turns into

$$I_n = \frac{\sqrt{3}}{12 \pi f L_{\sigma}} \sqrt{(U_{dc1} - U_{dc2})^2 \pi^2 + 4 U_{dc1} U_{dc2} \gamma^2 \left(3 - \frac{2\gamma}{\pi} \right)} \quad (4.12)$$

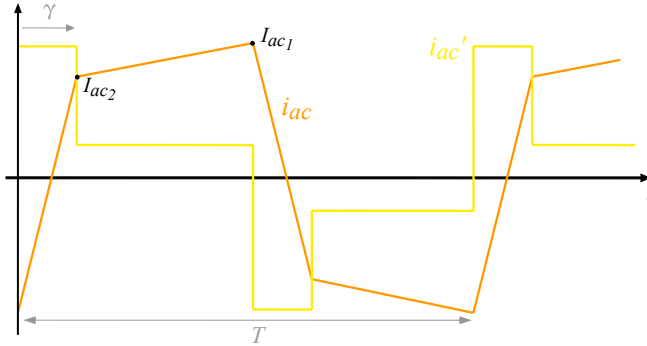


Figure 4.8: Current through the transformer and its derivative

Secondly, the rms value of the derivative of the current is determined (4.13).

$$I_n' = \frac{1}{L\sigma} \sqrt{(U_{dc1} - U_{dc2})^2 + 4 U_{dc1} U_{dc2} \frac{\gamma}{\pi}} \quad (4.13)$$

In an initial analysis the possibility of using solid conductors will be studied. Therefore, once both current expressions are established, they are introduced in (3.20) from subsection 3.2.8, from where the optimal foil thickness is determined (4.14).

$$d_{opt} = \delta_0 \sqrt[4]{\frac{(U_{dc1} - U_{dc2})^2 \pi^3 + 4 U_{dc1} U_{dc2} \gamma^2 (3\pi - 2\gamma)}{12 \Psi ((U_{dc1} - U_{dc2})^2 \pi + 4 U_{dc1} U_{dc2} \gamma)}} \quad (4.14)$$

If the winding is composed of round conductors, or rectangular Litz bundles, the optimal diameter for these cases will be,

$$d_{s_{opt}} = \delta_0 d_{opt} \quad (4.15)$$

If both dc voltages are equal the expression for the optimal diameter (4.15), is reduced to

$$d_{s_{opt}} = \delta_0 \sqrt[4]{\frac{\gamma (3\pi - 2\gamma)}{12 \Psi}} \sqrt{\frac{4}{\pi}} \quad (4.16)$$

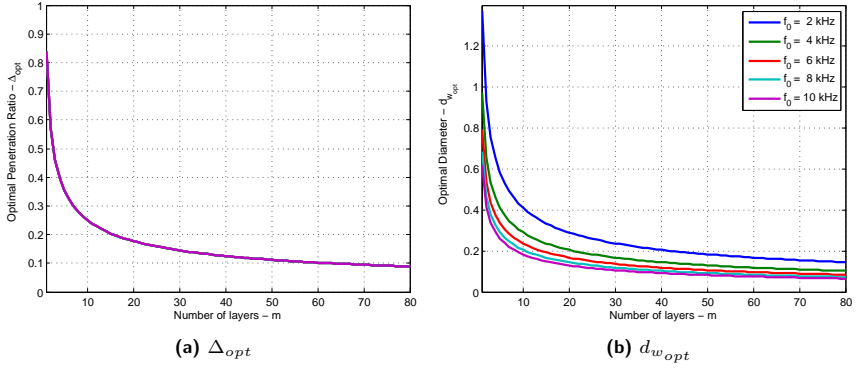


Figure 4.9: Optimal conductor diameter for various layers and frequencies, with $\gamma = 0.1309$ and $U_{dc1} = 1200$, $U_{dc2} = 1100$. Worst case scenario.

The optimal conductor diameter is illustrated in Fig. 4.9b for various number of layers and frequencies. It can be observed that the penetration ratio for low number of layers is > 0.75 (see Fig. 4.9a). This equation is not valid for one and two layer windings (there is an estimation error of %40 as shown in Appendix C.1), and thus, the traditional iterative method has been used for low number of layers. The result to this study shows that the optimal conductor thickness for a single layer winding will be 2.25 mm, and 1.25 mm for a two layer winding (see Appendix C.1). Supposing that the transformer is composed of a single layer, the required height for a rectangular conductor, for example, in the case of a dry-type transformer, will be

$$h_b = \frac{I_n}{J_{max} \cdot d_{s_{opt}}} = \frac{33}{1.75 \cdot 2.25} \simeq 8.3 \text{ [mm]} \quad (4.17)$$

Besides large conductors for single layer windings, the transformer needs a considerable leakage inductance value, i.e. a high number of turns will be necessary. Therefore, the core window height for such large conductors will be unacceptable, $C \simeq N h_b$. In order to face this problem, more layers will be necessary with smaller optimal conductors, prohibiting the utilization of solid conductors. Moreover, mention that too high conductors in transformer winding edges create additional losses and hot spots due to tangential magnetic fields.

If solid conductors are disregarded the only solution within this frequency range and current density values is the utilization of Litz wires. Looking at the curves illustrated in Fig. 4.9b, three Litz standard strand diameters have been considered: 0.355 mm, 0.20 mm and 0.1 mm, although other Litz strand diameters and compositions can be manufactured on demand, these three possible conductors cover widely the result illustrated in Fig. 4.9b.

The knowledge of the actual conductor geometry (height, width, number of strands and filling factor) is the key point within this optimization methodology, because not only the dc and ac loss within the winding will be minimized, but also the correct expressions will be applied in the optimization process. Moreover, if optimization processes are carried out with solid conductor suppositions and using Dowell’s equation, the final optimized design will be far from the final winding geometry, i.e. winding geometry is completely changed if solid conductors or Litz wires are used, and so do the winding-loss behavior and the leakage inductance value.

Litz wires can form rectangular or round bundles. In this case, and in order to increase the utilization factor of the core window, rectangular Litz bundles have been chosen. From the rectangular Litz wire table, the Litz wire bundle compositions illustrated in Fig. 4.3 have been selected.

Litz Wire	180 x 0.355	600 x 0.2	2205 x 0.1
Strand Diameter	0,355 mm	0,2 mm	0,1 mm
Number of Strands	180	600	2205
Effective Surface	18.37 mm ²	18.85 mm ²	17.56 mm ²
Current Density	1.79 A/mm ²	1.75 A/mm ²	1.88 A/mm ²

Table 4.3: Selected rectangular Litz bundles.

Once the winding possible conductors are chosen, the equations for the optimization process can be established. The procedure follows the steps extensively introduced in Chapter 3. The only missing point, is the evaluation of copper losses, which are specific for each converter application.

4.6. Winding Losses for the DAB

The determination of the specific loss behavior is essential for the optimal design process. Therefore, considering the linear behavior of copper, conduction losses can be established in an harmonic basis. The voltages on both sides of the medium-frequency transformer can be represented using their Fourier series,

$$u_{ac1}(t) = \sum_{\nu=1}^{\infty} \nu U_{ac1} \sin(\nu(\omega t + \gamma))$$

$$u_{ac2}(t) = \sum_{\nu=1}^{\infty} \nu U_{ac2} \sin(\nu \omega t)$$
(4.18)

where γ is the phase-shift between the bridges and the amplitudes of the ν^{th} harmonics are

$$U_{ac1} = U_{dc1} \frac{2}{\nu \pi} (1 - \cos(\nu \pi))$$
(4.19)

$$U_{ac2} = U_{dc2} \frac{2}{\nu \pi} (1 - \cos(\nu \pi))$$

As it can be observed, the odd harmonics on both sides of the transformer are zero. Once the excitation voltages are established, the voltage difference in the ac link is stated

$$\Delta u(t) = \sum_{\nu=1}^{\infty} \nu \Delta U \cos(\nu \omega t + \varphi_{\Delta})$$
(4.20)

with the amplitude of the ν^{th} harmonic as

$$\Delta U = \sqrt{U_{ac1}^2 + U_{ac2}^2 - 2 U_{ac1} U_{ac2} \cos(\nu \gamma)}$$
(4.21)

and the phase as

$$\varphi_{\Delta} = \arctan \left(\frac{U_{ac1} \sin(\nu \gamma)}{U_{ac1} \cos(\nu \gamma) - U_{ac2}} \right)$$

$$- \frac{\pi}{2} \operatorname{sign} (U_{ac1} \cos(\nu \gamma) - U_{ac2})$$
(4.22)

Finally, the current in the medium-frequency transformer will be

$$i_{ac}(t) = \sum_{\nu=1}^{\infty} \nu I_{ac} \sin(\nu \omega t + \varphi_{\Delta}) \quad (4.23)$$

where the amplitude of the ν^{th} harmonic is defined with

$$I_{ac} = \frac{\Delta U}{2 \pi f \nu L_{\sigma}} \quad (4.24)$$

where L_{σ} is the value of the desired leakage inductance. The current harmonic content for the worst case scenario is illustrated in Fig. 4.10.

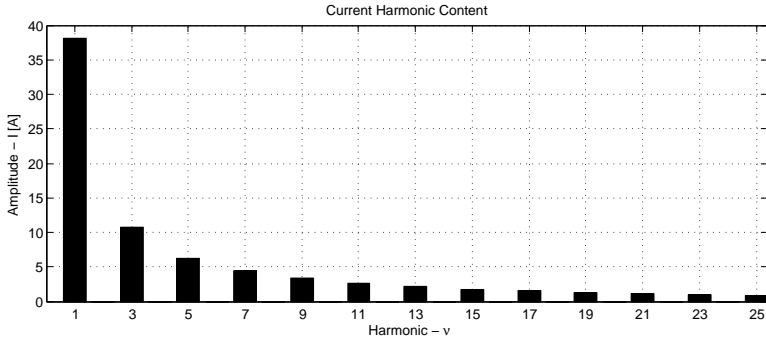


Figure 4.10: Amplitude of the current harmonics, for $f = 2$ kHz, $L_{\sigma} = 480 \mu$ H, $U_{dc1} = 1100$, $U_{dc2} = 1200$ and $\gamma = 0.1309$ rad.

The current presents only odd harmonics, which according to their amplitude have a strong influence on the transformer winding losses. Therefore, the selection of the optimal conductor diameter carried out in the previous subsection is essential to face this detrimental frequency effects, and optimize transformer final design.

Thus, in order to determine winding losses, the main current harmonic contents are evaluated, introduced in (3.56), and using the dimensions of the possible conductors, the resistance factor expression is derived. And finally, the total winding losses are evaluated.

4.7. Optimization Characteristics

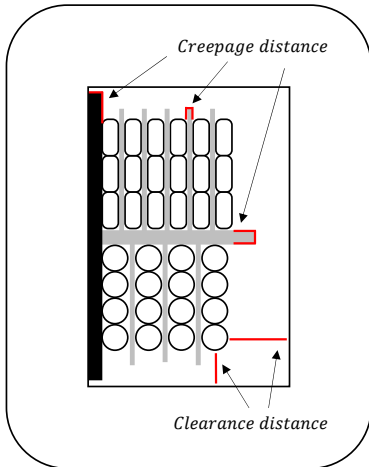
As mentioned before, a shell-type transformer has been selected for this case study. There are less unknown magnetic field trajectories outside the core, improving the estimation of the leakage inductance value and reducing parasitic fields in surrounding components. Moreover, a split winding has been selected. The application is bidirectional, and thus, a completely bidirectional transformer with symmetric behavior is proposed. In split windings, the dimension of both the primary and the secondary windings are equal, presenting equal dc resistances. However, in concentric windings with high-leakage inductances, the length difference between interior and exterior windings is considerable (3.54).

The transformer has to be able to withstand the 3.3 kV of one grid phase, therefore the minimum isolation voltage will be

$$U_{iso} = 2U_{max} + 1000 \simeq 8 \text{ [kV]} \quad (4.25)$$

In order to isolate this voltage levels the minimum creepage and clearance distances (500 V/mm) to the core have to be

$$d_{air} \geq \frac{3300}{500} = 6.6 \text{ [mm]} \quad \text{thus} \quad d_{air} = 7 \text{ [mm]}. \quad (4.26)$$



Regarding the intra-layer isolation, two NOMEX[®] sheets of 0.13 mm have been selected to be introduced between consecutive winding layers, which can hold rapid ac voltage rises of up to 27 kV/mm each one. The isolation between primary and secondary is reached using GPO-3 Glass polyester sheets, with a thickness of $d_{iso} = 5 \text{ mm}$, over dimensioned to tune the leakage inductance value. Moreover, the external part of the polyester sheet has to describe a creepage distance, i.e. air distance, of 7 mm. The coil former is also made with GPO-3 Glass

polyester sheets, and it has a thickness of $d_{former} = 6$ mm.

The Powerlite magnetic forms offer the possibility to vary transformer core geometry, almost as desired. In order to push the optimization further away, the window area limitations (tall rectangular form limitations) of the Power System series cores have been ignored, enabling free geometry generation.

Regarding the cost or objective function, for the first minimization function the expected leakage inductance value, as mentioned before, is $480 \mu\text{H}$. On the other hand, for the two other minimization functions the expected efficiency will be of at least 99%, equivalent to a maximum transformer loss value of 250 W.

4.8. MF Power Transformer Prototype

Even if a Powerlite form was selected for the transformer prototype, this kind of magnetic form was not commercially available in small quantities, and therefore several High Performance C-cores [METGLAS] made with the same iron-based amorphous alloy 2605SA1 have been used, exactly the AMCC-367S core (see Fig. 4.11). Fortunately, this core matched the designed geometry in a relatively correct manner.

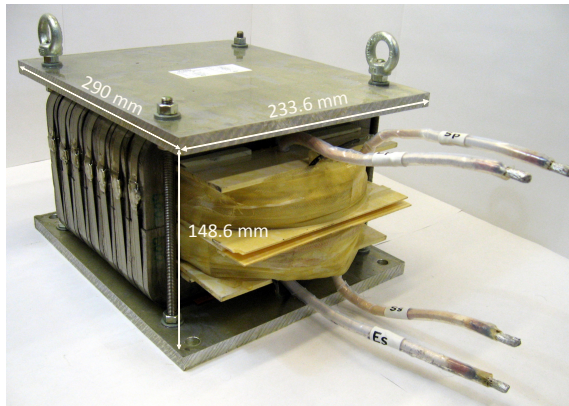


Figure 4.11: Image of the prototype transformer.

The final volume of the whole transformer is

$$V_t = 233.6[\text{mm}] \times 148.6[\text{mm}] \times 290[\text{mm}] \simeq 10 [\text{dm}^3] \quad (4.27)$$

with a power density of $2.5 \text{ kW}/\text{dm}^3$. Two sample prototypes of the transformer have been manufactured with the same geometry (one of them with a Black Backing Varnish which is used in highly restricted thermal environments). Moreover, the transformers have a fastening structure to help the heat dissipation and to facilitate transportation.

The AMCC-367S core presents the characteristics summarized in Table 4.4. The characteristics of the prototype transformer have been adjusted taking into account the dimensions of the AMCC-367S core. In the prototype transformer there are 14 AMCC-367S cores in two rows of 7 (see Fig. 4.11). This was the only available solution that matched the optimized core dimensions. Thus, the total core cross-sectional area is then $74.06 [\text{cm}^2]$.

A	B	C	D	l_m	A_c	A_w	A_p
25.8	67.0	97.8	25	43.78	5.29	63.81	340.1
[mm]	[mm]	[mm]	[mm]	[cm]	[cm ²]	[cm ²]	[cm ⁴]

Table 4.4: AMCC-367S core characteristics.

From the optimization process, and considering the expected leakage inductance value, a four layer winding has been manufactured. The primary and the secondary are composed of 38 Litz wire turns, made of 0.2 mm strands. The magnetizing inductance is determined with (4.28).

$$L_m = \frac{0.4 \pi N^2 A_c [\text{cm}^2] \cdot 10^{-8}}{l_{gap} [\text{cm}] + l_m [\text{cm}] / \mu_\Delta} = 14.3 [\text{mH}] \quad (4.28)$$

where $l_{gap} = 0.05$ is the minimum air gap and $\mu_\Delta = 1000$ is the incremental permeability in High Performance C-cores.

The maximum magnetic induction value in the optimization process turns always into a value around (4.29). As has been pointed out in subsection 3.2.7, for

naturally cooled transformers in order to increase operation frequency, the maximum magnetic induction must be kept in the low induction range. Thus, for an equal loss sharing strategy, with naturally cooled transformers working at 2 kHz, and built with iron-based amorphous alloys, the optimal maximum magnetic induction value is 0.5 T.

$$B_m = \frac{U_{dc}}{4 f N A_c} \simeq 488.6 \text{ [mT]} \quad (4.29)$$

Therefore, the expected transformer specific core losses will be

$$P_{c_s} = 2^{a+b} k_i f^a B_m^b = 4.83 \text{ [W/kg]} \quad (4.30)$$

with $k_i = 0.62$, for square voltage waveforms. Then the total core losses will be

$$P_{c_s} = P_{c_s} \rho_c V_c = 112 \text{ [W]} \quad (4.31)$$

with $\rho_c = 7.18 \text{ g/cm}^3$ [METGLAS].

The mean length of the winding is $l_w = 684 \text{ mm}$, and the total winding length more or less 26 m, with a 1.05 factor for strand twisting the final length turns into 27.3 m, which corresponds to a dc resistance of $27.4 \text{ m}\Omega$. Therefore, the ac resistance for various frequencies is represented in Fig. 4.12.

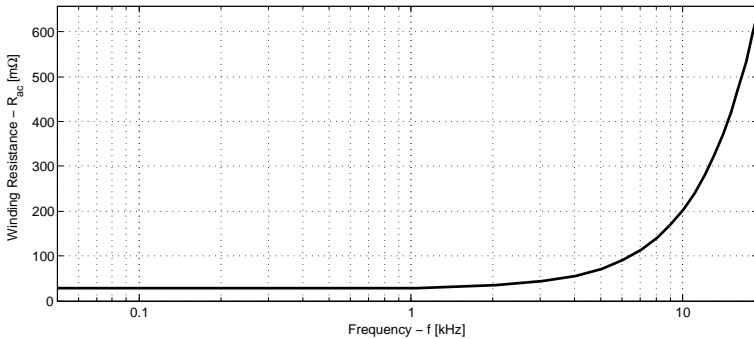


Figure 4.12: Expected winding resistance.

In order to determine winding losses, transformer current harmonics are evaluated, and along with the results illustrated in Fig. 4.12 they are combined in (3.56).

	Frequency [kHz]					
Operating Point	2	6	10	14	18	22
Nominal	30.37	10.06	5.97	4.19	3.18	2.53
Worst Case	38.10	10.7	6.29	4.39	3.33	2.64

Table 4.5: Transformer current harmonic content.

Instead of the worst case scenario, the nominal operating point will be used to determine transformer winding losses. So as to improve the efficiency of the transformer, winding nominal losses have to be equated with core constant losses. Therefore, summing up the main harmonic contents, winding losses turn into

$$P_p = 34.3 \cdot 30.37^2 + 90 \cdot 10^2 + 201.4 \cdot 6^2 + 368.4 \cdot 4.2^2 = 54.35 \text{ [W]} \quad (4.32)$$

Getting finally a total winding loss of $P_w = 2 P_p = 108.70 \text{ W}$. Thus, the total transformer losses will be $P_d = P_c + P_w \simeq 220$, reaching an efficiency of

$$\eta = \frac{P_{out}}{P_{out} + P_d} = \frac{25 \cdot 10^3}{25 \cdot 10^3 + 220} = 99.13\% \quad (4.33)$$

The optimization process improves the required minimum efficiency and correctly tunes the value of the leakage inductance. Moreover, winding and core losses are almost equally distributed. In order to validate the methodology, and therefore the chosen characterization expressions, several measurements have been carried out on the prototype transformer.

4.9. Experimental Results

4.9.1. Experimental Set-up

The complete experimental set up was built in the frame of the UNIFLEX-PM project (see Fig. 4.13) and part of it consists of 2 H-bridge converters composed of four 1700V/200A IGBTs, fed by a 1.1 kV dc voltage source.

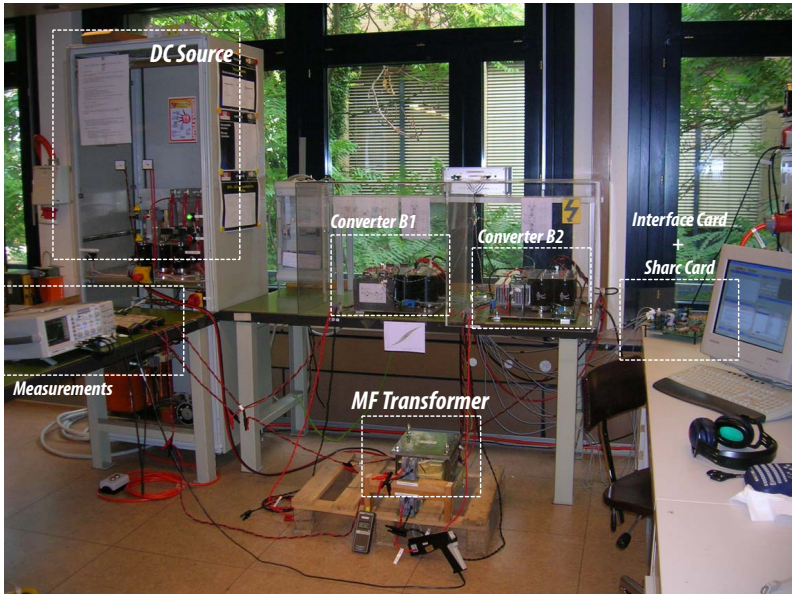


Figure 4.13: Picture of the experimental set-up.

4.9.2. Winding Parasitics Measurements

The easiest way to measure winding parasitics in transformers is using a RCL meter. It is important to use low induction levels, so as to reduce the possible effects introduced by the core. In low-frequency ranges, up to 20 kHz, the RCL meter measures the impedance of a RL device. Considering the equivalent circuit of the transformer (see Fig. 4.14), the inductance measured at the primary with

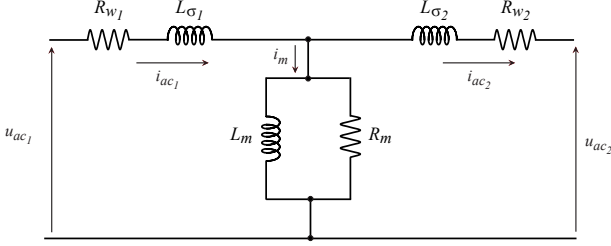


Figure 4.14: Transformer low-frequency model.

the secondary shorted, $L_{p_{sc}}$, is given by

$$L_{p_{sc}} = L_{\sigma 1} + \left(L_{m1} \parallel \frac{L_{\sigma 2}}{n^2} \right) = L_{\sigma 1} + \frac{L_{m1} L_{\sigma 2}}{n^2 L_{m1} + L_{\sigma 2}} \quad (4.34)$$

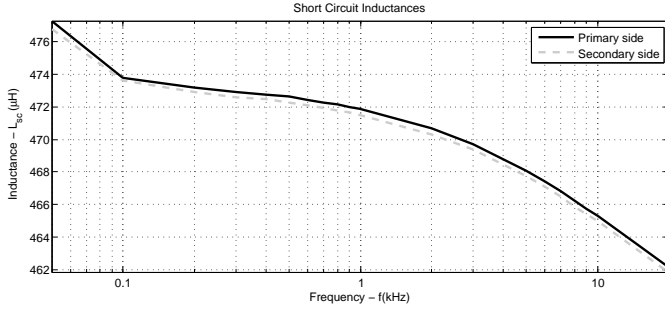
in this case the winding turn ratio is $n = 1$, therefore the equation simplifies to

$$L_{p_{sc}} = L_{\sigma 1} + \frac{L_m L_{\sigma 2}}{L_m + L_{\sigma 2}} \quad (4.35)$$

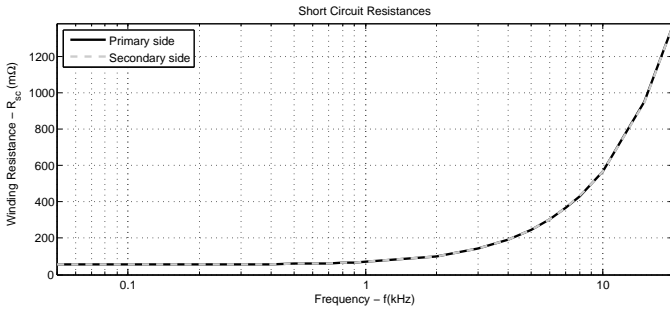
In order to determine the low-frequency equivalent circuit parameters (see Fig. 4.14) of the prototype the Fluke PM6304 RCL Meter has been used. The RCL meter has a 0.1% accuracy and the test frequencies range from 50 Hz to 20 kHz, and 100 kHz.

In Fig. 4.15 the short circuit measurements are illustrated. As the frequency drops to 50 Hz, the apparent leakage inductance seems to increase (see Fig. 4.15a). As the frequency drops, the impedance of the magnetizing inductance falls and becomes comparable to the winding resistance. Therefore, at low measurement frequencies the assumption of a larger magnetizing inductance (neglecting the second term of (4.35)) is no longer correct. This causes the measured leakage inductance to apparently increase.

The leakage inductance at 2 kHz is 470 μH , thus there is an estimation error of 20%, typical when referred to leakage inductance tolerances. This estimation error is tolerated because the final exact curvature and height of the winding are unpredictable, due to manufacturing process.



(a) Inductance.



(b) Resistance.

Figure 4.15: Short circuit primary and secondary side measurements.

The ac resistance of the winding (see Fig. 4.15b) presents the expected behavior, the one already introduced in Fig. 4.12 for a single winding. Therefore, winding parasitics are correctly characterized and tuned using the expressions introduced in Chapter 2 and the optimization methodology proposed in Chapter 3, respectively.

4.9.3. Core Loss Measurements

The measurement schematic is illustrated in Fig. 4.16. The secondary of the transformer is open circuited. The primary of the transformer is excited with a rectangular voltage waveform. The current in the primary will be the image of the

magnetic field, and the induced voltage in the secondary will be directly related with the magnetic induction in the transformer. The current in the primary is measured with a Tektronix TCPA 300/TCP303 150 A dc current sonde. Both voltages on the primary and secondary of the transformer are measured with two High Voltage 7000V Differential Probes. Measurements are stored in an oscilloscope, exactly 5000 points for each measurement, and transferred to a PC.

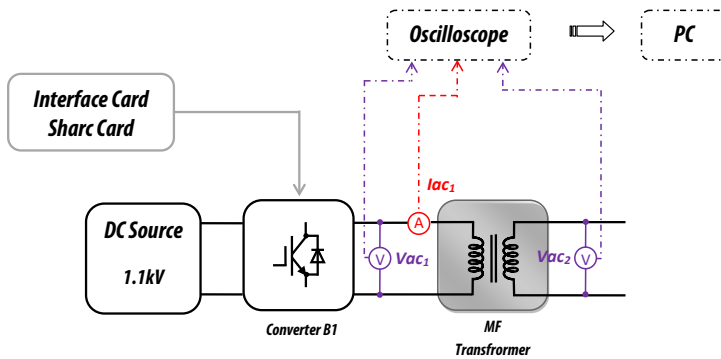


Figure 4.16: Open circuit measurement set-up schematic.

Measurements from the oscilloscope are post-processed as illustrated in Fig. 4.17. The secondary voltage is integrated to get the magnetic induction in the transformer. Both measurements are corrected to have a centered and correct magnetic loop. The surface of the BH loop is measured to get the magnetic energy density, which is appropriately treated to finally get the magnetic losses in the transformer core.

In order to determine the validity of the proposed empirical expression, the primary of the transformer has been excited with various rectangular voltage waveforms while the secondary of the transformer has been left open circuited, or inversely. Both voltages, as well as the primary current, have been measured.

Amplitude response In an initial measurement, a rectangular voltage has been applied to the primary of the transformer, increasing in each step the amplitude of

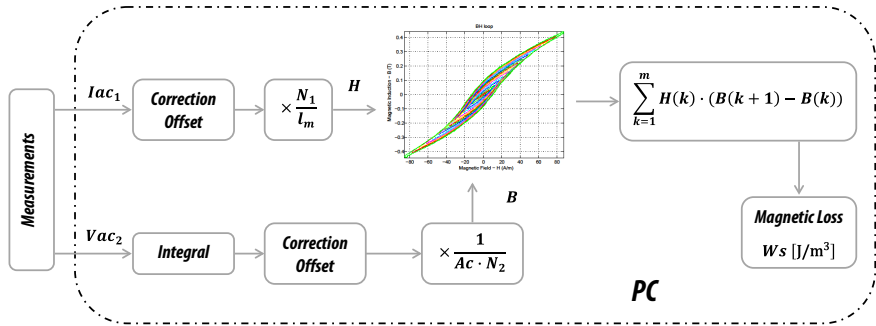


Figure 4.17: PC post-processing schematic.

the dc source voltage, or the excitation voltage of the transformer. The measured secondary voltage as well as the magnetizing current are illustrated in Fig. 4.18.

From the current and voltage measurements the magnetic field and the magnetic induction are determined following the process introduced in Fig. 4.17. The

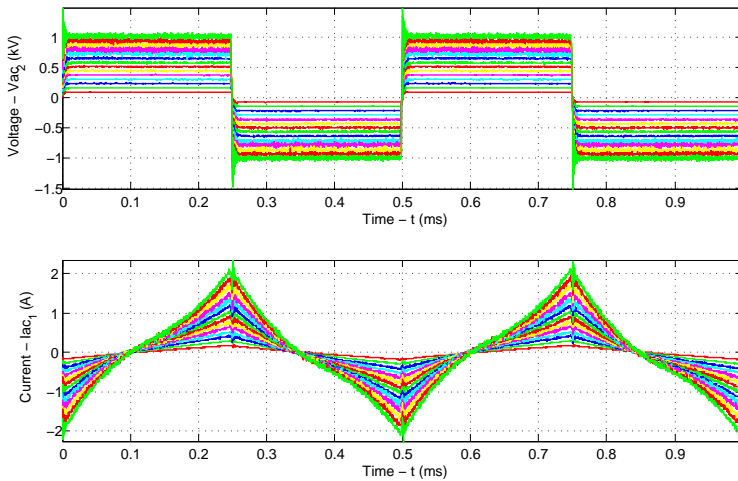


Figure 4.18: Measured voltage and current waveforms.

magnetic characteristic of the transformer for a 2 kHz rectangular voltage, with varying amplitude is illustrated in Fig. 4.19.

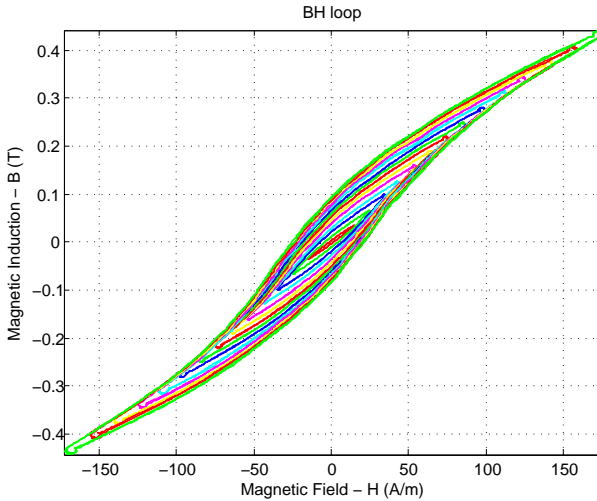


Figure 4.19: BH loop of the prototype. Rectangular voltage excitation at 2 kHz. Two periods are drawn to illustrate the periodicity and to verify the measurement quality.

In the tips of the magnetic characteristic two lobes, one on each tip, are present. Besides offset correction, the measurements have been filtered. The filter is a simple average moving filter, based on a sliding window.

Finally the loss densities for various maximum magnetic inductions have been determined, where along with the predicted core losses are illustrated in Fig. 4.20.

Clearly there is a huge underestimation error. The error is not related with the method but with the deviation on material characteristics, and more precisely the k parameter from the loss expression. As it has been pointed out previously, the iron-based amorphous alloy in its Power System series has been verified, and the estimation was correct (see subsection 3.3.4). However, as there was no loss data for these cores, the equation provided by the manufacturer has been used, which matches well with the results already verified for the Power System series

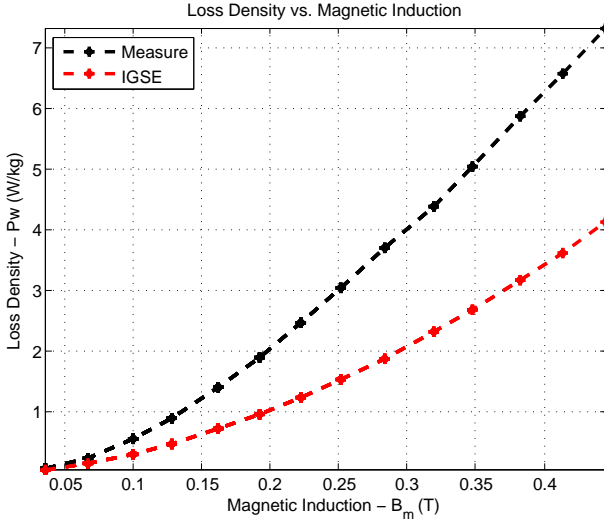


Figure 4.20: Magnetic loss density at 2 kHz and rectangular voltage waveforms.

core. The manufacturer predicted that the loss density with this type of cores and within these frequency ranges will be less than its Power System series core counterpart, which has been proven to be wrong by the obtained measurement results.

Consequently, as there are not any available and reliable data on High Performance Magnetic C-cores for the frequencies considered in this case study, these parameters have been identified experimentally.

Curve Fitting In order to do so, the transformer prototype has been excited with various rectangular voltage waveforms, with a varying amplitude and frequency. Ideally, a magnetic material is characterized using sinusoidal waveforms. However, the transformer is already built-up and it is not a trivial issue to generate a purely sinusoidal 1.1 kV waveform of several frequencies in order to induce the necessary magnetic induction.

The magnetic characteristics of the transformer, i.e. the BH loops, for some of the measured frequencies and excitation voltages are illustrated in Fig. 4.21. The

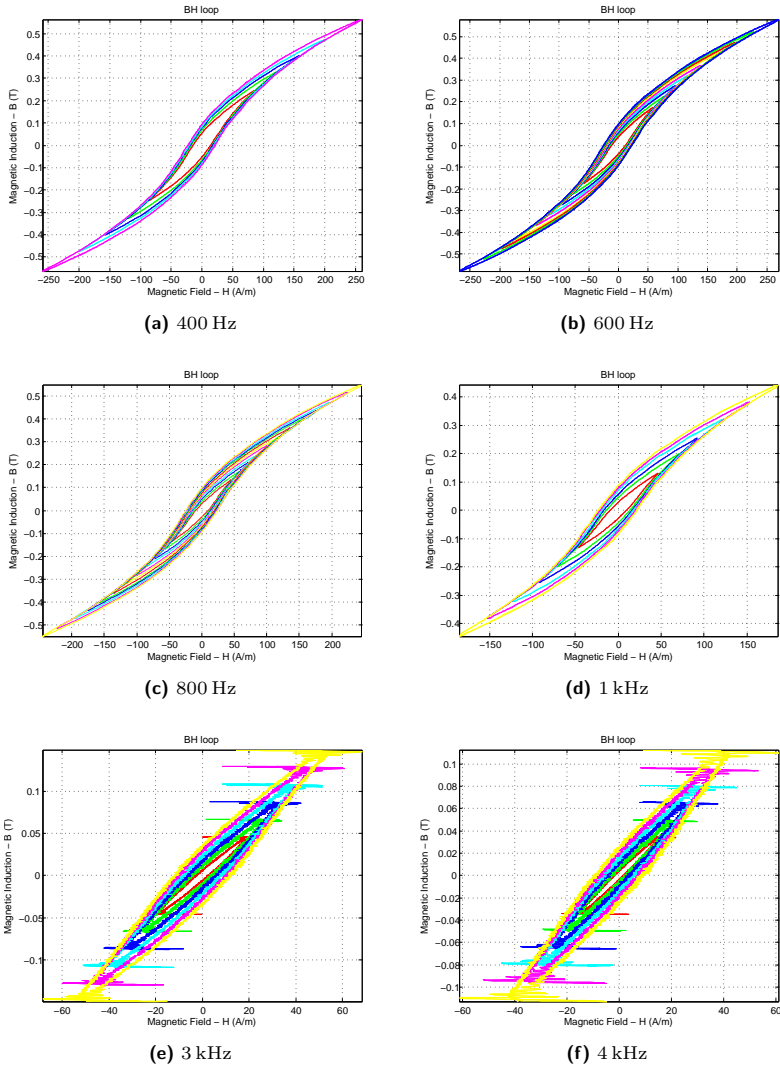


Figure 4.21: Prototype transformer BH loops for various frequencies and excitation voltages.

BH loops at 3 kHz and 4 kHz (see Fig. 4.21e and Fig. 4.21f) are not filtered to illustrate the effect of the parasitic capacitance of the transformer in open circuit measurements. The frequency has been limited to 2 kHz, because there is a clear distortion of the measurement, and also, because the required excitation voltage to get minimum magnetic induction values is out of the converter limits.

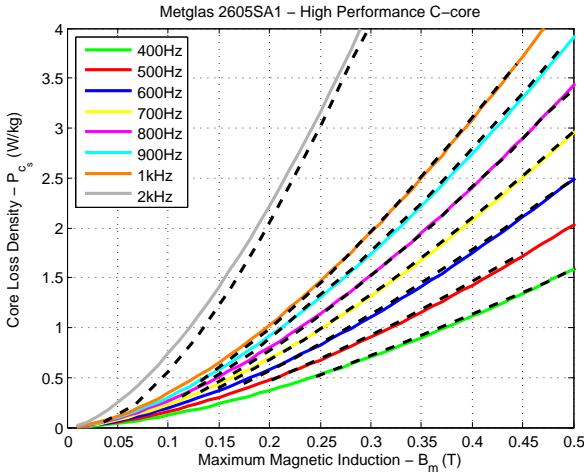


Figure 4.22: Curve fitting (-) of measured data (--), $k_i = 2.0316$, $a = 1.1126$ and $b = 1.5864$.

The curve fitting results are illustrated in Fig. 4.22. From 400 to 1 kHz, the curve fitting is precise enough. However, at 2 kHz, the estimated parameters overestimate the power loss density in the transformer.

In order to understand the behavior of the iron-based amorphous alloys, the dc BH loops of the two cores have been analyzed (see Fig. 4.23), which have been gently provided by the manufacturer. According to the manufacturer, the AMDT core has a longitudinal annealing, while the C-core has a tangential annealing. With a longitudinal annealing, the dc BH loop gets narrower, while with the tangential annealing, the dc BH loop gets flattened, reducing magnetic wall displacement losses (very important in high-frequency operation).

According to the manufacturer, the AMDT core should get wider than the C-core at 2 kHz. However, measurements on both materials show the opposite.

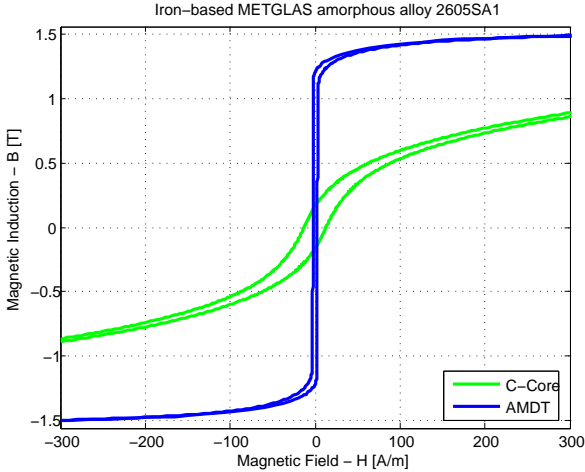


Figure 4.23: Metgals 2605SA1 iron-based amorphous alloy dc BH Loop provided by the manufacturer for the AMDT Cores (Power System Series) and for the Powerlite C-Cores (High-Frequency Series).

Due to the flattened loop, frequency effects should be less harmful in the C-core and at higher frequencies its behavior could be the expected one. Probably, there is a frequency barrier where both loops areas are equal, but at 2 kHz at least, the low-frequency core is still the best solution.

Thus, the validity of the loss expression itself has been verified, and so of the methodology itself, although unexpected material behavior has been found. However, the expected losses will be two times higher, reaching a value of 224 W.

4.9.4. Thermal Response

The measured core losses double the expected ones, therefore the thermal limits of the prototype will be exceeded. In order to control the maximum temperature rise of the transformer, the maximum power transfer has been limited. The schematic of the measurement is illustrated in Fig. 4.24. Both dc sides of the converter are directly connected to the 1100V dc source, and a 6° phase-shift has been introduced between the two active bridges, generating an active power transfer of

17kW. As both dc sides are connected to the same dc source, the only current coming from the source will be the image of the whole converter losses.

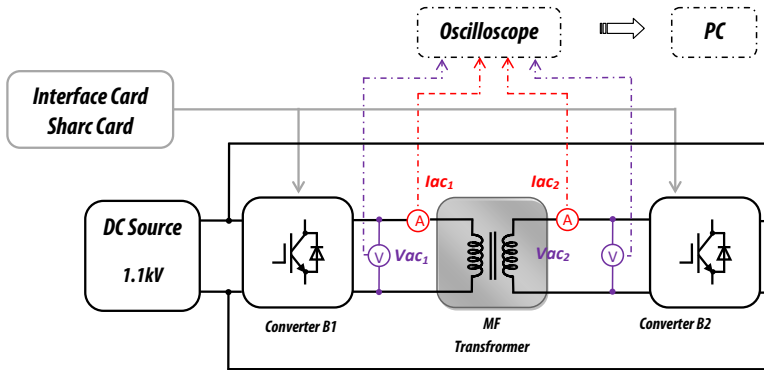


Figure 4.24: Thermal measurement converter schematic.

The proposed transformer design methodology, throughout the optimization process verifies whether or not the temperature limits within the transformer are exceeded, with a maximum permissible surface temperature of 100°C , in an ambient temperature of 40°C , and thus a maximum temperature increase of 60°C . Clearly, the expected temperature will be exceeded, but the characterization procedure introduced in Chapter 2 will still be valid, only with new loss sources. Before introducing the transformer thermal model, the thermal measurements will be analyzed.

4.9.4.1. Thermal Measurements

In order to carry out transformer thermal measurements, three different measurement methods have been used: (a) a thermal camera in order to show the temperature distribution in the frontal face of the transformer, (b) a thermocouple of *type k* placed in the center of the cores to measure the internal temperature behavior of the core, and finally (c) an acquisition card composed of 20 measurement points. All three measurement methods are illustrated in Fig. 4.25.

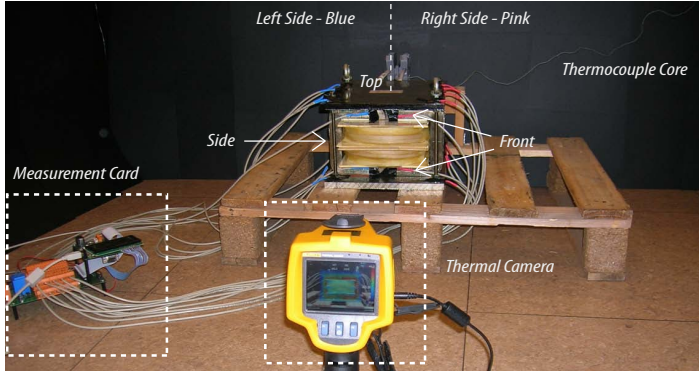


Figure 4.25: Thermal measurement set-up.

Every thermal behavior in the transformer can be described with an exponential function. The transformer has been running for 2h30, and with those measurements a curve fitting has been done to determine the final temperature rise of each measured point.

Thermocouple In the construction phase of the transformer a thermocouple of *type k* was introduced in the center of the transformer, in between the central cores.

A thermocouple is a device that is formed by the union of two different metals that produces a voltage difference in an open circuit, which is a function of the temperature difference between both ends. The thermocouple of *type k*, in particular, is composed of nickel-chromo and nickel-aluminium alloys. As the thermocouple is made of magnetic materials, if the thermocouple is introduced within a magnetic field, measurement errors can be introduced due to induced voltages. Therefore, the correct direction of the thermocouple within this magnetic field is essential to get precise measurements. The resolution of the thermocouple is of 1°C .

In Fig. 4.26 the thermal response of both transformer cores is illustrated. The transformer with varnish has a temperature rise of 67.5°C , while the transformer without varnish shows a temperature rise of 76.3°C . However, it is important to mention that this second thermocouple showed a temperature drop of 4°C as soon as the power from the converter was turned off. Therefore, it can be concluded

that this thermocouple is not correctly placed within the magnetic field of the transformer, and the measurement will be affected by this fact. In the case of the varnished transformer there were no temperature drops detected.

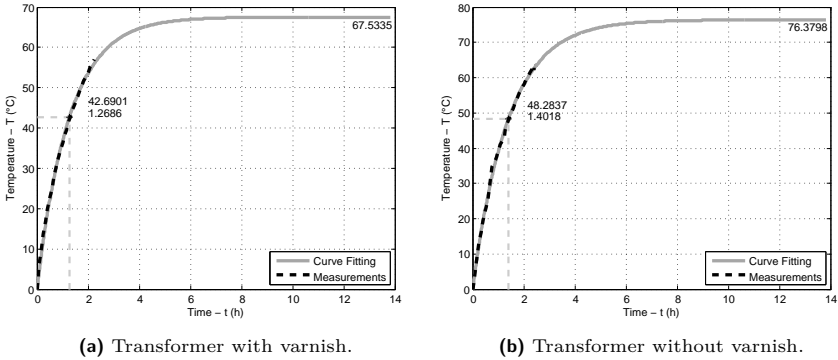


Figure 4.26: Thermocouple in the core of the transformer.

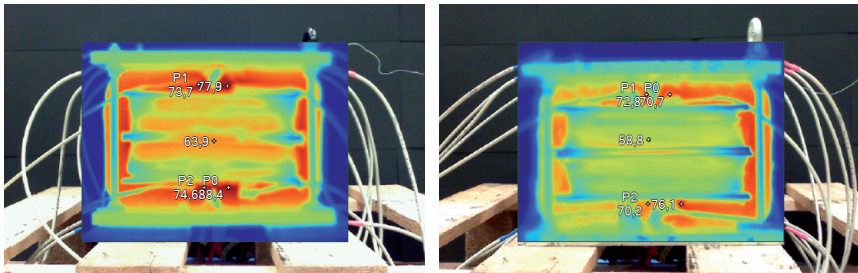
Thermal Camera A thermal camera is a device able to form visible images from the medium infrared electromagnetic spectrum, i.e. is able to measure the thermal radiation of a particular body. Nevertheless, the correct utilization and adjustment is usually difficult. The thermal camera in Fig. 4.25, is a Fluke Ti20 Thermal Imager with a temperature resolution of 0.1°C.

If the measured surface is too reflective or if the transformer is located in a very reflective room, thermal camera measurements will exhibit errors, due to the fact that the reflected beams will be part of the measurement too. Moreover, the thermal camera does only measure with one emissivity, not taking into account the difference between materials. Finally, it is very important to keep the camera as direct as possible, perpendicular to the measured surface, because every angle variation in the measured beam introduces a measurement error.

The converter and transformer are located in a luminous room within the Industrial Electronics Laboratory, that has several reflective screens for security reasons. Thus to reduce every possible measurement error, the surroundings of

the transformer have been covered with black cards, which create a non-reflective volume. Moreover, the black cards have a considerable height to reduce the direct light coming from the exterior.

Even if the measurements are carried out with a predefined emissivity, in the post processing stage the emissivity of every point in the image can be changed by the software. In the post-processing of the images, every pixel in the image can be selected and altered to establish the correct emissivity. In order to compare the measurements carried out with the acquisition card and the thermal camera, four points have been located in the thermal image, which are illustrated for both transformers in Fig. 4.27. Those four points are located near the temperature acquisition points, but not in the exact point due to the difference in emissivity with the sticker. The location of those four reference points is not exactly the same in every thermal image. The software does not provide a coordinate system and the introduction of those points is manual. However, the introduced error with this manual point location is below 0.5°C .



(a) Transformer with varnish.

(b) Transformer without varnish.

Figure 4.27: Transformer thermal image with the four reference points.

The curve fitting results, from both the varnished and the unvarnished transformer are shown in Fig. 4.28 and Fig. 4.29, respectively. The emissivity of the points has been modified in order to illustrate its importance.

In the case of the varnished transformer, results show some coherence, because they almost arrive to the same final temperature. However, in the case of the

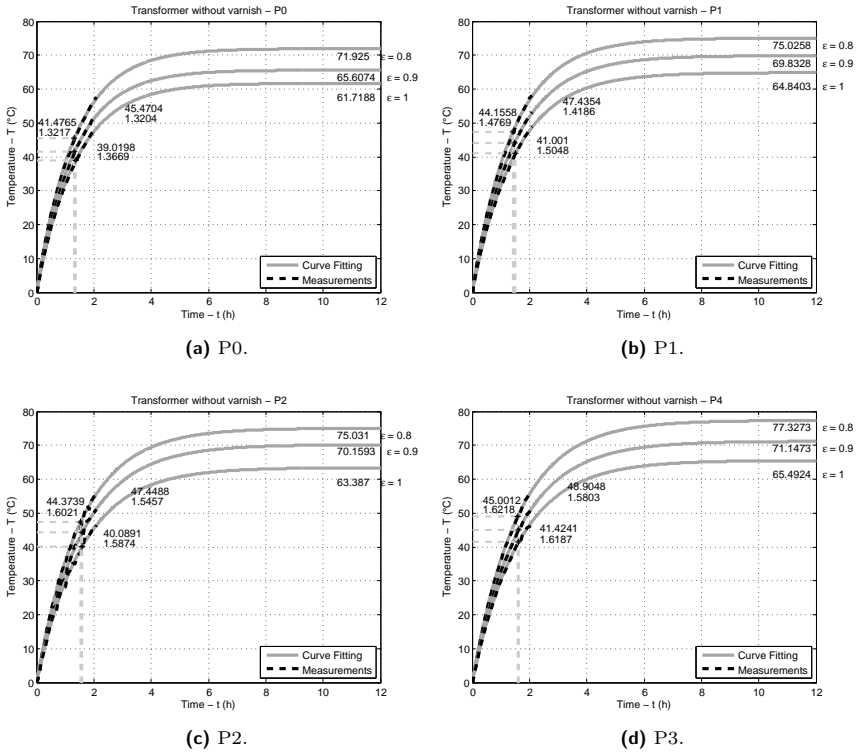


Figure 4.28: Thermal response of the four points within the frontal plane of the varnished transformer.

unvarnished transformer, the points P0 (see Fig. 4.29a) and P1 (see Fig. 4.29b) show remarkable thermal variations, as well as the final estimated temperature. Probably due to isolated reflections from the surrounding to the transformer, and then to the camera. On the contrary, points P2 (see Fig. 4.29c) and P3 (see Fig. 4.29d) show coherent thermal behaviors.

The varnished transformer has a uniform black color, and although it is a little bit shiny, the measurement behavior, apparently, is better.

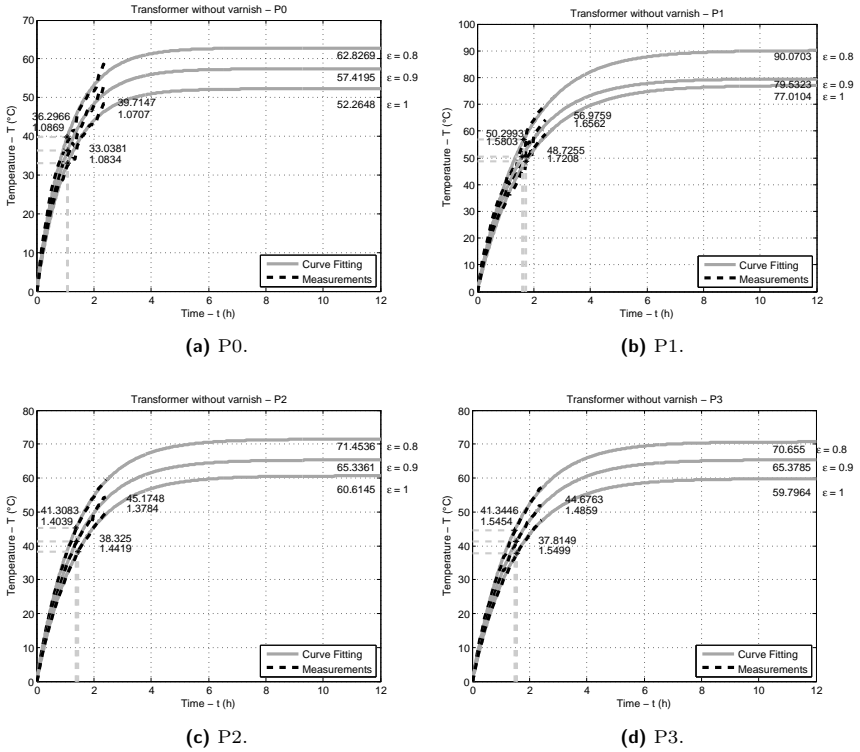
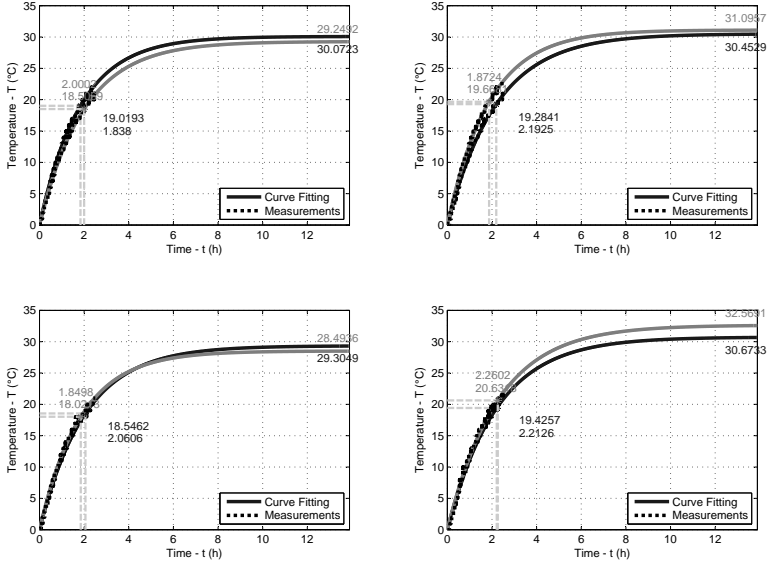


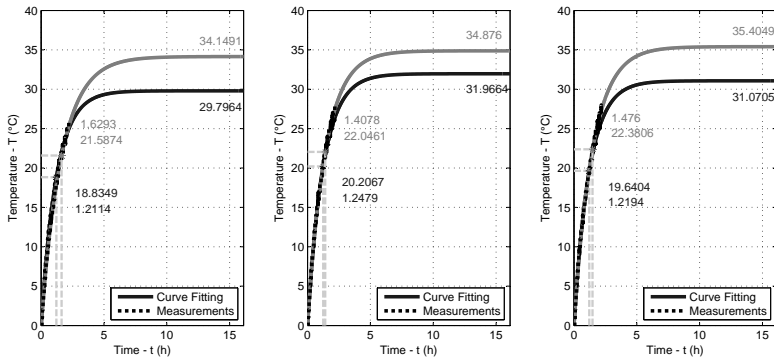
Figure 4.29: Thermal response of the four points within the frontal plane of the unvarnished transformer.

Measurement Card The measurement card is composed of 20 measurement points. The temperature in each point is measured with a programmable digital thermostat and thermometer, DS1821. The circuit measures the temperature by counting the number of clock cycles generated by an oscillator with a low temperature coefficient. Temperature is captured each second with an accuracy of 1°C.

In Fig. 4.30a, the thermal response of the fastening top layer is introduced for the varnished transformer. The fastening structure is made of aluminium and it



(a) At the top of the transformer, 8 measurement points distributed symmetrically by couples.



(b) Measurements almost at the same symmetrical points on transformer sides.

Figure 4.30: Thermal response of the varnished transformer, measurement card. Left-hand side of the transformer gray and right-hand side of the transformer black.

suffers a temperature rise of 30°C.

As well as the sides of the fastening structure of the transformer, the core sides have also been measured (see Fig. 4.25). According to the measurement card results (see Fig. 4.30b), the transformer core on its sides suffers only a temperature rise of 30°C-35°C.

Finally, the four measurement points on the frontal plane of the transformer are illustrated in Fig. 4.31. Apparently, the transformer has a manufacturing dissymmetry that distributes the temperature unequally between both sides, which can also be noticed in the thermal image taken by the camera (see Fig.4.27). Moreover, there is a thermal difference between the top and bottom parts of the transformer. Probably, due to the wooden support placed under the transformer.

The measurement card results matched approximately with the thermal camera measurements, when the emissivity of the surface is set to 1.

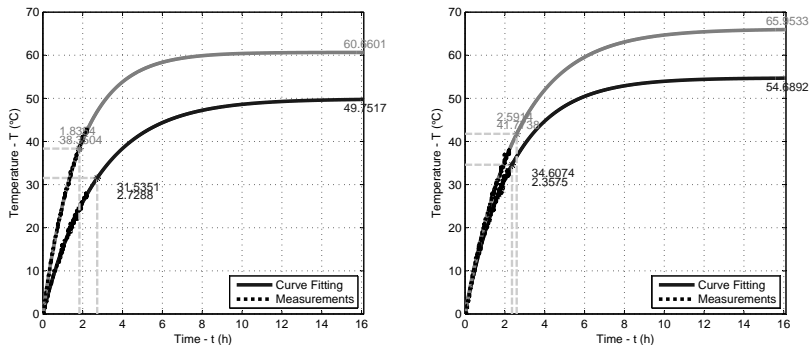


Figure 4.31: Thermal response of the varnished transformer in the frontal 4 measurement points, transformer top side and bottom side. Left-hand side of the transformer gray and right-hand side of the transformer black.

Apparently, the front face of the transformer has difficulties in exteriorizing the heat, because at almost the same transformer height the temperature difference between transformer sides and frontal face are considerable (see Fig. 4.30 and Fig. 4.31). Probably, this is due to the fact that the winding changes the heat flux trajectory, as it has been introduced in Chapter 2, and the heat transfer coefficient

in that specific transformer area is low.

Finally mentioned that the measurements of the black varnished transformer will be used for comparison purposes, due to the fact that they are the most coherent ones.

4.9.4.2. Thermal Model

The transformer has a symmetrical structure, thus only half of the volume can be considered. Moreover, the frontal and back faces of the transformer are not considered, supposing the heat only exteriorizes from the sides of the transformer. Furthermore, due to the winding structure, all the winding heat is supposed to go through the central part of the core. The considered model is illustrated in Fig. 4.32a.

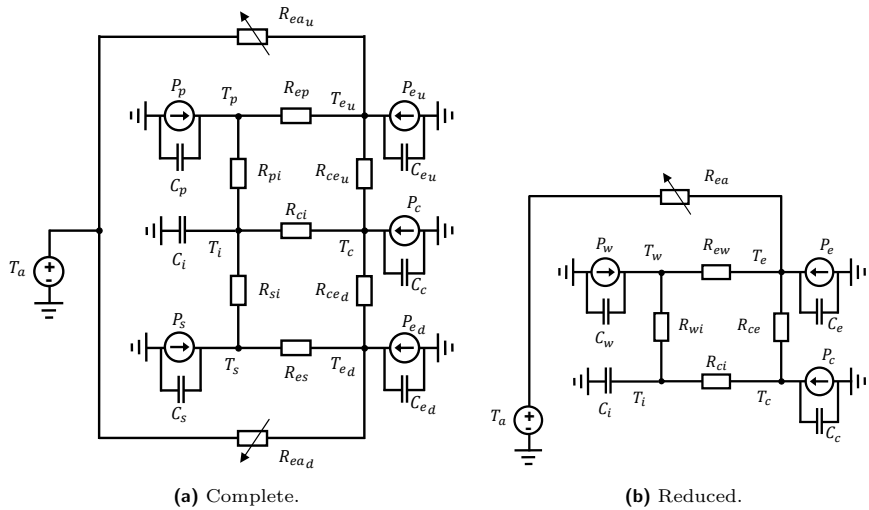


Figure 4.32: Equivalent thermal circuit of the transformer.

Although the upper and lower surfaces of the core do not dissipate heat in the same manner, they usually present an almost identical behavior (see Fig. 4.27). Therefore, the complete model illustrated in Fig. 4.32a is once more reduced,

reaching the simplified network illustrated in Fig. 4.32b.

The thermal network illustrated in Fig. 4.32b can be represented with four first order differential equations:

$$C_c \frac{dT_c}{dt} = \frac{1}{R_{ce}} (T_e - T_c) + \frac{1}{R_{ci}} (T_i - T_c) + P_c \quad (4.36)$$

$$C_e \frac{dT_e}{dt} = \frac{1}{R_{ce}} (T_c - T_e) + \frac{1}{R_{ew}} (T_w - T_e) + \frac{1}{R_{ea}} (T_a - T_e) + P_e \quad (4.37)$$

$$C_w \frac{dT_w}{dt} = \frac{1}{R_{ew}} (T_e - T_w) + \frac{1}{R_{wi}} (T_i - T_w) + P_w \quad (4.38)$$

$$C_i \frac{dT_i}{dt} = \frac{1}{R_{wi}} (T_w - T_i) + \frac{1}{R_{ci}} (T_c - T_i) \quad (4.39)$$

which are simplified to steady-state in order to iteratively solve and reach the final temperature rise.

Each of these equations establish the temperature on the corresponding unknown node. Apart from the primary-to-secondary isolation layer, the rest of the temperature points are connected to a heat source. Moreover, transformer core losses are divided in external and internal core losses, shared according to respective external and internal core volumes.

As the convection and radiation heat transfer mechanisms are temperature dependent, the transformer temperature rise is calculated iteratively. The initial temperature of each node is established at ambient temperature. In each iteration every temperature dependent parameter is evaluated. Besides, the iterative process enables the definition of temperature dependent heat sources.

The final estimated temperature rise for the transformer central column is 67°C, similar to the measurement result. However, the estimated external core temperature reaches a value of 58°C, higher than the measured one. According to this result and the thermal measurements in the external part of the core, part of the winding heat is exteriorized without crossing the external part of the core, which will estimate a smaller temperature increase.

4.10. Conclusions

The aim of this chapter was to apply the proposed methodology to a case study, a Dual Active Bridge developed in the context of the UNIFLEX-PM European project. The equations that describe the converter behavior, along with the transformer characterization equations have been introduced.

The optimization methodology correctly tunes the value of the leakage inductance, and improves the expected efficiency. Moreover, winding and core losses are almost equally shared.

The characterization expressions introduced in Chapter 2 has been verified, although unexpected core loss behavior has been found. In order to face this unexpected behavior, curve fitting of the measured data has been done reaching new material values for proper characterization of the selected magnetic core.

Finally, the thermal behavior of the transformer has been measured, and also the measurement difficulties and errors have been pointed out, closing the section with a simplified thermal model of the transformer.

5

Conclusions and Future Work

5.1. Summary

Current high-power semiconductor devices, along with new magnetic materials, enable a potential substitution of bulky low-frequency transformers with new conversion structures. These conversion structures combine fast and efficient switching devices with medium-frequency power transformers. The overall volume of the conversion structure is reduced due to the higher operation frequency of the transformer.

Apart from the inherent low-frequency transformer characteristics, like voltage adaptation and isolation, these conversion structures add several functionalities to the system like power flow regulation and power quality improvement. Therefore, these Power Electronic Transformers offer two types of advantages: a physical one with volume and weight reduction, and a functional one. Although there are several applications in the literature related to the functional advantage of Power Electronic Transformers (mostly related to medium-voltage distribution grids), the most promising improvement is the physical one. Apart from several proposals found on the literature, a considerable amount of industrial companies (mostly related to traction and wind energy) not only propose but have already built a Power Electronic Transformer prototype.

The core element of all these conversion systems is the medium-frequency power transformer and its correct characterization is essential for an optimized Power Electronic Transformer design. Within this thesis report, several aspects of medium-frequency power transformer characterization have been thoroughly analyzed. The non-sinusoidal excitation waveforms of these medium-frequency power transformers demand a reevaluation of conventional characterization design methodologies. High-power densities, with medium operational frequencies require new conductor types to face detrimental frequency effects until now not present in high-power applications. Thus, adequate field expressions are necessary to correctly characterize transformer behavior. Moreover, the non-sinusoidal excitation voltages generate magnetic losses that need correct characterization. In order to face these problems, optimal conductor expressions, along with specific core-loss parameters, have been proposed to initiate the way towards optimization.

5.2. Contributions

The first main contribution of this thesis encompasses the figures of characterization. A thorough analysis of current loss expressions has been introduced, filling the void of comparison and validity studies, especially in relation to round Litz wires and modified Steinmetz expressions. In both cases, the characterization problem has been transferred to the current medium-frequency case study with simple, precise and easily manageable expressions.

In a second phase, a new medium-frequency design methodology has been introduced. Instead of having a magnetic core look-up table, a wire look-up table is proposed, always following specific and clear initial design criteria. This proposition arises both, from the need to allocate actual Litz wires in a core window and, from the specific leakage inductance value requirements. Conventional transformer design methodologies, are based on solid conductors, and use in some cases Dowell's expression. However, if the solid conductor needs to be replaced by a Litz wire with the same effective area, the final covered core window area will be much bigger. Moreover, not only the window area will be insufficient, but winding layer distribution will have to be changed too. The expected number of turns in each layer will be far away from the optimized design, requiring more layers to keep magnetic induction values, and thus increasing copper losses due to the increase in layers. Finally, losses will be distributed within the transformer without any optimized pattern. In contrast the proposed methodology succeeds to obtain an optimal design by realizing an initial study based on the current waveform, and selecting accordingly a set of optimal conductors. The final conductor geometry is considered within the optimization process, avoiding a second verification as in conventional methodologies. Moreover, within the proposed methodology, an expression for the determination of the optimal strand diameter for round Litz bundles has been developed, reaching a compact and easily manageable expression.

Besides the proposed methodology in Chapter 3, several operational limits of high-power amorphous cores have been pointed out. The standard dimensions offered by the manufacturer limit the maximum current density to 1.75 A/mm^2 if natural cooling is considered, while this maximum current density can be increased up to 4 A/mm^2 if forced cooling is the choice. Moreover, the operational frequency

of this type of cores can not exceed the 4 kHz limit for naturally cooled transformers, and the 12 kHz one for forced cooling cases, if equal loss sharing is expected in order to reach the maximum transformer efficiency.

The proposed design methodology has been validated in Chapter 4, with the construction of a medium-frequency power transformer prototype, which reaches the desired leakage inductance value, excess the expected efficiency, and equally shares the loss within the transformer. Furthermore, the characterization expressions have been verified in a second measurement stage, getting the expected windings parasitics behavior. In addition, the encountered unexpected magnetic core behavior has captured much of the attention, emphasizing an important point for future medium-frequency transformer designs: the necessity of a prior verification of the magnetic material behavior. It has been demonstrated, that there was a considerable lack of available and reliable data related to High Performance Magnetic C-cores for the frequencies considered in this case study. In order to fill this gap, a series of experimental tests have been carried out and the core has been characterized, which can be considered as another contribution made in this work.

5.3. Future work

In the final stage of this thesis, some acoustic measurements have been done in order to point out the challenge that medium-frequency power transformers will have to face in future medium-voltage applications.

The maximum acceptable sound power level for human beings is located around 65 dB. However, as it is clearly illustrated in Fig. 5.1, the iron-based amorphous core presents maximum power levels of 100 dB, even for small induction values. The dominant noise generating source of transformers is usually magnetostriction (the change in magnetic material dimensions), which is inherently high in iron-based amorphous alloys ($\lambda^s = +27$ ppm). Magnetostriction creates an oscillation of the core at twice the switching fundamental frequency (see Fig. 5.1), clearly dominating the sound spectrum of the prototype transformer.

Thus, the noise levels generated by these Power Electronic Transformers will be a crucial issue to be solved for the successful future deployment of this kind of technology. If magnetic material characteristics do not change, and considering

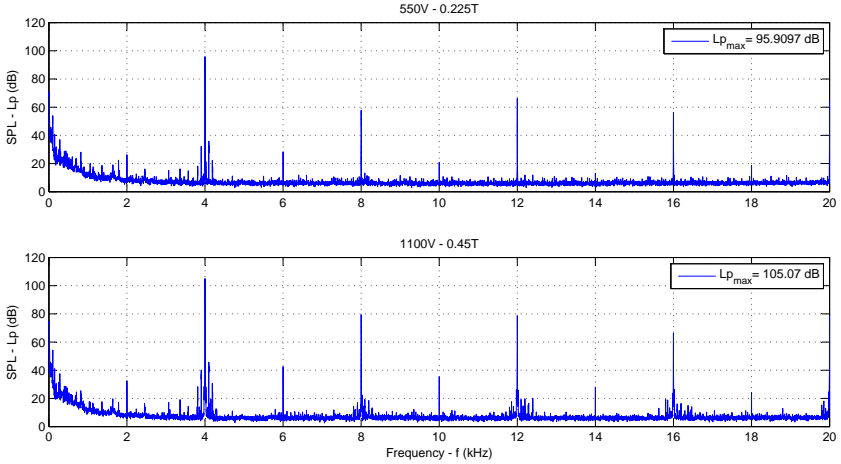


Figure 5.1: Acoustic measurements at 2 kHz.

current noise pressure levels, the design of any acoustic barrier, passive or active, will be essential, in order to transfer this technology to the final user.

Even if noise is probably the main challenge that will be faced by medium-frequency transformers, it is not the only one. Reliability issues related to the complex structures employed in this kind of conversion systems, together with a cost reduction necessity, will have to be correctly addressed to gain the confidence and predilection of future users. In addition, the necessity of using high-voltage levels will lead to new specific isolation materials and forms.

In any case if medium-frequency conversion systems are able to successfully face at least the main technological challenges (noise and reliability), we will see in a few years, a progressive deployment of this technology in diverse niche energy and transportation applications, where special requirements of volume, weight or space may lead to the adoption of this solutions. If, in addition, these technological improvements are accompanied with a drastic price reduction, which seems to be quite far today, it could even become the "standard" conversion solution of the future.



Mathematical Developments

A.1. Time Harmonic Diffusion Equation

Time harmonic Maxwell equations in phasorial form are:

$$\nabla \times \mathbf{E} = -j\omega\mu\mathbf{H} \quad (\text{A.1})$$

$$\nabla \times \mathbf{H} = \mathbf{J} + j\omega\epsilon\mathbf{E} \quad (\text{A.2})$$

$$\nabla \cdot \mathbf{E} = \rho_v/\epsilon \quad (\text{A.3})$$

$$\nabla \cdot \mathbf{H} = 0. \quad (\text{A.4})$$

Along with the constitutive relationship of a conducting material:

$$\mathbf{J} = \sigma \mathbf{E}. \quad (\text{A.5})$$

Neglecting displacement currents and substituting (A.5) in (A.2),

$$\nabla \times \mathbf{H} = \mathbf{J} \quad \Rightarrow \quad \nabla \times (\nabla \times \mathbf{H}) = \sigma(\nabla \times \mathbf{E}), \quad (\text{A.6})$$

And finally the diffusion equation is reached equating (A.6) with (A.1),

$$\nabla^2 \mathbf{H} = j\sigma\omega\mu\mathbf{H} \quad (\text{A.7})$$

A.1.1. Diffusion Equation in Cartesian Coordinates

The magnetic field is a vector phasor which contains information about the direction, magnitude and phase (A.8).

$$\mathbf{H}(x, y, z) = \mathbf{a}_x H_x + \mathbf{a}_y H_y + \mathbf{a}_z H_z \quad (\text{A.8})$$

Rewriting the diffusion equation in cartesian coordinates

$$\begin{aligned} & \left(\frac{\partial^2 H_x}{\partial x^2} + \frac{\partial^2 H_x}{\partial y^2} + \frac{\partial^2 H_x}{\partial z^2} \right) \mathbf{a}_x + \\ & \left(\frac{\partial^2 H_y}{\partial x^2} + \frac{\partial^2 H_y}{\partial y^2} + \frac{\partial^2 H_y}{\partial z^2} \right) \mathbf{a}_y + \\ & \left(\frac{\partial^2 H_z}{\partial x^2} + \frac{\partial^2 H_z}{\partial y^2} + \frac{\partial^2 H_z}{\partial z^2} \right) \mathbf{a}_z = j\sigma\omega\mu (\mathbf{a}_x H_x + \mathbf{a}_y H_y + \mathbf{a}_z H_z) \end{aligned} \quad (\text{A.9})$$

In the case of magnetic core windows, the magnetic field has only one direction, y , and varies according to another one, x , (A.10).

$$\mathbf{H}(x) = \mathbf{a}_y H_y(x) \quad (\text{A.10})$$

The reduced equation (A.11) becomes a differential equation due to the single axis dependency.

$$\frac{d^2 H_y(x)}{dx^2} = j\sigma\omega\mu \mathbf{a}_y H_y(x) \quad (\text{A.11})$$

A.1.2. Diffusion Equation in Cylindrical Coordinates

The magnetic field vector phasor in cylindrical coordinates:

$$\mathbf{H}(r, \phi, z) = \mathbf{a}_r H_r + \mathbf{a}_\phi r H_\phi + \mathbf{a}_z H_z \quad (\text{A.12})$$

Rewriting the diffusion equation:

$$\begin{aligned} & \left(\frac{\partial^2 H_r}{\partial r^2} + \frac{1}{r^2} \frac{\partial^2 H_r}{\partial \phi^2} + \frac{\partial^2 H_r}{\partial z^2} + \frac{1}{r} \frac{\partial H_r}{\partial r} - \frac{2}{r^2} \frac{\partial H_\phi}{\partial \phi} - \frac{H_r}{r^2} \right) \mathbf{a}_r + \\ & \left(\frac{\partial^2 H_\phi}{\partial r^2} + \frac{1}{r^2} \frac{\partial^2 H_\phi}{\partial \phi^2} + \frac{\partial^2 H_\phi}{\partial z^2} + \frac{1}{r} \frac{\partial H_\phi}{\partial r} + \frac{2}{r^2} \frac{\partial H_r}{\partial \phi} - \frac{H_\phi}{r^2} \right) \mathbf{a}_\phi + \\ & \left(\frac{\partial^2 H_z}{\partial r^2} + \frac{1}{r^2} \frac{\partial^2 H_z}{\partial \phi^2} + \frac{\partial^2 H_z}{\partial z^2} + \frac{1}{r} \frac{\partial H_z}{\partial r} \right) \mathbf{a}_z \\ & = j\sigma\omega\mu (\mathbf{a}_r H_r + \mathbf{a}_\phi r H_\phi + \mathbf{a}_z H_z) \end{aligned} \quad (\text{A.13})$$

Once more, the magnetic field has only one direction, ϕ , and varies according to r , therefore the reduced one dimensional equation is:

$$r^2 \frac{d^2 H_\phi(r)}{dr^2} + r \frac{dH_\phi(r)}{dr} - (1 + r^2 (j\sigma\omega\mu)^2) H_\phi(r) = 0 \quad (\text{A.14})$$

A.2. Conduction Loss Expression

Using current density

$$P_{\sigma} = \frac{1}{\sigma} \int_V \mathbf{J} \cdot \mathbf{J}^* \, dv \quad (\text{A.15})$$

or using Poynting vector

$$\mathcal{P} = \mathbf{E} \times \mathbf{H} \quad (\text{A.16})$$

A.2.1. Conduction Loss Expression in Cartesian Coordinates

The current density in cartesian coordinates, already introduced in section 2.2.2.1, is rewritten so as to develop the expression for conduction losses.

$$J_z(x) = \alpha H_{ext} \frac{\cosh(\alpha x)}{\sinh(\alpha d_w)} - \alpha H_{int} \frac{\cosh(\alpha(x - d_w))}{\sinh(\alpha d_w)} \quad (\text{A.17})$$

From the one dimensional current density, the conduction loss expression in a conduction layer located within a transformer window will be derived from:

$$P_{\sigma} = \frac{1}{2\sigma} \int_V |J_z^2(x)| \, dv = \frac{1}{2\sigma} \int_{x=0}^{x=d_w} |J_z^2(x)| h_w l_w \, dx \quad (\text{A.18})$$

The resolution of the equation leads to the following expression:

$$P_{\sigma} = \frac{l_w h_w}{2 \delta \sigma} \left[(H_{ext} + H_{int})^2 \frac{\sinh(2\Delta) + \sin(2\Delta)}{\cosh(2\Delta) - \cos(2\Delta)} - 4 H_{int} H_{ext} \frac{\sinh(\Delta) \cos(\Delta) + \cosh(\Delta) \sin(\Delta)}{\cosh(2\Delta) - \cos(2\Delta)} \right] \quad (\text{A.19})$$

The following two mathematical identities arise from the solution of the hyperbolic functions:

$$\frac{\sinh(2\Delta) + \sin(2\Delta)}{\cosh(2\Delta) - \cos(2\Delta)} = \frac{1}{2} \left[\frac{\sinh(\Delta) + \sin(\Delta)}{\cosh(\Delta) - \cos(\Delta)} + \frac{\sinh(\Delta) - \sin(\Delta)}{\cosh(\Delta) + \cos(\Delta)} \right] \quad (\text{A.20})$$

$$\frac{\sinh(2\Delta) + \sin(2\Delta)}{\cosh(2\Delta) - \cos(2\Delta)} = \frac{\sinh(\Delta) - \sin(\Delta)}{\cosh(\Delta) + \cos(\Delta)} + \frac{2(\sinh(\Delta)\cos(\Delta) + \cosh(\Delta)\sin(\Delta))}{\cosh(2\Delta) - \cos(2\Delta)} \quad (\text{A.21})$$

Substituting the previous identities in (A.19) leads to the final equation introduced in section 2.2.2.1.

A.3. Bessel Functions

$$J_\nu(z e^{3\pi j/4}) = \text{ber}_\nu(z) + j \text{bei}_\nu(z) \quad (\text{A.22})$$

therefore

$$\text{ber}_\nu(z) = \Re \left[J_\nu(z e^{3\pi j/4}) \right] \quad \text{and} \quad \text{bei}_\nu(z) = \Im \left[J_\nu(z e^{3\pi j/4}) \right] \quad (\text{A.23})$$

from where

$$\text{ber}'_\nu(z) = \frac{\text{ber}_\nu(z) + \text{bei}_\nu(z)}{\sqrt{2}} \quad \text{and} \quad \text{bei}'_\nu(z) = \frac{-\text{ber}_\nu(z) + \text{bei}_\nu(z)}{\sqrt{2}} \quad (\text{A.24})$$

A.4. Approximations for Modified Bessel Functions

For small arguments the modified Bessel functions can be approximated by the leading terms in the series expansion:

$$I_\nu(z) \sim \frac{z^\nu}{2^\nu \nu!} \quad (\text{A.25})$$

and

$$K_\nu(z) \sim 2^{\nu-1} (\nu-1)! z^{-\nu} \quad (\text{A.26})$$

For large values of the complex argument the asymptotic forms are:

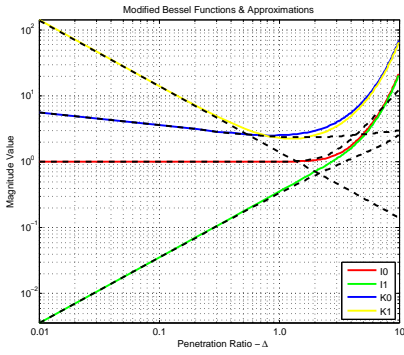
$$I_\nu(z) \sim \frac{e^z}{\sqrt{2\pi z}} \quad (\text{A.27})$$

and

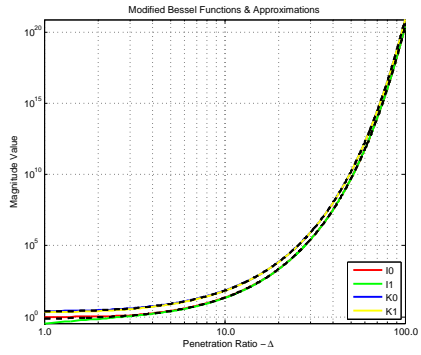
$$K_\nu(z) \sim e^{-z} \sqrt{\frac{\pi}{2z}} \quad (\text{A.28})$$

In the case of single round conductors or Litz wire strands, the winding will be design so as to reduce the frequency effects. Therefore, the radius of the conductor will be smaller than the skin depth ($r < \delta$). In those cases the small arguments approximations will be valid. However, in the case of coaxial conductors the radius will be higher than the skin depth ($\delta < r$), because the central, at least of the external conductor, is empty. Therefore, for the external conductor the large arguments approximations will be valid. In the case of internal conductors the correct approximation will vary, whether the conductor is full or void, and depending on its dimensions.

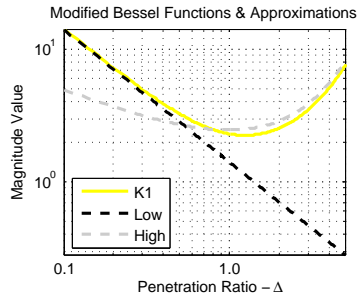
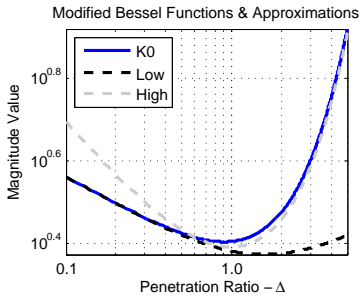
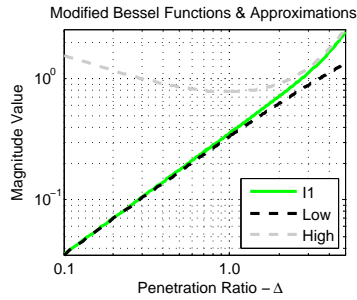
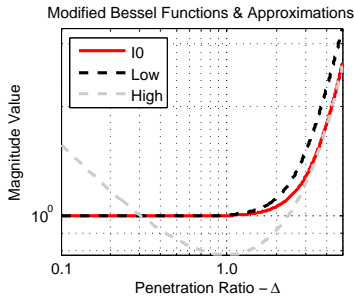
In Fig. A.1 small and large argument approximations are shown, along with the original curves. Moreover, the transition region is highlighted to illustrate clearly the validity regions.



(a) Small arguments.



(b) Large arguments.



(c) Transition from small to large arguments.

Figure A.1: Bessel functions and approximations for various arguments.

B

Physical Properties

B.1. Thermal Properties of Various Fluids

Fluid	Variable	Expression	Unit
Air	ρ	$1.225 \cdot 273 / (T + 258)$	$[\text{kg}/\text{m}^3]$
	β	$1 / (T + 273)$	$[1/\text{K}]$
	μ	$16.8 \cdot 10^{-6} + 52 \cdot 10^{-9} T$	$[\text{kg}/\text{m s}]$
	λ	$0.0242 + 6.2 \cdot 10^{-5} T$	$[\text{W}/\text{m K}]$
	c_p	1000	$[\text{J}/\text{kg K}]$
Oil	ρ	$887 - 0.659 T$	$[\text{kg}/\text{m}^3]$
	β	$8.6 \cdot 10^{-4}$	$[1/\text{K}]$
	μ	$0.13573 \cdot 10^{-5} \exp(2797.3/(T) + 273)$	$[\text{kg}/\text{m s}]$
	λ	$0.124 - 1.525 \cdot 10^{-4} T$	$[\text{W}/\text{m K}]$
	c_p	$1960 + 4.005 T$	$[\text{J}/\text{kg K}]$
Silicone	ρ	$989 - 0.87 T$	$[\text{kg}/\text{m}^3]$
	β	$9.5 \cdot 10^{-4}$	$[1/\text{K}]$
	μ	$0.12127 \cdot 10^{-3} \exp(1782.3/(T) + 273)$	$[\text{kg}/\text{m s}]$
	λ	$0.138 - 9.621 \cdot 10^{-5} T$	$[\text{W}/\text{m K}]$
	c_p	1500	$[\text{J}/\text{kg K}]$

Table B.1: Thermal properties of various fluids, T = temperature [$^{\circ}\text{C}$].

B.2. Operating Limits for Oil Cooling

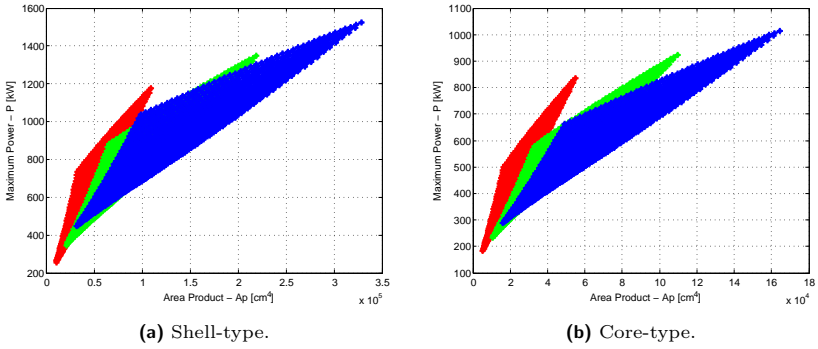


Figure B.1: Maximum power, supposing an efficiency of $\eta = \%99$. Possible transformer configurations with $D = 146$ mm and $A=[25$ mm (red), 50 mm (green), 75 mm (blue)]. Natural convection with $T_{amb} = 40$ °C, $T_{surface} = 100$ °C and $\varepsilon = 0.8$.

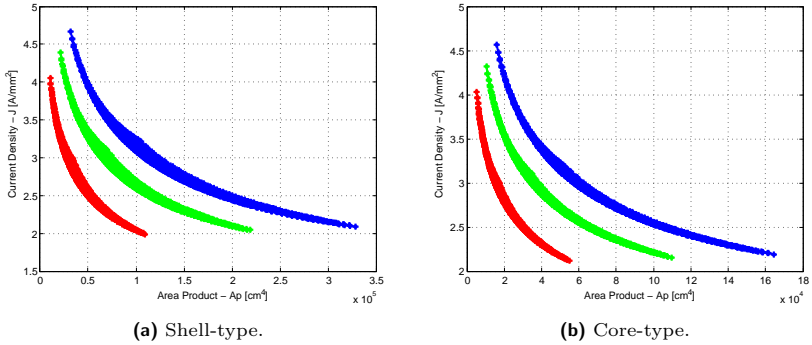


Figure B.2: Current density vs area product. Possible transformer configurations with $D = 146$ mm and $A=[25$ mm (red), 50 mm (green), 75 mm (blue)]. Natural convection with $T_{amb} = 40$ °C, $T_{surface} = 100$ °C and $\varepsilon = 0.8$. Filling factor 0.2.

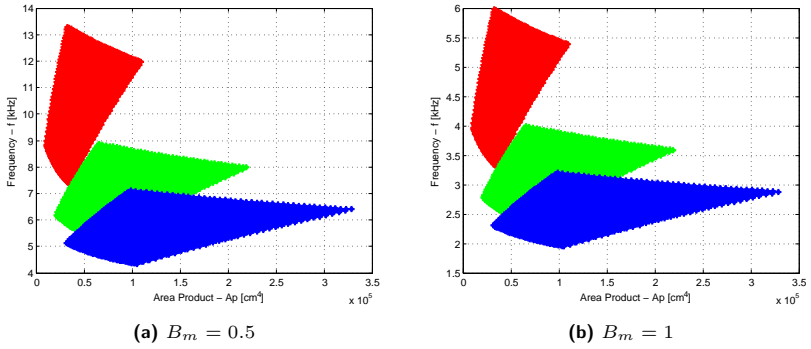


Figure B.3: Operating frequency range for a shell-type transformer. Possible transformer configurations with $D = 146$ mm and $A=[25$ mm (red), 50 mm (green), 75 mm (blue)]. Natural convection with $T_{amb} = 40$ °C, $T_{surface} = 100$ °C and $\varepsilon = 0.8$.

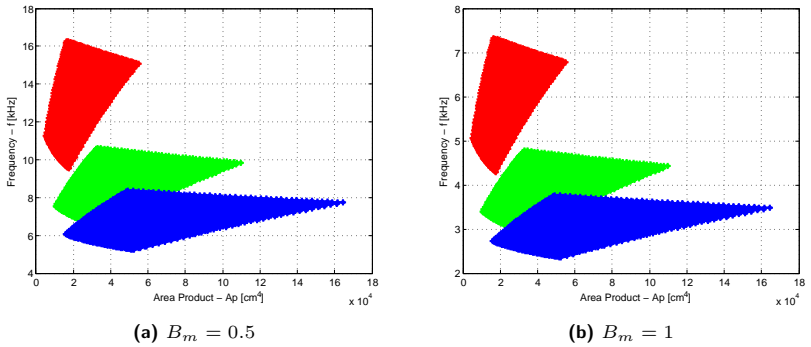


Figure B.4: Operating frequency range for a core-type transformer. Possible transformer configurations with $D = 146$ mm and $A=[25$ mm (red), 50 mm (green), 75 mm (blue)]. Natural convection with $T_{amb} = 40$ °C, $T_{surface} = 100$ °C and $\varepsilon = 0.8$.

C

**Optimal Conductor Thickness Estimation
Error**

C.1. Optimal Conductor Thickness

In Fig. C.1 the minimum value for each number of total layers is represented, which corresponds to an optimum value of Δ , and therefore an optimum value of d , for each operating frequency.

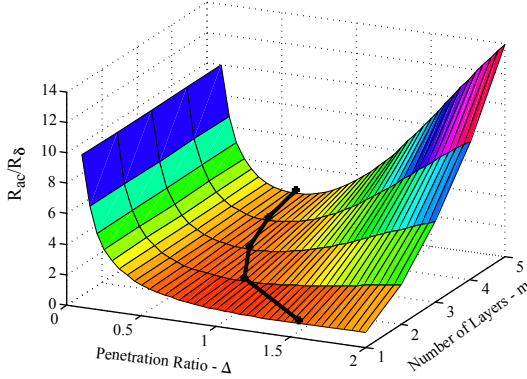


Figure C.1: R_{ac}/R_δ vs. Δ and m . The minimum point for each number of layers is highlighted.

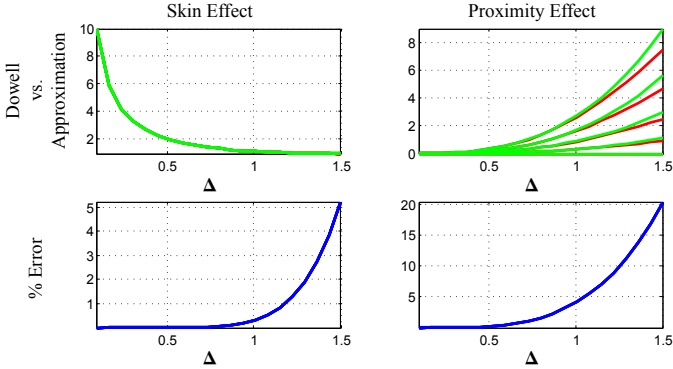
In order to reach the simplified expression for the optimal layer thickness introduced in subsection 3.2.8 some approximations have been used in the development of the expression [Hurley et al., 2000]. The resistance factor expression has been rewritten in its power series form with terms up to the third power.

$$\text{Skin Effect} \quad \varsigma_1 = \frac{\sinh(2\Delta) + \sin(2\Delta)}{\cosh(2\Delta) - \cos(2\Delta)} = \frac{1}{\Delta} + \frac{4}{45}\Delta^3 \quad (\text{C.1})$$

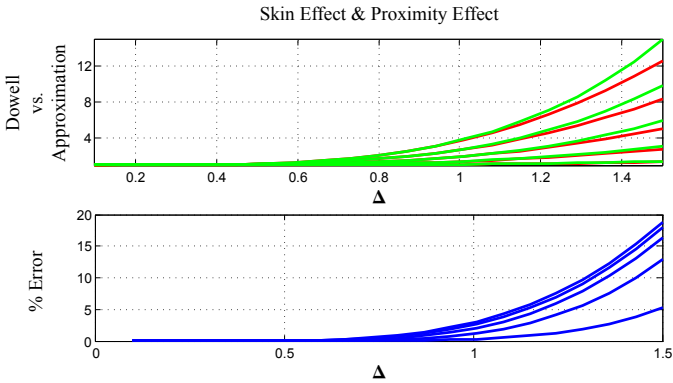
$$\text{Proximity Effect} \quad \varsigma_2 = \frac{\sinh(\Delta) - \sin(\Delta)}{\cosh(\Delta) + \cos(\Delta)} = \frac{1}{6}\Delta^3$$

In Fig. C.2, the exact expression and the approximation are illustrated. As long as the optimum penetration ratio Δ_{opt} results below 1, the introduced error stays below %5 (see Fig. C.2).

In order to verify the simplified optimization expression, an iterative process has been carried out, for the current introduced in the case study analyzed in Chapter 4. The iterative study establishes foil conduction losses for different cur-



(a) Skin and proximity effects



(b) Total

Figure C.2: Dowell expression, power series approximation and incurred error for different values of the penetration ratio.

rent waveforms (γ), possible layer thickness ranges and various number of layers. In Fig. C.3 the minimum loss points from the iterative evaluation process are highlighted (*) and the corresponding loss points for the predicted optimum foil thickness (*).

In Fig. C.4 the estimation error for various cases is illustrated. The committed error is much higher than the predicted error in Fig. C.2, because in that case the

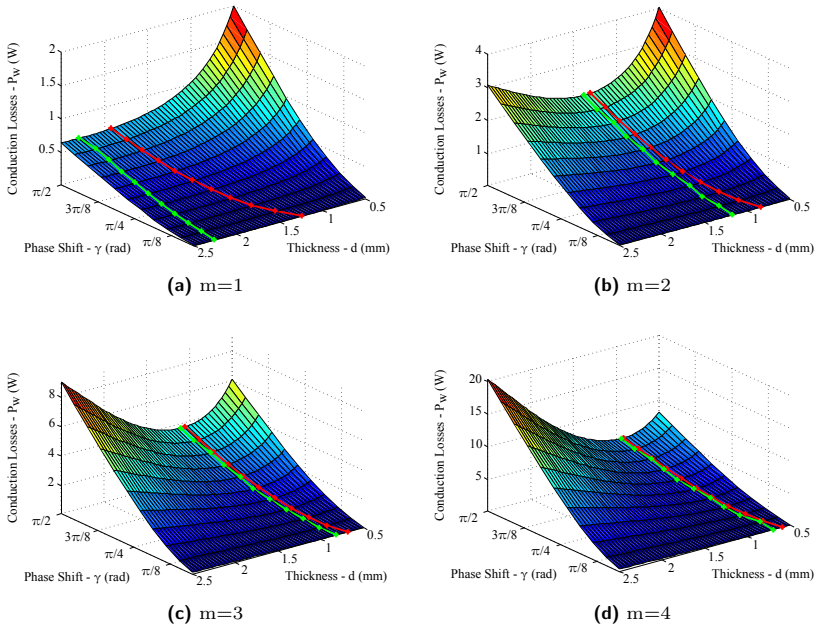


Figure C.3: Estimation of conduction losses. The minimum from the iterative evaluation and from the optimal conductor thickness are highlighted.

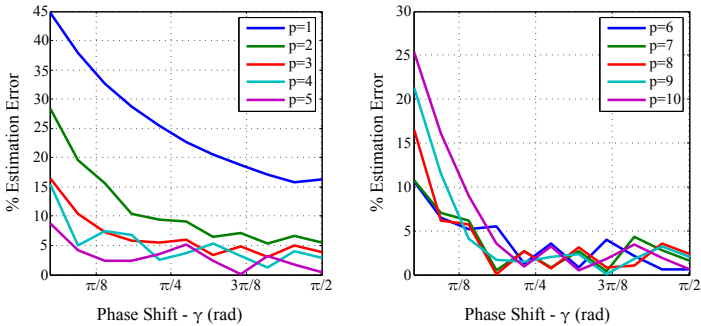


Figure C.4: Estimation error in the case of the Dual Active Bridge currents.

error was established for a single harmonic component, while in real non-sinusoidal waveforms the error for each component will have to be added. It can be seen in Fig. C.4 that the error reduces when the number of layers is increased. The estimation error is related to the predicted optimal penetration ratio, which will be below 1 and even lower with the increase in number of layers.

List of Figures

1.1. Operation principle of Power Electronic Transformers.	5
1.2. Possible Power Electronic Transformer structure.	5
1.3. 5L inverters.	6
1.4. Isolated dc-dc converter within a PET with indirect-conversion topology.	6
1.5. Two main topologies for the ac-link of isolated dc-dc converters. . .	7
1.6. Traction converter with MF transformers.	8
1.7. Offshore wind farm topology with MF transformers.	10
1.8. Combination of intermittent sources with storage facilities.	10
1.9. Flexible medium-voltage grid with medium-frequency transformers.	11
1.10. Transmission and distribution MF transformers for ac or dc grids.	12
1.11. Magnetic material comparison.	16
2.1. Equivalent circuit of a transformer with corresponding loss and energy storing elements.	21
2.2. Current density in an isolated 4 mm round copper conductor with total net current of 10 A for various frequencies.	22
2.3. Current density in an open circuited 4 mm copper conductor placed within a external field $H_{y_{ext}}$, external magnetic field with only y-component.	24
2.4. Cut view of an EE core transformer with foil windings, infinite permeability magnetic material and one dimensional magnetic field in the core window.	25

2.5. Foil conductor carrying a peak current I within a transformer core window, with general boundary conditions. 26

2.6. Magnetic field and current density in a two layer winding for various frequencies, with $d_w = 2$ mm and 1 mm of inter-layer space. Boundary conditions (H_{int} , H_{ext}): (0, 1) and (1, 2) for the first and second layer, respectively. 27

2.7. Transformer winding with several primary and secondary layers and equivalent dc magnetic field distribution within foil conductors according to Ampere’s circuital law. 29

2.8. Dowell resistance factor expression F_r versus penetration ratio. . . 30

2.9. Representation of the equivalent foil conductor, from round conductors to equivalent square conductors to equivalent foil conductors and finally to whole window foil conductors. 31

2.10. Representation of the position variation of a strand in a Litz bundle. 36

2.11. Type of eddy currents in Litz conductors. Illustration introduced in [Sullivan, 1999]. 36

2.12. Total current density in a single round Litz wire $d_b = 4.5$ mm, with 37 strands of $d_s = 0.64$ mm and $f = 20$ kHz. 37

2.13. Comparison of different expressions for the determination of skin effect losses in an isolated round conductor with $d_s = 0.2$ mm. . . . 39

2.14. Litz bundle, the radial position of each strand is considered to apply the radial dependent internal magnetic field. 40

2.15. Comparison of different expressions for the determination of internal proximity losses in a single isolated Litz bundle with $d_b = 4.5$ mm and 37 strands of $d_s = 0.64$ mm. 41

2.16. Total current density and magnetic field lines in a single isolated Litz bundle $d_b = 4.5$ mm, with 37 strands of $d_s = 0.64$ mm for different penetration ratios. 42

2.17. Comparison of different expressions for the determination of external proximity losses in an open circuited Litz bundle $d_b = 4.5$ mm, with 37 strands of $d_s = 0.64$ mm, within an external magnetic field $H_e = 1$ A/mm for different penetration ratios. 43

2.18. Total current density and magnetic field lines in an open circuited Litz bundle $d_b = 4.5$ mm, with 37 strands of $d_s = 0.64$ mm, within an external magnetic field $H_e = 1$ A/mm for different penetration ratios.	43
2.19. Comparison of different expressions for the determination of total Litz wire winding losses for different number of layers. Five Litz bundles per layer $d_b = 0.54$ mm, with 37 strands of $d_s = 0.2$ mm. .	45
2.20. Four layer winding, two primary and two secondary. First column, layers are interleaved, $m=1$. Second column, consecutive layers, $m=2$.	47
2.21. Isolated rectangular Litz bundle (half) for various penetration ratios.	48
2.22. Transformer winding with several primary and secondary layers and equivalent dc magnetic field distribution within foil conductors according to Ampere's circuital law.	49
2.23. Magnetic field distribution in a transformer composed of three layers per winding, dc field (-) and ac field (--)representation.	53
2.24. Leakage inductance ($\mu\text{H/m}$) in a transformer with 3 primary and secondary copper layers, with $d_{w_1} = d_{w_2} = 2$ mm, $d_g = d_{i_1} = d_{i_2} = 1$ mm and $h_w = 20$ mm.	54
2.25. Types of hysteresis loops and magnetization curves.	57
2.26. Anhysteretic curve and mayor loop.	58
2.27. Preisach bistable unit and Preisach plane, or triangle.	60
2.28. Chan-Vladirimescu model with initial magnetization curve, mayor loop and minor symmetrical loops.	62
2.29. Magnetic characteristic and equivalent elliptical loop.	66
2.30. Measurements carried out in a FeSi transformer in order to verify the magnetic induction slope dependency.	71
2.31. Basic configuration of an equivalent nodal network.	76
2.32. Grasshof number for various characteristic lengths D , with $T_f = 30^\circ\text{C}$. Fluid air.	81
2.33. Radiation approximation for various temperature differences with $T_f = 30^\circ\text{C}$ and $\varepsilon = 0.9$	83
2.34. Analyzed transformer geometry and basic equivalent nodal network.	83
2.35. Temperature distribution for different winding geometries.	86

3.1. Proposed medium-frequency transformer design methodology flow chart.	92
3.2. C-core dimensions.	95
3.3. Core-type or shell-type transformer structures for the same fictive volume.	99
3.4. Maximum power, supposing an efficiency of $\eta = \%99$. Possible transformer configurations with $D = 146$ mm and $A=[25$ mm (red), 50 mm (green), 75 mm (blue)]. Natural convection with $T_{amb} = 40^\circ\text{C}$, $T_{surface} = 100^\circ\text{C}$ and $\varepsilon = 0.8$	101
3.5. Current density vs area product. Possible transformer configurations with $D = 146$ mm and $A=[25$ mm (red), 50 mm (green), 75 mm (blue)]. Natural convection with $T_{amb} = 40^\circ\text{C}$, $T_{surface} = 100^\circ\text{C}$ and $\varepsilon = 0.8$. Filling factor 0.2.	103
3.6. Operating frequency range for a shell-type transformer. Possible transformer configurations with $D = 146$ mm and $A=[25$ mm (red), 50 mm (green), 75 mm (blue)]. Natural convection with $T_{amb} = 40^\circ\text{C}$, $T_{surface} = 100^\circ\text{C}$ and $\varepsilon = 0.8$	104
3.7. Operating frequency range for a core-type transformer. Possible transformer configurations with $D = 146$ mm and $A=[25$ mm (red), 50 mm (green), 75 mm (blue)]. Natural convection with $T_{amb} = 40^\circ\text{C}$, $T_{surface} = 100^\circ\text{C}$ and $\varepsilon = 0.8$	105
3.8. Resistance factor expression for various penetration ratios and number of layers.	106
3.9. Optimal penetration ratio and optimal conductor diameter for sinusoidal waveforms.	108
3.10. Resistance factor expression for various penetration ratios and number of strands, and for two number of layers.	109
3.11. Resistance factor expression for various penetration ratios and number of layers, and for two number of strands.	110
3.12. Optimal penetration ratio for sinusoidal waveforms, for various number of layers and strands.	111
3.13. Rectangular voltage waveform and trapezoidal magnetic induction.	112
3.14. Winding configurations.	114

3.15. Winding total height, considering the ending loop of the last turn.	114
3.16. Winding length depending on transformer composition.	116
3.17. Core and winding arrangement, considering the clearance and creepage distances.	117
3.18. Loss method comparison for various rectangular voltage waveforms, with $f = 2$ kHz, $B_{sq} = 500$ mT, $K = 6.5$, $a = 1.51$ and $b = 1.74$. Theoretical results.	119
3.19. Transformer from the UNIFLEX-PM project, composed of two Power System cores.	120
3.20. Measurements carried out in the UNIFLEX-PM project. Transformer built with two Power System cores.	120
3.21. Measurement results for various rectangular voltage waveforms, with $f = 2$ kHz, $B_{sq} = 500$ mT, $K = 6.5$, $a = 1.51$ and $b = 1.74$. . .	121
3.22. Primary and secondary winding length, considering the intra-layer and inter-winding isolation distances.	123
3.23. Magnetic field distribution within the considered winding structures.	124
4.1. Three-port structure proposal on the UNIFLEX-PM European Project.	133
4.2. Medium-frequency individual conversion cell structures compared within the UNIFLEX-PM project.	134
4.3. Two-port reduced-scale conversion system.	135
4.4. Bidirectional isolated dc-dc converter, the Dual Active Bridge (DAB).	136
4.5. Equivalent operation principle schema of the DAB and phasor representation for the first harmonic.	137
4.6. Voltage and current waveforms in the converter and transformer when both dc voltages are equal.	137
4.7. Active and reactive power for various phase-shifts with $L_\sigma = 480$ μ H, $f = 2$ kHz, $U_{dc1} = 1100$ and (a) $U_{dc2} = 1100$ or (b) $U_{dc2} = 1200$. . .	139
4.8. Current through the transformer and its derivative	142
4.9. Optimal conductor diameter for various layers and frequencies, with $\gamma = 0.1309$ and $U_{dc1} = 1200$, $U_{dc2} = 1100$. Worst case scenario. . .	143

4.10. Amplitude of the current harmonics, for $f = 2 \text{ kHz}$, $L_\sigma = 480 \mu \text{ H}$,
 $U_{dc1} = 1100$, $U_{dc2} = 1200$ and $\gamma = 0.1309 \text{ rad}$ 146

4.11. Image of the prototype transformer. 148

4.12. Expected winding resistance. 150

4.13. Picture of the experimental set-up. 152

4.14. Transformer low-frequency model. 153

4.15. Short circuit primary and secondary side measurements. 154

4.16. Open circuit measurement set-up schematic. 155

4.17. PC post-processing schematic. 156

4.18. Measured voltage and current waveforms. 156

4.19. BH loop of the prototype. Rectangular voltage excitation at 2 kHz.
 Two periods are drawn to illustrate the periodicity and to verify the
 measurement quality. 157

4.20. Magnetic loss density at 2 kHz and rectangular voltage waveforms. 158

4.21. Prototype transformer BH loops for various frequencies and excita-
 tion voltages. 159

4.22. Curve fitting (-) of measured data (--), $k_i = 2.0316$, $a = 1.1126$ and
 $b = 1.5864$ 160

4.23. Metgals 2605SA1 iron-based amorphous alloy dc BH Loop provided
 by the manufacturer for the AMDT Cores (Power System Series)
 and for the Powerlite C-Cores (High-Frequency Series). 161

4.24. Thermal measurement converter schematic. 162

4.25. Thermal measurement set-up. 163

4.26. Thermocouple in the core of the transformer. 164

4.27. Transformer thermal image with the four reference points. 165

4.28. Thermal response of the four points within the frontal plane of the
 varnished transformer. 166

4.29. Thermal response of the four points within the frontal plane of the
 unvarnished transformer. 167

4.30. Thermal response of the varnished transformer, measurement card.
 Left-hand side of the transformer gray and right-hand side of the
 transformer black. 168

4.31. Thermal response of the varnished transformer in the frontal 4 measurement points, transformer top side and bottom side. Left-hand side of the transformer gray and right-hand side of the transformer black.	169
4.32. Equivalent thermal circuit of the transformer.	170
5.1. Acoustic measurements at 2 kHz.	177
A.1. Bessel functions and approximations for various arguments.	185
B.1. Maximum power, supposing an efficiency of $\eta = \%99$. Possible transformer configurations with $D = 146$ mm and $A=[25$ mm (red), 50 mm (green), 75 mm (blue)]. Natural convection with $T_{amb} = 40^\circ\text{C}$, $T_{surface} = 100^\circ\text{C}$ and $\varepsilon = 0.8$	189
B.2. Current density vs area product. Possible transformer configurations with $D = 146$ mm and $A=[25$ mm (red), 50 mm (green), 75 mm (blue)]. Natural convection with $T_{amb} = 40^\circ\text{C}$, $T_{surface} = 100^\circ\text{C}$ and $\varepsilon = 0.8$. Filling factor 0.2.	189
B.3. Operating frequency range for a shell-type transformer. Possible transformer configurations with $D = 146$ mm and $A=[25$ mm (red), 50 mm (green), 75 mm (blue)]. Natural convection with $T_{amb} = 40^\circ\text{C}$, $T_{surface} = 100^\circ\text{C}$ and $\varepsilon = 0.8$	190
B.4. Operating frequency range for a core-type transformer. Possible transformer configurations with $D = 146$ mm and $A=[25$ mm (red), 50 mm (green), 75 mm (blue)]. Natural convection with $T_{amb} = 40^\circ\text{C}$, $T_{surface} = 100^\circ\text{C}$ and $\varepsilon = 0.8$	190
C.1. R_{ac}/R_δ vs. Δ and m . The minimum point for each number of layers is highlighted.	192
C.2. Dowell expression, power series approximation and incurred error for different values of the penetration ratio.	193
C.3. Estimation of conduction losses. The minimum from the iterative evaluation and from the optimal conductor thickness are highlighted.	194
C.4. Estimation error in the case of the Dual Active Bridge currents.	194

List of Tables

1.1. MF power transformer designs and physical prototypes found in the literature.	14
2.1. Skin depth in mm for common winding materials.	23
2.2. Comparison of the relative percentage error of two closed form expressions and for different porosity factors.	34
2.3. Magnetic energies in different winding spaces referred to the primary current.	52
3.1. Dimensional limits for iron-based amorphous alloys in Power System cores [METGLAS].	96
3.2. Dimensional characteristics for the core-type and shell-type transformers.	100
3.3. Core-loss expressions for rectangular voltage profiles.	118
4.1. Main parameters of the reduced-scale prototype and the indirect-conversion structure.	135
4.2. Powerlite form dimensions, made of iron-based amorphous alloy 2605SA1 ribbons or laminations.	141
4.3. Selected rectangular Litz bundles.	144
4.4. AMCC-367S core characteristics.	149
4.5. Transformer current harmonic content.	151
B.1. Thermal properties of various fluids, $T =$ temperature [$^{\circ}\text{C}$].	188

Bibliography

- Aggeler, D., Biela, J. and Kolar, J. [2008]. A compact, high voltage 25 kW, 50 kHz dc-dc converter based on SiC JFETs, *23rd Annual IEEE Applied Power Electronics Conference and Exposition, APEC*, pp. 801–807.
- Akagi, H. and Inoue, S. [2006]. Medium-voltage power conversion systems in the next generation, *5th International Power Electronics and Motion Control Conference, IPEMC*, Vol. 1, pp. 1–8.
- Bartoli, M., Noferi, N., Reatti, A. and Kazimierczuk, M. [1996]. Modeling litz-wire winding losses in high-frequency power inductors, *IEEE 27th Annual Power Electronics Specialists Conference, PESC*, Vol. 2, pp. 1690–1696.
- Bennet, E. and Larson, S. [1940]. Effective resistance to alternating currents of multilayer windings, *AIEE Transactions* **59**: 1010–1017.
- Bertotti, G. [1986]. Some considerations on the physical interpretation of eddy current losses in ferromagnetic materials, *Journal of magnetism and magnetic materials* **54-57**(1-3): 1556–1560.
- Bertotti, G. [1992]. Dynamic generalization of the scalar preisach model of hysteresis, *IEEE Transactions on Magnetics* **28**(5 Part 2): 2599–2601.
- Biczel, P. [2007]. Power electronic converters in dc microgrid, *Compatibility in Power Electronics, CPE*, pp. 1–6.
- Bifaretti, S., Zanchetta, P., Yue, F., Iov, F. and Clare, J. [2008]. Power flow control through a multi-level H-bridge based power converter for universal and flexible

- power management in future electrical grids, *13th International Conference on Power Electronics and Motion Control, EPE-PEMC*, pp. 1771–1778.
- Blaabjerg, F., Iov, F., Teodorescu, R. and Chen, Z. [2006]. Power electronics in renewable energy systems, *12th International Conference on Power Electronics and Motion Control, EPE-PEMC*, pp. 1–17.
- Bonnans, J. F., Gilbert, J. C., Lemaréchal, C. and Sagastizábal, C. A. [2006]. *Numerical Optimization*, Springer.
- Bose, B. K. [2009]. Power electronics and motor drives recent progress and perspective, *IEEE Transactions on Industrial Electronics* **56**(2): 581–588.
- Chabert, C. and Rufer, A. [2001]. Multilevel converter with 2 stage-conversion, *9th European Conference on Power Electronics and Applications, EPE*.
- Chan, J., Vladimirescu, A., Gao, X.-C., Liebmann, P. and Valainis, J. [1991]. Nonlinear transformer model for circuit simulation, *IEEE Transactions on Computer-Aided Design of Integrated Circuits and Systems* **10**(4): 476–482.
- de Doncker, R., Divan, D. and Kheraluwala, M. [1988]. A three-phase soft-switched high power density dc-dc converter for high power applications, *23rd Annual Meeting of the IEEE Industry Applications Society, IAS*, Vol. 1, pp. 796–805.
- della Torre, E. and Vajda, F. [1994]. Parameter identification of the complete-moving-hysteresis model using major loop data, *IEEE Transactions on Magnetics* **30**(6): 4987–5000.
- Dimitrakakis, G. and Tatakis, E. [2008]. Investigation of high frequency effects on layered coils, *13th International Conference on Power Electronics and Motion Control, EPE-PEMC*, pp. 1301–1308.
- Dimitrakakis, G., Tatakis, E. and Rikos, E. [2007]. A new model for the determination of copper losses in transformer windings with arbitrary conductor distribution under high frequency sinusoidal excitation, *12th European Conference on Power Electronics and Applications, EPE*, pp. 1–10.

- Doebbelin, R., Benecke, M. and Lindemann, A. [2008]. Calculation of leakage inductance of core-type transformers for power electronic circuits, *13th International Conference on Power Electronics and Motion Control, EPE-PEMC*, pp. 1280–1286.
- Dowell, P. [1966]. Effects of eddy currents in transformer windings, *Proceedings of the IEE* **113**(8): 1387–1394.
- Engel, B., Victor, M., G., B. and Falk, A. [2003]. 15 kV-16.7 Hz energy supply system with medium frequency transformer and 6.5 kV IGBTs in resonant operation, *10th European Conference on Power Electronics and Applications, EPE*.
- Ferreira, J. [1990]. Appropriate modelling of conductive losses in the design of magnetic components, *IEEE 21st Annual Power Electronics Specialists Conference, PESC*, pp. 780–785.
- Ferreira, J. [1992]. Analytical computation of ac resistance of round and rectangular litz wire windings, *Electric Power Applications, IEE Proceedings B* **139**(1): 21–25.
- Ferreira, J. [1994]. Improved analytical modeling of conductive losses in magnetic components, *IEEE Transactions on Power Electronics* **9**(1): 127–131.
- Filchev, T., Wheeler, P., Clare, J., Yudov, D., Valchev, V. and Van den Bossche, A. [2004]. A LCL resonant dc-dc converter for electrical power distribution systems, *11th International Conference on Power Electronics and Motion Control, EPE-PEMC*.
- Fischer, D., Mecke, R. and Rathge, C. [2002]. Bidirectional isolated dc-dc converter for energy storage integration in modular photovoltaic systems, *10th International Conference on Power Electronics and Motion Control, EPE-PEMC*.
- Heinemann, L. [2002]. An actively cooled high power, high frequency transformer with high insulation capability, *17th Annual IEEE Applied Power Electronics Conference and Exposition, APEC*, Vol. 1.

- Heinemann, L. and Mauthe, G. [2001]. The universal power electronics based distribution transformer, an unified approach, *IEEE 32nd Annual Power Electronics Specialists Conference, PESC*, Vol. 2, pp. 504–509.
- Hiller, M., Sommer, R. and Beuermann, M. [2008]. Converter topologies and power semiconductors for industrial medium voltage converters, *43rd Annual Meeting of the IEEE Industry Applications Society, IAS*, pp. 1–8.
- Hugo, N., Stefanutti, P. and Pellerin, M. [2007]. Power electronics traction transformer, *12th European Conference on Power Electronics and Applications, EPE*.
- Hui, S. and Zhu, J. [1995]. Numerical modelling and simulation of hysteresis effects in magnetic cores using transmission-line modelling and the preisach theory, *Electric Power Applications, IEE Proceedings - 142*(1): 57–62.
- Hurley, W., Gath, E. and Breslin, J. [2000]. Optimizing the ac resistance of multilayer transformer windings with arbitrary current waveforms, *IEEE Transactions on Power Electronics 15*(2): 369–376.
- Hurley, W., Wolffe, W. and Breslin, J. [1998]. Optimized transformer design: inclusive of high-frequency effects, *IEEE Transactions on Power Electronics 13*(4): 651–659.
- Iman-Eini, H., Farhangi, S. and Schanen, J. [2008]. A modular ac-dc rectifier based on cascaded H-bridge rectifier, *13th International Conference on Power Electronics and Motion Control, EPE-PEMC*, pp. 173–180.
- Inoue, S. and Akagi, H. [2007]. A bi-directional dc-dc converter for an energy storage system, *22nd Annual IEEE Applied Power Electronics Conference and Exposition, APEC*, pp. 761–767.
- Jiles, D. C. and Atherton, D. L. [1984]. Theory of ferromagnetic hysteresis (invited), *Journal of Applied Physics 55*(6): 2115–2120.
- Jiles, D., Thoelke, J. B. and Devine, M. K. [1992]. Numerical determination of hysteresis parameters for the modeling of magnetic properties, *IEEE Transactions on Magnetics 28*(1): 27–35.

- John H. Lienhard IV and John H. Lienhard V [2004]. *A Heat Transfer Textbook*, Phlogiston Press.
- Kheraluwala, M., Gascoigne, R., Divan, D. and Baumann, E. [1992]. Performance characterization of a high-power dual active bridge dc-to-dc converter, *IEEE Transactions on Industry Applications* **28**(6): 1294–1301.
- Kjellqvist, T., Norrga, S. and Ostlund, S. [2004]. Design considerations for a medium frequency transformer in a line side power conversion system, *IEEE 35th Annual Power Electronics Specialists Conference, PESC*, Vol. 1, pp. 704–710.
- Konishi, H., Kawazoe, H., Makino, Y. and Imaizumi, T. [2005]. Study on multi-terminal dc transmission system applicable to distribution systems for specific area, *International Power Electronics Conference, IPEC*.
- Lai, J., Maitra, A., Mansoor, A. and Goodman, F. [2005]. Multilevel intelligent universal transformer for medium voltage applications, *40th Annual Meeting of the IEEE Industry Applications Society, IAS*, Vol. 3, pp. 1893–1899.
- Lammeraner, J. and Štafl, M. [1966]. *Eddy Currents*, Iliffe Books LTD, London.
- Lancarotte, M.S. and de A. Penteado, A. J. [2001]. Estimation of core losses under sinusoidal or nonsinusoidal induction by analysis of magnetization rate, *IEEE Transaction on Energy Conversion* **16**(2): 174–179.
- Li, J., Abdallah, T. and Sullivan, C. [2001]. Improved calculation of core loss with nonsinusoidal waveforms, *36th Annual Meeting of the IEEE Industry Applications Society, IAS*, Vol. 4, pp. 2203–2210.
- Lin, D., Zhou, P., Fu, W. N., Badics, Z. and Cendes, Z. J. [2004]. A dynamic core loss model for soft ferromagnetic material and power ferrite materials in transient finite element analysis, *IEEE Transactions on Magnetics* **40**(2): 1318–1321.
- Lotfi, A. and Lee, F. [1993]. A high frequency model for litz wire for switch-mode magnetics, *28th Annual Meeting of the IEEE Industry Applications Society, IAS*, Vol. 2, pp. 1169–1175.

- Marchesoni, M., Novaro, R. and Savio, S. [2002]. Ac locomotive conversion systems without heavy transformers - Is it a practicable solution?, *IEEE International Symposium on Industrial Electronics, ISIE*, Vol. 4, pp. 1172–1177.
- Mariethoz, S. and Rufer, A. [2006]. Multisource dc-dc converter for the supply of hybrid multilevel converter, *41st Annual Meeting of the IEEE Industry Applications Society, IAS*, Vol. 2, pp. 982–987.
- Mayergoyz [1986]. Mathematical models of hysteresis, *The American Physical Society* **56**(15): 1518–1521.
- McLyman, C. W. T. [2004]. *Transformer and Inductor Design Handbook*, Marcel Dekker, Inc.
- Meier, S., Norrga, S. and Nee, H.-P. [2004]. New topology for more efficient ac-dc converters for future offshore wind farms, *IEEE Nordic Workshop on Power and Industrial Electronics, NORPIE*.
- METGLAS 2605SA1 [2009]. <http://www.metglas.com/>, *Technical report*, Hitachi Metals.
- Meyer, C., Hoing, M., Peterson, A. and de Doncker, R. [2007]. Control and design of dc grids for offshore wind farms, *IEEE Transactions on Industry Applications* **43**(6): 1475–1482.
- Mohan, N., Undeland, T. and Robbins, W. [2002]. *Power Electronics: Converters, Applications, and Design*, Wiley.
- Morren, J., Pavlovsky, M., de Haan, S. and Ferreira, J. [2001]. Dc-dc conversion for offshore windfarms, *9th European Conference on Power Electronics and Applications, EPE*.
- Nan, X. and Sullivan, C. [2003]. An improved calculation of proximity-effect loss in high-frequency windings of round conductors, *IEEE 34th Annual Power Electronics Specialist Conference, PESC*, Vol. 2, pp. 853–860.
- Nilsson, D. and Sannino, A. [2004]. Efficiency analysis of low- and medium-voltage dc distribution systems, *IEEE Power Engineering Society General Meeting*, Vol. 2, pp. 2315–2321.

- NOMEX [2009]. <http://www2.dupont.com>, *Technical report*, DuPont.
- Norrgra, S. [2006]. Experimental study of a soft-switched isolated bidirectional ac-dc converter without auxiliary circuit, *IEEE Transactions on Power Electronics* **21**(6): 1580–1587.
- Oates, C. and Bassett, R. [2006]. Future T&D technology, *12th International Conference on Power Electronics and Motion Control, EPE-PEMC*, pp. 2144–2148.
- Pavlovsky, M., de Haan, S. and Ferreira, J. [2005]. Concept of 50kW dc/dc converter based on ZVS, quasi-ZCS topology and integrated thermal and electromagnetic design, *11th European Conference on Power Electronics and Applications, EPE*.
- Prasai, A., Jung-Sik, Y., Divan, D., Bendre, A. and Seung-Ki, S. [2008]. A new architecture for offshore wind farms, *IEEE Transactions on Power Electronics* **23**(3): 1198–1204.
- Preisach, F. [1935]. Über die magnetische nachwirkung, *Zeitschrift für Physik* **94**: 277–302.
- Prieto, R., Cobos, J., Garcia, O., Alou, P. and Uceda, J. [1998]. Taking into account all the parasitic effects in the design of magnetic components, *13th Annual IEEE Applied Power Electronics Conference and Exposition, APEC*, Vol. 1.
- Reatti, A. and Kazimierczuk, M. [2002]. Comparison of various methods for calculating the ac resistance of inductors, *IEEE Transactions on Magnetics* **38**(3): 1512–1518.
- Reinert, J., Brockmeyer, A. and de Doncker, R. [2001]. Calculation of losses in ferro- and ferrimagnetic materials based on the modified steinmetz equation, *IEEE Transactions on Industry Applications* **37**(4): 1055–1061.
- Reinold, H. and Steiner, M. [1999]. Characterization of semiconductor losses in series resonant dc-dc converters for high power applications using transformers with low leakage inductance, *8th European Conference on Power Electronics and Applications, EPE*.

- Robert, F., Mathys, P. and Schauwers, J.-P. [2000]. The layer copper factor, although widely used and useful, has no theoretical base [smcs transformers], *IEEE 31st Annual Power Electronics Specialists Conference, PESC*, Vol. 3, pp. 1633–1638.
- Robert, F., Mathys, P. and Schauwers, J.-P. [2001]. A closed-form formula for 2-d ohmic losses calculation in smcs transformer foils, *IEEE Transactions on Power Electronics* **16**(3): 437–444.
- Roshen, W. [2007]. A practical, accurate and very general core loss model for nonsinusoidal waveforms, *IEEE Transactions on Power Electronics* **22**(1): 30–40.
- Rufer, A. [2007a]. Benefits of short- and long-term energy storage in the context of renewable energies and sustainable management of energy resources, *International Exhibition and Conference Ecological Vehicles & Renewable Energies, EVER*.
- Rufer, A. [2007b]. Today's and tomorrow's meaning of power electronics within the grid interconnection, *12th European Conference on Power Electronics and Applications, EPE*, pp. 1–11.
- Schibli, N. [2000]. *Symmetrical multilevel converters with two quadrant dc-dc feeding*, PhD thesis, École Polytechnique Fédérale de Lausanne.
- Shen, W. [2006]. *Design of High-Density Transformers for High-Frequency High-Power Converters*, PhD thesis, Virginia Polytechnic Institute and State University.
- Siemaszko, D., Zurkinden, F., Fleischli, L., Villar, I., De Novaes, Y. R. and Rufer, A. [2009]. Description and efficiency comparison of two 25kva dc/ac isolation modules, *EPE Journal* **19**(4).
- Steiner, M. and Reinold, H. [2007]. Medium frequency topology in railway applications, *12th European Conference on Power Electronics and Applications, EPE*.

- Steinmetz, C. [1892]. On the law of hysteresis, *American Institute of Electrical Engineers Transactions* **9**: 3–64.
- Strbac, G., Jenkins, N. and Green, T. [2006]. Future network technologies, *Technical report*, UK Department for Business, Enterprise & Regulatory Reform.
- Sullivan, C. [1999]. Optimal choice for number of strands in a litz-wire transformer winding, *IEEE Transactions on Power Electronics* **14**(2): 283–291.
- Taufiq, J. [2007]. Power electronics technologies for railway vehicles, *International Power Conversion Conference, PCC*, pp. 1388–1393.
- Tourkhani, F. and Viarouge, P. [2001]. Accurate analytical model of winding losses in round litz wire windings, *Magnetics, IEEE Transactions on* **37**(1 Part 2): 538–543.
- UNIFLEX [2006]. <http://www.eee.nott.ac.uk/uniflex/>, *Technical report*.
- van den Bossche, A., Valchev, V. and Georgiev, G. [2004]. Measurement and loss model of ferrites with non-sinusoidal waveforms, *IEEE 35th Annual Power Electronics Specialists Conference, PESC*, Vol. 6, pp. 4814–4818.
- Venkatachalam, K., Sullivan, C., Abdallah, T. and Tacca, H. [2002]. Accurate prediction of ferrite core loss with nonsinusoidal waveforms using only steinmetz parameters, *IEEE Workshop on Computers in Power Electronics*, pp. 36–41.
- Villar, I., Viscarret, U., Etxeberria-Otadui, I. and Rufer, A. [2008]. Transient thermal model of a medium frequency power transformer, *Proc. 34th Annual Conference of IEEE Industrial Electronics IECON 2008*, pp. 1033–1038.
- VITROPERM 500F [2009]. <http://www.vacuumschmelze.de/>, *Technical report*, Vacuumschmelze.
- Wang, D., Mao, C. and Lu, J. [2007]. Modelling of electronic power transformer and its application to power system, *Generation, Transmission & Distribution, IET* **1**(6): 887–895.

Wu, B., Pontt, J., Rodríguez, J., Bernet, S. and Kouro, S. [2008]. Current-source converter and cycloconverter topologies for industrial medium-voltage drives, *IEEE Transactions on Industrial Electronics* **55**(7): 2786–2797.

Curriculum Vitae

Irma Villar Iturbe

Born 17th March 1980

✉ ivillar@ikerlan.es

EDUCATION

- 2009 to date **Researcher** at the Control Engineering and Power Electronics Area, Ikerlan-IK4, Arrasate-Mondragón, Spain.
- 2005 - 2009 **PhD thesis** under the supervision of Professor Alfred Rufer at the Industrial Electronics Laboratory (LEI), at the EPFL, Lausanne, Switzerland in collaboration with the Control Engineering and Power Electronics Area at Ikerlan-IK4, Arrasate-Mondragón, Spain.
- 2004 - 2005 Master Thesis Project "Analysis, simulation and implementation of sensorless control strategies for brushless ac motors" in the Control Engineering and Power Electronics Area, in Ikerlan-IK4, Arrasate-Mondragón, Spain.
- 2002 - 2004 **Master** in Engineering in Automatics and Industrial Electronics, in the Faculty of Engineering, Mondragón Unibertsitatea, Arrasate-Mondragón, Spain.
- 2002 Bachelor Thesis Project "Implementation of a speed controller for a stepper motor based on a PIC microcontroller", in the Faculty of Engineering, Mondragón Unibertsitatea, Arrasate-Mondragón, Spain
- 1998 - 2002 **Bachelor** in Technical Engineering in Industrial Electronics, in the Faculty of Engineering, Mondragón Unibertsitatea, Arrasate-Mondragón, Spain.

LANGUAGES

- Basque Native language
- Spanish Native language
- English Fluent (spoken and written)
- French Fluent (spoken and written)
- German Basic understanding

PUBLICATIONS

D. Siemaszko, F. Zurkinden, L. Fleischli, I. Villar, Y. R. De Novaes and A. Rufer, "Description and efficiency comparison of two 25 kVA dc/ac isolation modules", in *EPE Journal*, Vol. 19, No. 4, December 2009.

I. Villar, U. Viscarret, I. Etxeberria-Otadui and A. Rufer, "Global loss evaluation methods for non-sinusoidally fed medium frequency power transformers", in *IEEE Transactions on Industrial Electronics*, Vol. 56, No. 10, October 2009.

I. Villar, U. Viscarret, I. Etxeberria-Otadui and A. Rufer, "Transient thermal model of a medium frequency power transformer" in *34th Annual Conference of the IEEE Industrial Electronics Society, IECON*, 2008.

I. Villar, A. Rufer, U. Viscarret, F. Zurkinden and I. Etxeberria-Otadui, "Analysis of empirical core loss evaluation methods for non-sinusoidally fed medium frequency power transformers", in *IEEE International Symposium on Industrial Electronics, ISIE*, 2008.

EPFL, Lausanne

22nd January 2010